Palaeogeography Palaeoclimatology Palaeoecology
July 2023, Volume 621 Pages 111562 (25p.)
https://doi.org/10.1016/j.palaeo.2023.111562
https://archimer.ifremer.fr/doc/00852/96387/

Archimer
https://archimer.ifremer.fr

Land-sea linkages on the Algerian Margin over the last 14 kyrs BP: Climate variability at orbital to centennial timescales

Coussin V [6, *], Penaud A. [6, *], Combourieu-Nebout N. [2], Peyron O. [3], Sicre M. A. [4], Tisnerat-Laborde N. [5], Cattaneo Antonio [1], Babonneau Nathalie [6]

[1] Univ. Brest, CNRS, Ifremer, Geo-Ocean, UMR 6538, F-29280 Plouzané, France
[2] HPNP, CNRS, UMR 7194, Département de Préhistoire du Muséum d'Histoire Naturelle, F-75013 Paris, France
[3] LOCEAN, CNRS, Sorbonne Université, Campus Pierre et Marie Curie, F75005 Paris, France
[4] Sorbonne Univ, LOCEAN, CNRS, Campus Pierre & Marie Curie, F-75005 Paris, France.
[5] Laboratoire des Sciences du Climat et de l'Environnement, LSCE/IPSL, UMR 8212 UVSQ-CNRS-CEA, Avenue de la Terrasse, 91198 Gif-sur-Yvette, France.
[6] Univ. Brest, CNRS, Ifremer, Geo-Ocean, UMR 6538, F-29280 Plouzané, France

* Corresponding authors : V. Coussin, email address : vincent.coussin@univ-brest.fr ; A. Penaud, email address : aurelie.penaud@univ-brest.fr

Abstract :

Past and present environmental conditions over the Holocene along the Algerian coast involve complex atmosphere-hydrosphere-biosphere interactions and anthropogenic activities on adjacent watersheds. Atlantic Ocean surface waters entering the western Mediterranean Sea at the Gibraltar Strait create the Algerian Current, which flows along the North African coast in a succession of strong and large-scale eddies. Deep-water upwelling plumes are other recurrent hydrological features of the Algerian margin affecting regional environmental features. However, vegetation and paleohydrological changes that have occurred over the Holocene have not yet been described. To bridge this gap, a suite of paleoclimate proxies was analysed in marine core MD04-2801 (2067 m water depth) at a secular-scale resolution over the last 14 kyrs BP. Terrestrial (pollen grains) and marine (dinoflagellate cysts or dinocysts) palynological assemblages, as well as sedimentological (grain-size analysis and XRD-based quantitative analysis of clay minerals) and biomarkers (alkenones and n-alkanes), were determined to explore the links between past sea surface hydrological conditions and regional environmental changes on nearby watersheds.

The over-representation of heterotrophic dinocyst taxa (Brigantedinium spp.) indicates strong planktonic productivity in the study area. Results shows that the links between dryness on land and surface hydrological conditions are expressed by: (i) recurrent upwelling cells during the relatively dry climate conditions of the Younger Dryas (12.7 to 11.7 ka BP), the Early Holocene (11.7 to 8.2 ka BP) and from 6 ka BP onwards, (ii) enhanced fluvial discharges between 8.2 and 6 ka BP during the African Humid Period concomitant with the colonization of coastal lands by Mediterranean forest. Middle to Late Holocene

Please note that this is an author-produced PDF of an article accepted for publication following peer review. The definitive publisher-authenticated version is available on the publisher Web site.

transition around 4.2 ka BP characterizes by the intense event reffered to here as the Algerian Mega Drought (4.3 to 3.9 ka BP).

Highlights

► Land-sea multiproxy approach on the Algerian Margin over the last 14 kyrs. ► Productivity regimes closely associated with the vigour of the Algerian Current. ► Settlement of modern production conditions since 3 ka BP. ► First record of the Algerian Mega Drought event between 4.3 and 3.9 ka BP. ► NPP fingerprint in marine sediments related to erosion and river runoff.

Keywords : Holocene, Dinocysts, Pollen, Biomarkers, oy analysis, Algerian Current

Please note that this is an author-produced PDF of an article accepted for publication following peer review. The definitive publisher-authenticated version is available on the publisher Web site.

Abbreviations: AM: Algerian Margin; AC: Algerian Current; WMB: Western Mediterranean Basin; WMDW: Western Mediterranean Deep Waters; LIW: Ligurian Intermediate Waters; MOW: Mediterranean Outflow Waters; YD: Younger Dryas; B/A: Bölling-Alleröd.

1. Introduction

Interactions between low- and mid-latitude atmospheric circulations and local-scale configurations such as orography and coastal geomorphology, have created the specificities of the Mediterranean climate (Brayshaw et al., 2011). Furthermore, the summer season length depending on the vigor of the Hadley cell directly impacts summer droughts in the Mediterranean Basin (Lionello et al., 2006). In contrast, Mediterranean storm activity driving the main seasonal precipitation is strongly associated with the position and strength of the North-Atlantic mid-latitude storm tracks (Brayshaw et al., 2010). Consequently, the interactions between tropical convection and North-Atlantic storm tracks constitute a complex but essential element in understanding the long-term, rapid climate change that took place in the WMB during the Holocene. Climate changes during the last climatic cycle (e.g. Combourieu-Nebout et al., 1999, 2002; Sánchez-Goñi et al., 2002; Beaudouin et al., 2007; Bout-Roumazeilles et al., 2007; Brauer et al., 2007; Fletcher and Sánchez-Goñi, 2008; Kotthoff et al., 2008) have driven rapid paleoenvironmental changes in the Mediterranean basin.

Global warming, together with the generally high climatic and environmental sensitivity of this region raises questions concerning future environmental and human trajectories in the Mediterranean Basin, in particular due to subtropical aridification (IPCC report, 2019).

In this context, the Algerian Margin (AM) appears ideal to investigate both terrestrial (i.e. landscape changes) and marine (i.e. hydrological changes) ecosystems inherited from climate change and land-use practices over the Holocene. The AM, and mostly its westernmost part, is a highly productive area contrasting with the predominantly oligotrophic waters of the Western Mediterranean Basin (Sournia, 1973; Lohrenz et al., 1988). Strong riverine inputs (i.e. flash-flood episodes) to coastal waters and upwelling cells result in nutrient-enriched surface waters (Raimbault et al., 1993). These hydrological patterns provide understanding of the distribution of planktonic organisms as recently discussed for fossilized dinocysts at the scale of the Western Mediterranean Basin (WMB) (Coussin *et al*., 2022).

Numerous studies have shown the rapid response of Mediterranean environments to Holocene climate variability (e.g. Rohling et al., 2002; Fletcher et al., 2013; Chabaud et al., 2014; Sicre et al., 2016; Jalali et al., 2016; 2017, 2018; Di Rita et al., 2018; Bini et al., 2021), including research on remote short-term events of the North Atlantic Basin (e.g. Bond et al., 1997, 2001; Mayewski et al., 2004; Sicre et al., 2021). However, Holocene paleoenvironmental changes along the northern African margin, between the Alboran Sea (e.g. Combourieu-Nebout et al.,

1999, 2009 ; Fletcher et al., 2013) and the Sicilian Strait (e.g. Rouis-Zargouni et al., 2010, 2012; Desprat et al., 2013 ; Di Rita et al., 2018), remain poorly documented.

Here, we present new results for the AM based on the multi-proxy analysis of the marine core MD04-2801 (36°30.99'N; 0°30.03'E) over the last 14 kyrs BP, with a focus on the Holocene interval. This study benefited from a detailed sedimentological description (including X-ray fluorescence-XRF and grain-size analyses, clay mineral identification and conventional stable isotopes of O and C), centennial-scale resolution reconstructions of palynological proxies (pollen grains, dinocysts and other non-pollen palynomorphs or NPP), and molecular biomarkers (alkenones and n-alkanes). Our main objectives are i) to characterize upwelling variations through dinocyst assemblages and North-Atlantic atmospheric and hydrological influences on ecosystem variability, ii) to explore dryness and moisture conditions on land in relation with river discharge, iii) to assess the non-pollen palynomorphs (NPP) fingerprint in marine sediments and their relationship with erosion and river runoff on adjacent watersheds, iv) to evaluate the first pollen- and dinocyst-based quantifications of climate and hydrological parameters, respectively, in the study area. This dataset finally contributes to improve knowledge on north to south and west to east climatic and environmental gradients across the WMB.

2. Environmental context

2.1. Geographical and geomorphological background

The marine sediment core MD04-2801 was retrieved on the AM, 24 km from the coast, on the eastern side of the Kramis deep-sea fan (Babonneau et al., 2012; Figure 1b). From a geomorphological point of view, the Algerian coast is limited to the south by the Dahra Mountains (Cretaceous schist clay substratum) that reach an altitude of 1550 m and is bordered by the Tellian Atlas chain. The study area is surrounded by Tortonian (blue marls and sandstones), Messinian (gypsum, gypsy marls, diatomites and diatomitic marls), Pliocene (marine blue marls, sandstones and limestones), and Quaternary (calcareous sandstones, sands and alluvial deposits) geological land formations (e.g. Perrodon, 1957; Meghraoui et al., 1996; Belkebir et al., 2008; Osman et al., 2021). The proximity of the AM to high relief means that its environment includes small coastal watersheds and small, fluctuating river flows (i.e. oueds). The oued Cheliff, whose mouth is located around 60 km to the west of the MD04-2801 core site (Figure 1b), is the largest oued of the region and is characterized by an average weak flow of 15 $m^3.s^{-1}$, varying from 1.5 $m^3.s^{-1}$ during the dryest episodes to 1,500 $m^3.s^{-1}$ during flash-flood events (Gautier et al., 1998). The source of the oued Kramis (Figure 1b) is located in the Saharian Atlas and flows to the sea through the Dahra Mountains, distally feeding the Kramis deep-sea fan (Babonneau et al., 2012).

Two major climate features characterize the study area: i) mild conditions under the strong influence of mid-latitude westerly atmospheric circulation over the North Atlantic (i.e. westerlies), especially during winter, and ii) dry conditions (about 3 to 5 months per year) due to the strengthened Azores High, especially during summer (Lionello et al., 2006). The meteorological station at Mostaganem (near the Cheliff mouth) reports an average annual temperature of 18.7°C (minimum of 5°C and maximum of 25°C) between 1981 and 2010. Over this period, seasonal flash floods of nearby oueds, mainly during the "humid" season (fall to spring), represent the largest part of annual precipitation (i.e. average amount of 383 mm/yr, minimum of 1 mm/month and maximum of 71 mm/month). Flash floods drive huge amounts of terrigenous sediments (i.e. organic and inorganic particles and nutrients) to coastal waters due to their high erosive capacity (e.g. Pouquet, 1967; Guizien et al., 2007; Tzoraki and Nikolaidis, 2007).

2.2. Landscape

The Mediterranean landscapes shaping the study area are characterized by an altitudinal belt type organization split into three major subdivisions (Barbero et al., 1981; Polunin and Walters, 1985; Quezel and Medail, 2003). The thermo-Mediterranean belt covers lowlands and areas up from the coast to a 1,000 m altitude and is composed of *Olea*, *Pistacia,* sclerophillous shrublands and xerophytous taxa, associated with steppe and semi-desert representative taxa (e.g. *Artemisia,* Amaranthaceae, *Ephedra*). From 1,000 to 1,500 m, the meso-Mediterranean belt is composed of the sclerophyllous oak forest (e.g. *Quercus ilex, Quercus suber, Buxus* and *Myrtus)* and the humid-temperate oak forest (dominated by deciduous *Quercus* and Ericaceae, in association with *Juniperus* and *Cupressus*). At higher altitudes, from 1500 to 2300 m, the supra-Mediterranean belt is characterized by a specific coniferous forest (i.e. North African species of *Pinus, Abies* and *Cedrus*). The oro-Mediterranean belt extends up to 2800 m in the high Atlas with a high rate of representation of *Juniperus* (open forest taxon or arborescent mattorals). Finally, the alti-Mediterranean belt (i.e. mountainous regions) is composed of scattered Chamaephytae taxa (e.g. *Erica, Romarinus* and other Lamiaceae, *Ilex* or *Artemisia*) and represents the highest vegetation belt in the area. It corresponds to the grassland belt of European mountains (Quezel and Medail, 2003).

2.3. Hydrological context

The semi-enclosed Mediterranean Sea undergoes excess evaporation over freshwater input, resulting in a deficient water balance (Béthoux, 1979, 1984). The western Mediterranean Sea is strongly influenced by the Modified Atlantic Waters (MAW) entering through the Gibraltar strait, flowing along the Spanish coast and forming two anticyclonic gyres (i.e. the Western Alboran Gyre-WAG and the Eastern Alboran Gyre-EAG; Figure 1a). The Almeria-Oran front (35 km wide; 200 m deep; Figure 1a) position and intensity depends on the degree of development of the EAG (Tintoré et al., 1988; Rohling et al, 1995; Viúdez and Tintoré, 1995; Rohling et al., 2009). The MAW follow the Almeria-Oran front, which marks a deflection along the AM, forming the Algerian Current (AC, Figure 1; Millot, 1987; Millot, 1999, Millot and Taupier-Letage, 2005). The AC undulates eastward up to 30–40 km from the coast to 3°E (Millot, 1985, 1987; Arnone and La Violette, 1986; Arnone et al., 1990; Perkins and Pistek, 1990) where North African coast irregularities generate wind-driven eddies (cf. dotted arrows in Figure 1a). These eddies are responsible for northward coastal current extensions as well as the associated offshore propagation of low-salinity surface waters (Millot, 1999; Millot and Taupier-Letage, 2005).

The AC shows a salinity gradient from the Alboran Sea (< 37 psu; Arnone and La Violette, 1986) to the east and the internal zones of the WMB (psu > 37.5). In its coherent form, the AC marks a haline density front (Arnone et al., 1990; Perkins and Pistek, 1990) responsible for vertical mixing (i.e. upwelling; Sournia, 1973; Lohrenz et al., 1988; Raimbault et al., 1993), while the Alboran Sea is characterized by a general oligotrophic regime. On the coastal side of the density front, isopycnal mixing brings nutrient-enriched waters from the nutricline to the photic zone while, on the offshore side, diapycnal mixing brings deeper nutrients to the surface (i.e. nutrient export crossing the haline front; Raimbault et al., 1993), promoting enhanced productivity (Raimbault et al., 1993; Coussin et al., 2022). Additionally, seasonal offshore winds induce coastal upwelling, probably supported by low barometric pressure cells due to solar heating (Bakun and Agostini, 2001).

Finally, the regional climate (cf. section 2.1) is responsible for weak and irregular fluvial discharge especially during the dryest season (i.e. April to September) while strong oued discharge (i.e. flash floods) occasionally occurs during autumn and winter, transporting terrigenous material and nutrients to the sea (Guizien et al., 2007; Tzoraki and Nikolaidis, 2007).

2.3. Sedimentological context

Core MD04-2801 (36°30.99'N; 00°30.03'E; 24.82 m long; 2,063 m water depth) is located about 6 km north of the Kramis Canyon, which has an east to west orientation in the lower slope (Figure 1b). The core is located at the base of the slope and is separated from the canyon by a canyon terrace. Turbidity current overflow from the canyon to the core site is currently assumed to be very low (Babonneau et al., 2012). However, a contribution of diluted mud plumes at the top of the turbidity currents could explain the high sedimentation rates in the area. Finally, a large sediment wave field develops downslope along the right side of the Kramis Canyon. These sedimentary features mark the overflow zone of turbidity currents of the Kramis and Khadra canyons on the Kramis sedimentary ridge. Core MD04-2801 is located at the top of this field and was affected by intense overflow currents in the early phase of the formation of the Kramis sedimentary ridge (Babonneau et al., 2012).

The uppermost 10 m of MD04-2801 are not affected by gravity-driven sediment instability processes (i.e. turbidity currents and resulting turbidites; Babonneau et al., 2012). From 1045 cm upward (From section VII to section I; Figure 2), sediment generally consists of hemipelagic clays. Below 1,045 cm, section VIII consists of fine-grained turbidite beds (of approximately 1 cm thick) within a silty-clay matrix representing repeated destabilization of the shelf sediments via turbiditic plumes. Silty to sandy deposits lie on the slopes of the fan with a wide dispersal of turbiditic overflows across the abyssal plain (Babonneau et al., 2012). Around the Kramis fan, a canyon levee crest, 200 m higher than the channel bottom, only releases overflow of the largest turbidity currents, resulting in interfingered turbiditic levee deposits of the Kramis system with hemipelagic sediment (Babonneau et al., 2012). The absence of turbidites in the upper sections of core MD04-2801 (above 1,045 cm, Sections I to VII; Figure 2) reflects the isolation of the core site from the turbiditic channel due to aggradation of the levees.

3. Methodology

3.1. Sediment cores and stable isotope analyses

The log of core MD04-2801 was established through visual description of the sedimentary facies (Figure 2). The physical properties of the core (i.e. P-wave velocity, magnetic susceptibility and gamma-ray attenuation density) were measured using a 'Geotek Multi Sensor Core Logger' (MSCL) with a 2-cm-step (average 30 yrs) resolution at the Ifremer Marine Geosciences laboratory (Plouzané, France). X-ray fluorescence (XRF) profiles, for the semi-quantitative chemical composition analysis of the study core, were acquired with an "Avaatech

core-scanning XRF" with a 1-cm-step (average 15 yrs) resolution (Ifremer Marine Geosciences laboratory, Plouzané, France). In sediments, the Ti element is commonly interpreted as a terrigenous-siliclastic signature while the Ca element is related to carbonate materials of detritic and/or biogenic sources (Richter et al., 2006). Based on this assumption, the XRF-Ti/Ca ratio has been commonly used on silico-clastic margins (where Ca mainly originates from biogenic carbonates) to estimate varying terrigenous inputs to the marine realm. In this study, even if geological formations on land are mainly composed of carbonates, we will use this ratio combined with other proxies to track fluvial input to the marine realm.

Grain-size analyses were first performed at high resolution on total sediments (Master thesis of Si Bachir Roza, IUEM) and, in a second step, at a lower resolution on both total and decarbonated sediments (after HCl 30% treatment) at the IUEM (*Institut Universitaire Européen de la Mer*, Plouzané, France) using a Malvern MASTERSIZER 2000. The software GRADISTAT was used to produce particle grain-size distribution and size statistics from the laser granulometer data, including median grain size (D50) as well as sediment volumetric phase percentages (i.e. clays: $0 < Ø < 10$ µm, silts: $10 < Ø < 63$ µm, and sands: $Ø > 63$ µm).

Semi-quantitative mineralogical composition of the clay fraction was measured by X-ray diffraction (XRD) at the Ifremer Marine Geosciences laboratory (Plouzané, France) with a Bruker D2 PHASER set (with a Lynxeye fast detector; Cu X-ray tube; 30 kV voltage; 10 mA intensity). After decarbonation and decantation to retain only the < 2µm fraction, the sample was deposited on oriented glass. Each sample was routinely analyzed from 2 to 30° with a resolution of 0.02° lasting 1 s, with three XRD runs: i) air-dried, ii) ethylene-glycol saturated and iii) after calcination at 490°C. The characterization of each clayey mineral followed the description of Bout-Roumazeilles et al. (1999). Semi-quantitative estimation of clay mineral abundances (%) was performed using the Macintoch MacDiff® 4.2.5 software (R. Petschick, http://www.geologie.uni-frankfurt.de/Staff/Homepages/Petschick/RainerE.html).

Finally, stable isotopes were performed on planktonic *Globigerinoides bulloides* as well as endobenthic *Globobulimina affinis* foraminifera, hand-picked in the >150 µm sediment fraction. Isotopic analyses were conducted at the "*Pôle Spectrométrie Océan*" (IUEM, University of Brest, France) on a Finnigan MAT253 equipped with a Kiel-device automated introduction line. Analytical precisions for this spectrometer are <0.05‰ for the $\delta^{18}O$ and <0.03‰ for the $\delta^{13}C$ using, respectively, the certified NBS-19 and NBS-18 standards.

Core KMDJ-23 (36°30.006'N; 0°15.422'E; 7.52 m long; 2542 m water depth) was collected close to core MD04-2801 (Figure 1b). In this study, modern palynological assemblages related to current hydrological conditions are considered thanks to the top sediments of core KMDJ-

23 with radionucleide dating that confirmed the contemporaneous deposits at the study site (Coussin et al., 2022). We compare dinocyst data (i.e. *O. centrocarpum* for the North Atlantic influence (i.e. AC strengthening) *versus L. machaerophorum* for the estuarine influence (i.e. surface stratification) or Ocen/Lmac ratio), pollen data (sum of Mediterranean and Eurosiberian forest taxa), and alkenone SST, with coeval records of the Gulf of Cadiz (core MD99-2339), the Alboran Sea (ODP site 976 and core MD95-2043), the Algerian Margin-AM (MD04-2801, this study) and the Siculo-Tunisian strait (core MD04-2797).

3.2. Palynological analyses

3.3.1. Palynological treatments and palynomorph identifications

About 1 to 2 cm^3 of sediments were sampled every 20 cm in the upper MD04-2801 core (0 to 500 cm) at about 100 yrs resolution and every 10 cm in the lower part (500 to 1042 cm) at about 150 yrs resolution. Eighty-six samples were processed using the same palynological protocol as for palynomorph extraction, allowing direct comparison between terrestrial (pollen, spores, freshwater microalgae, and other continental non-pollen palynomorphs-NPPs) and marine (dinocysts and other marine NPPs such as marine microalgae or foraminiferal linings) microfossils on the same palynological slides. The preparation technique (Geo-Ocean laboratory, IUEM, France) was performed on the <150 µm fraction following the standardized palynological protocol of de Vernal et al. (1999), slightly adapted at the EPOC laboratory (University of Bordeaux, http://www.epoc.u-bordeaux.fr/index.php?lang=fr&page=eq_paleo_pollens). It includes chemical treatments (cold HCl: 10, 25 and 50%; cold HF: 45 and 70%, to remove carbonates and silicates, respectively) and sieving through single-use 10 µm nylon mesh screens. To avoid selective dinocyst degradation during sample treatment, no oxidative agent or heavy liquid technique was applied. Microscopic identification was performed with a Zeiss (Axio Scope.A1) microscope at x630 magnification. Absolute concentrations of palynomorphs were calculated using the marker grain method (Stockmarr, 1971; de Vernal et al., 1999; Mertens et al., 2009). Accordingly, aliquot volumes of *Lycopodium* spores were added to each sample before chemical treatment to allow the calculation of palynomorph concentrations as a number of palynomorphs/cm^3 of dry sediments (i.e. these exotic spores are counted simultaneously with studied palynomorphs for each sample).

A threshold of 100 individuals (> 5% in the total assemblage) is required to identify major species (Fatela and Taborda, 2002). In this study, 88 samples were analysed, with a minimum

count of 100 dinocysts (taxonomy following Fensome et al., 1993) and 150 pollen grains except for the over-represented taxon *Pinus* (Turon, 1984; Heusser and Balsam, 1985; taxonomy following Reille, 1992). Minimal counts were not reached for two dinocyst (40-41 and 541-542 cm) and three pollen (20-21, 440-441, 441-442 cm) assemblages. Their corresponding levels were therefore excluded from the discussion. Among dinocysts, *Brigantedinium* spp. includes all round-brown cysts, *Echinidinium* spp. includes all brown cysts with typical *Echinidinium* spine-like processes not determined on a species level, and *Spiniferites* spp. includes all *Spiniferites* taxa not determined on a species level. In addition, heterotrophic dinocysts (i.e. derived from dinoflagellates with a strict heterotrophic nutrional strategy) are indirectly related to food resources, especially diatoms, as commonly shown in upwelling areas (Wall et al., 1977; Lewis et al., 1990; Marret, 1994; Biebow, 1996; Zonneveld et al., 1997, 2001; Targarona et al., 1999; Bouimetarhan et al., 2009; Penaud et al., 2016). Therefore, the sum of heterotrophic taxa was made to account for "strict" heterotrophic dinocysts. Among continental palynomorphs, "undetermined fungal spores" include all fungal spores that cannot be determined on type-code, genus or species levels. Regarding relative abundance of pollen assemblages, percentages of *Pinus* were based on the total pollen sum, while continental NPP relative abundances were calculated on a total sum that includes the pollen main sum (i.e. without *Pinus*) and the sum of spores and other continental NPPs (van Geel et al., 1972; Cugny et al., 2010; Miola, 2012).

3.3.2. Statistical analysis on palynological results

Palynological diagrams of pollen and dinocyst assemblages were performed with the Tilia software (Grimm, 1990), also defining the more parsimonious statistically homogeneous palynological zonations according to the CONNIS model (Grimm, 1987).

Taxonomical diversity indexes were calculated using the "PAST version 4.06b" software (Hammer et al., 2001), including the species richness (i.e. number of taxa per sample), the Margalef's richness index (diversity index), and the dominance index (i.e. the value "0" indicates equal presence of all taxa while the value "1" indicates the dominance of one taxon in the assemblage). In addition, multivariate analyses (Detrended Correspondence Analysis, DCA) were performed with the PAST program for semi-quantitative geochemical XRF data (cf. Data Availability section).

3.3.3. Dinocyst-inferred environmental reconstructions

Dinocyst-based sea-surface environmental quantifications were performed using R version 2.7.0 software (R Development Core Team, 2008; http://www.r-project.org/) and the Modern Analogue Technique (MAT; e.g. Guiot, 1990; Guiot and de Vernal, 2007). This method consists of selecting (based on a dissimilarity index) a limited number of analogue surface dinocyst assemblages and associated environmental values. A modern surface database is thus required. Dinocyst fossil assemblages were compared to the most recent standardized Northern Hemisphere "modern" database (n=1,968 sites; de Vernal et al., 2020), recently upgraded with new modern assemblages of the Western Mediterranean Basin (WMB; + n=23: 6 in the Gulf of Lion and 17 in the AM; Coussin et al., 2022). The dinocyst dataset includes 71 different taxa in relation with 17 modern environmental parameters (de Vernal et al., 2020). Five modern analogues were found by the MAT, which allowed to calculate environmental parameters considering an average of related parameter values, with the maximum weight attributed to the statistically closest analogue (e.g. Guiot and de Vernal, 2007). Considering the statistical threshold distance of the MAT (d_T= 1.2), analogues are considered as i) remote when the distance $d > d_T$, acceptable when $d_T/2 < d < d_T$, and good when $d < d_T/2$ (de Vernal et al., 2005). Root Mean Square Errors (RMSE) are used to discuss uncertainties in fossil quantifications, often caused by the lack of corresponding modern analogues of fossil assemblages (Guiot and de Vernal, 2007; de Vernal et al., 2020). In this study, we have estimated summer and winter sea surface temperature (SST_{winter} and SST_{summer}; RMSE of 1.2°C and 1.8°C, respectively), sea surface salinity (SSS_{winter} and SSS_{summer}; RMSE of 1.1 psu and 2.1 psu, respectively), and mean annual Primary Productivity (PP_{annual}; RMSE of 436.1 gC m^{-2} yr^{-1}).

3.3.4. Pollen-inferred climate reconstruction

Pollen reconstructions were also generated with the MAT applying the same general principles as for the dinocyst-based reconstructions. In this case, the method calculates a dissimilarity index between fossil pollen obtained on core MD04-2801 and modern pollen assemblages extracted from the database updated in Dugerdil et al. (2021). Modern climate parameters associated with the best analogues are then weighted (according to the similarity of the best four analogues) to provide values for fossil-pollen assemblages. Climate reconstructions were obtained with a leave-one-out approach. In this study, the climate variables are Mean Temperature of the Coldest Month (MTCO; RMSE of 4.7°C), Mean Temperature of the Warmest Month (MTWA; RMSE of 2.6°C), Annual Temperature (TANN; RMSE of 3.1°C),

Annual Precipitation (PANN; RMSE of 199 mm/yr), and Summer Precipitation (SUMMERPR; RMSE of 51.3 mm/summer). We also calculated a temperature seasonality index as the difference between MTWA and MTCO reconstructions using the Rioja package in R (Juggins, 2012).

3.4. Biomarker analyses

Biomarker analyses were performed at a temporal resolution of about 150 years. Lipids were extracted from 1.5 to 2 g of freeze-dried sediments using a mixture of dichloromethane/methanol (2:1 v/v). Silica gel chromatography was used to isolate alkenones and n-alkanes from the total lipid extracts. They were then analysed by gas chromatography, following Sicre et al. (1990). We used the global calibration from Conte et al. (2006) to convert the unsaturation ratio of C_{37} alkenones ($U^{k'}_{37} = C_{37:2}/(C_{37:2} + C_{37:3})$ into sea surface temperature (SST) using the following equation ($SST = -0.957 + 54.293(U^{k'}_{37}) - 52.894(U^{k'}_{37})^2 + 28.321(U^{k'}_{37})^3$).

Simultaneously, high molecular-weight terrestrial n-alkane concentrations were determined. The C_{29}, C_{31}, C_{33} and C_{35} homologues produced from higher plants were quantified. Their sum, thereafter named TERR-alkanes, was used to reflect terrestrial inputs to the studied site (Castañeda et al., 2009; Jalali et al., 2017). Vegetation types can be distinguished based on the relative homologue distribution of leaf wax n-alkanes. Deciduous trees and shrubs are thought to mainly produce n-alkanes with n-C_{27} and n-C_{29} while grasses and herbs mainly produce n-C_{31} and n-C_{33} (Vogts et al., 2009; Schäfer et al., 2016; Bliedtner et al., 2018). Average Chain Length (ACL) of n-alkanes was also calculated to produce information on water availability and compare this to vegetation-type indicators from pollen analyses (Jalali et al., 2017).

4. Results

4.1. Age model of core MD04-2801

The age model of core MD04-2801 was built by integrating 20 AMS ^{14}C dates (11 from the ARTEMIS spectrometer of the Laboratoire de mesure du Carbone 14, CEA Paris-Saclay, and nine from the ECHoMICADAS spectrometer; Table 1): 18 samples consist of monospecific planktonic foraminifera (*G. bulloides*) and two samples consist of gastropods (Table 1). All radiocarbon dates were calibrated using the CALIB 8.2 software (Stuiver and Reimer, 1993) and the IntCal20 calibration curve (Reimer et al., 2020), first considering a reservoir age of -400 years (Siani et al., 2000). To establish the age model (Figure 2), the rbacon package (Blaauw and Christen, 2011) was used under R (version 4.1.0; R Development Core Team, 2021; http://www.r-project.org/). Two dates were discarded at 931 cm (large analytical error of 270 years; Table 1) and 31 cm (considered as an outlier regarding the first 4 m of the core; yellow diamonds in Figure 2).

It is worth noting that the stratigraphy of the upper section is suspected to be influenced by a core disturbance by piston effect. This is supported by decreasing values of the sediment density from 250 cm upward, with very low Vp values between 140 and 90 cm (Figure 2). For this reason, the age model was calculated independently for the upper (431 to 0 cm) and lower (1,031 to 431 cm) parts of the studied core, and then brought together (Figure 2). Considering the density as the artefact clue, abrupt change in sedimentation rates at 431 cm (Figure 2) is suggested while the artefact in the sampling appears from 250 cm upward. Furthermore, laminations are visible below 400 cm but less clear above this level (especially from 250 cm upward), where sediments appear to be more homogenous (Figure 2). At the MD04-2801 core site, situated beyond the crest of a turbidite channel-levee system, the expected sedimentary record could be composed of hemipelagites and fine-grained turbidites from turbidity currents overspilling the levee. These high accumulation rates (i.e. around 150 cm/kyr on the 431–0 cm section; Figure 2) cannot therefore be expected to reflect gravity-driven sedimentary processes. In light of these features, a coring artefact in MD04-2801 is probable (Figure 2). Overall, a robust chronology is assumed from 431 cm to the base of the core with average sedimentation rates of about 40 cm/kyr (stable Vp and density values with a two-step density trend at around 870 cm; Figure 2), while a less robust chronology is assumed from 431 cm upward with a two-step trend in physical sediment properties. From 431 to 250 cm, well-layered sediments, as observed in the basal section, correspond to a strong increase in density values and still stable Vp values and may be related to an acceleration in sedimentation rates (280 cm/kyr; Figure 2).

From 250 cm upward, the creep of sediments appears very likely affected by the piston effect (strong decrease in density values at 250 cm and unexpected low Vp values between 120 and 70 cm). According to the age model (Figure 2), the base of the studied core is dated at 14 cal ka BP.

4.2. Sedimentological signals

The core MD04-2801 mainly consists of homogeneous silty sediments that can be separated by six limits (a to f in Figure 3) based on the trends in graphs of sedimentological parameters. KMDJ23 is a core very close to the MD04-2801 coring site whose top sample (water-sediment interface) was analyzed and presented in Coussin et al., 2022 (https://doi-org.scd-proxy.univ-brest.fr/10.1016/j.marmicro.2022.102157). It constitutes a modern assemblage useful as a reference point.

4.2.1. X-ray Fluoresence

In order to investigate the co-occurrences of major elements of the XRF dataset, we performed a Detrended Component Analysis (DCA) on selected elements (Ca, Si, Al, K, S, Ti, Fe, Mn, Sr; cf. Data in brief). In the study area, the silico-clastic detrital signature is well expressed by Ti and Fe, while Si and Al are the main chemical components of alluminosilicates. Ti, FE, Si and Al show similar trends suggesting that these elements potentially relate to the clayey fraction formed by the chemical alteration of soils. Conversely, common patterns of Sr and Ca point to biomineralized and/or detrital carbonates. The DCA statistical analysis (Data in Brief) led to the most relevant XRF ratios for the following discussion. Given the difficulty in deconvoluting terrigenous and marine sources in the Ca-XRF signature, we considered both Ca/Al-XRF (mixed detrital-biogenic signature, Figure 3a) and Ti/Al-XRF (detrital signature; Figure 3b) for the paleoenvironmental interpretation conducted in the AM sediments. Both ratios generally show similar fluctuations in temporal variations over time and amplitudes, suggesting a stronger detrital source in the Ca-XRF signature except for two intervals characterized by high Ca/Al-XRF and low Ti/Al-XRF ratios from the base of the core to 910 cm (limit “b”) and between 575 and 485 cm (limits d and e). The Ti/Ca-XRF ratio is considered as primarily detrital and linked to silico-clastic *versus* carbonate sources to the AM.

4.2.2. Magnetic Susceptibility and grain size

The Magnetic Susceptibility (MS) signal shows distinct fluctuations between 3.8 and 17.5 SI. Three main phases are identifed with average values of 9.2 SI from the base to 910 cm (limit

"b"), of 14.3 SI between 910 and 370 cm (limit "f") and of 11.6 SI from 370 cm upward (Figure 3c).

In addition, according to the high-resolution grain-size data of total sediments (Data In Brief), the 4–63 µm fraction largely dominates (silt, average of 66%), followed by the fraction <4 µm (clay, average of 23%) and the fraction >63 µm (sand, average of 11%). More specifically, from the base of the sequence to 910 cm (limit "b"), the high proportion of the >63 µm fraction (Figure 3d) is associated with low amounts of ferro-magnetic minerals (low MS values; Figure 3c), high Ca/Al values *versus* low Ti/Al (Figure 3 a,b), and extremely low median (D50) grain size of $CaCO_3$-free sediments *versus* high D50 grain size of total sediments (Figure 3d). This may indicate that coarser sediments are mainly inherited from the erosion of carbonate formations, with little advection of small-sized silico-clastic and ferro-magnetic sediments.

Then, from 910 cm (limit "b") to 370 cm (limit "f"), higher MS values (Figure 3c) combined with D50 values of $CaCO_3$-free sediments higher than D50 values of total sediments (Figure 3d) indicate increasing advection of silico-clastic and ferro-magnetic silto-clayey material with a lower proportion of detritic carbonate particles. Across limits "b" to "f", the coarsest detrital particles of the mix (silicates and carbonates) are particularly evident in the 740–575 cm interval (between limits "c" and "d" or interval "c-d"), and correspond to two remarkable peaks of sandy sediments at 580 and 600 cms (Data in Brief). It is worth noting that the 575 to 485 cm interval ("d-e") coincides with the second interval of high Ca/Al-XRF values (as in zone "a-b") and lower D50 grain-size values (Figure 3d), with coarser sediments corresponding to silty rather than sandy particles as in the interval "a-b".

From 370 cm (limit "f") to 250 cm, MS values as well as grain-size properties point to finer silto-clayey sediments (Figure 3c). Finally, from 250 cm upward, wide ranges of coarse *versus* fine-sediment fluctuations (Data in Brief), associated with low D50 grain-size values (Figure 3d), can be reconciled by invoking a small proportion of very coarse sediments which would bias the mean but hardly alter the particle-size medians. A grey band in Figure 3 highlights this section, suspected to be affected by core disturbance through piston effect.

4.2.3. Clay mineral composition

Clay mineral averages are about 8% of Illite-Smectite (Interstratified), 18% of Chlorite, 32% of Kaolinite and 43% of Illite (Data In Brief). Clay results are represented as anomalies relative to the mean of each dataset (Data In Brief). Due to high sedimentation rates (around 50 cm/kyr; Figure 2), palygorskite was not significantly detected. The boxes in Figure 3g highlight the Majorly different clay mineral phases (relative to their mean values). The two intervals of

enhanced Ca/Al-XRF values ("a-b" and "d-e") are also characterized by the highest interstratified values and lowest kaolinite percentages. Conversely, kaolinite percentages increase during intervals of both increasing proportions of clays and finer grain-size sediments ("b-c" and "e"-250cm). This suggests that increasing kaolinite values could evidence strengthened chemical alteration on land. We consequently use the Kaolinite/Illite ratio as a proxy of chemical alteration throughout the sequence.

4.3. Stable isotope signals

4.3.1. Carbon isotopes in foraminifera

The $\delta^{13}C$ values of endobenthic *Globobulimina affinis* and planktonic *Globigerinoides bulloides* foraminifera range between -0.9 and -2.1‰ (mean of -1.6‰) and between -0.6 and -2‰ (mean of -1.1‰), respectively (Figure 3e). Planktonic and endobenthic $\delta^{13}C$ signals show similar values until 740 cm (limit "c"), but exhibit a significant offset (average of 0.7 ‰) after 575 cm (limit "d").

Heavier planktonic $\delta^{13}C$ values observed during the interval "a-b", as well as after 575 cm (limit "d") reveal strong primary productivity. Conversely, the $\delta^{13}C$ of endobenthic foraminifera generally reflects the $\delta^{13}C$ of pore waters, which depends on the export flux of organic matter and availability of dissolved oxygen in bottom waters (e.g. McCorkle et al., 1990; Mackensen & Licari, 2003; Fontanier et al., 2006). Lighter benthic $\delta^{13}C$ values after limit "b" may be indicative of remineralization of enhanced organic matter in bottom sediments.

4.3.2. Oxygen isotopes

Endobenthic (*G. affinis*) and planktonic (*G. bulloides*) $\delta^{18}O$ values range between 2.1 and 4 ‰ (mean of 2.6 ‰) and between 0.4 and 2.2 ‰ (mean of 0.8 ‰), respectively, and show similar patterns throughout the sequence (Figure 3f). Heavier $\delta^{18}O$ values (colder sea surface temperatures) in the interval "a-b" are reflected by values of 1.9 and 3.8 ‰ for planktonic and endobenthic taxa, respectively. Lighter mean $\delta^{18}O$ values after limit "b" are stable around 0.6 ‰ (standard deviation of 0.2 ‰) and 2.4 ‰ (standard deviation of 0.1 ‰) for planktonic and endobenthic taxa, respectively. However, wider ranges of planktonic $\delta^{18}O$ isotope value variations, with slightly lower values since interval "b-d", may be indicative of either decreasing salinities and/or increasing temperatures.

4.4. Palynological analyses

4.4.1. Dinoflagellate cysts

- *Diversity and concentrations*

Thirty-nine different dinocyst taxa were identified over the whole sequence, with a mean species richness of 18 different taxa per slide (Figure 4a). Species richness is lower than average from the base of the sequence to limit "a" (1,025 cm), in the "b-d" interval (910–575cm), and after limit "e". Conversely, species richness is higher than average in "a-b" (1,025–910 cm) and "d-e" (575–485 cm) intervals. Both intervals are also characterized by low kaolinite percentages and high Ca/Al-XRF values, as well as heavy planktonic $\delta^{13}C$ values.

The dinocyst dominance index (Figure 4a) is systematically explained by the major taxa *Brigantedinium*. The dinocyst diversity (Figure 4a), as reflected by the Margalef index (similar to species richness), shows opposite trends compared to *Brigantedinium* spp.; the lowest diversity being synchronous with high *Brigantedinium* spp. percentages.

Total dinocyst concentrations, mainly explained by *Brigantedinium* spp. occurrences, range between 450 and 29,000 cysts/cm^3, with mean values of around 3,300 cysts/cm^3 (Figure 4a). Dinocyst concentrations show higher values during intervals "a-b" (1,025 to 910 cm) and "d-e" (575 to 485 cm), both previously described by a stronger diversity. We thus plotted the concentrations of all dinocysts without *Brigantedinium* spp. against the concentrations of *Brigantedinium* spp. alone in order to evaluate the respective contribution of these heterotrophic taxa with regards to the rest of the dinocyst community (Figure 4a). Up to limit "b", other dinocysts are higher than *Brigantedinium* spp. (around 10,000 *versus* 2,000 cysts/cm^3). They follow similar patterns between limits "b" and "e" (around 1,500 cysts/cm^3) and, after limit "e", all other dinocyst concentrations are slightly lower than *Brigantedinium* spp. (1,000 vs. 1,500 cysts/cm^3). Dinocyst concentrations show lower values but similar evolution compared to pollen grain concentrations throughout the sequence, except for similar concentrations obtained from 1040 cm to limit "b" and during the interval "d-e" (575–485 cm).

- *Dinocyst assemblages and dinocyst zones*

Dinocyst assemblages are dominated by eight autotrophic taxa: *Nematosphaeropsis labyrinthus, Impagidinium aculeatum, Spiniferites mirabilis, Operculodinium centrocarpum, Spiniferites bentorii, Spiniferites membranaceus,* cysts of *Pentapharsodinium dalei, Lingulodinium machaerophorum* and seven heterotrophic taxa including *Echinidinium* spp., *Selenopemphix quanta,* cysts of *Protoperidinium nudum, Selenopemphix nephroides,*

Lejeunecysta spp. (grouping of *L. oliva* and *L. sabrina*), *Trinovantedinium* spp. and *Brigantedinium* spp. (Figure 5a).

The dinocyst assemblages led us to consider four main limits, thus five palynozones (MD04-1 to MD04-5; Fig. 5). These boundaries/zones are based on the CONNISS cluster analysis performed on dinocyst assemblages (threshold used is 11; Figure 5a). These four limits also correspond to four sedimentological limits (a-b-d-e; Figs. 3 and 4). Zone MD04-1, from the base of the sequence to limit "a", is characterized by the dominance of *Brigantedinium* spp., *S. mirabilis* and *O. centrocarpum*. The second zone MD04-2 (interval "a-b") is marked by increasing values of *N. labyrinthus* reaching 20 to 40%, associated with the increase in *B. tepikiense, S. lazus* and *O. centrocarpum.* Zone MD04-03 (interval "b-d") is characterized by a high plateau of *Brigantedinium* spp. up to ca. 40%, associated with the increase in *I. aculeatum* (up to 15 %) and *S. mirabilis*, especially in the interval "c-d", and a progressive decrease in *O. centrocarpum* percentages. Zone MD04-4 (interval "d-e") shows a sharp drop in *Brigantedinium* spp. percentages reaching 20%, while *S. mirabilis* increases to 30%. Finally, zone MD04-5 (from limit "e" onward) is characterized by the highest values of *Brigantedinium* spp. (about half of the total assemblage) associated with *S. mirabilis* (around 15%). A full description of main dinocyst results is available in Data in Brief.

4.4.2. Pollen grains

- *Diversity and concentrations*

Seventy-one different pollen taxa were identified for the whole sequence, with a mean species richness of 28 different taxa per slide (Figure 4b). Species richness ranges between 18 and 29 taxa per slide with lower values between limits "c" and "f "(740 to 370 cm) which also correspond to the strongest representation of forest taxa (cf. percentages of total trees and total trees with *Pinus*; Figure 4b). In contrast, increased diversity coincides with the diversification of herbaceous plants. Mean total pollen concentrations are approximately of 6200 grains/cm^3 (ranging between 1300 and 25,000 grains/cm^3); the highest values are in intervals "a-b" (1,025 to 910 cm) and "d-e" (575 to 485 cm), as for dinocysts, and above 250 cm (removed from the discussion).

Pinus concentrations follow the same trend as total pollen concentrations that are mainly driven by trees (especially *Quercus*). Strong pollen production, enhanced river transport, and finer grain-sized sediments, are crucial factors contributing to increase pollen-grain concentrations. However, the strong link between pollen (terrestrial compartment) and dinocyst (marine realm)

concentrations point to a common mechanism of organic matter export to the AM and sedimentation processes.

- *Pollen and Non-Pollen Palynomorph (NPP) assemblages and pollen zones*

The zones defined on the basis of dinocyst assemblages have also been used for pollen assemblages to facilitate land-sea comparison (Figure 5b). Zone MD04-1 is characterized by the dominance of herbaceous pollen taxa, mainly Cichorioideae and Poaceae. Zone MD04-2 is marked by the strong increase in the altitudinal taxa *Cedrus* (reaching maximum percentages above 40% at 1001 and 961 cm), associated with semi-desert, steppic pollen taxa (i.e. *Ephedra* and *Artemisia*) and coastal-steppic taxa (i.e. Amaranthaceae). Zone MD04-3 is characterized by the progressive increase in arboreal taxa (especially *Quercus ilex*), associated with strong occurrences of herbaceous taxa (Cichorioideae and Poaceae) until 740 cm (limit "c"). In zone MD04-3, limit "c" corresponds to the onset of the strongest forest representation, largely represented by *Quercus*, associated with Cupressaceae, as well as Mediterranean forest (*Olea, Pistacia*) and open vegetation (i.e. Cichorioideae and Poaceae) taxa. Interestingly, from limit "c", freshwater algae occurrences also increase. Zone MD04-3 is also marked by increasing abundance of *Glomus* spores and Ascospores. Zone MD04-4 shows a strong representation of arboreal taxa (up to 40%) associated with a slight decrease in open-vegetation taxa (Cichorioideae, Poaceae). Coastal-steppic taxa (Amaranthaceae), with slight increases in *Ephedra* and *Artemisia*, also correspond to decreasing occurrences of *Glomus* spores. Finally, zone MD04-5 is characterized by the progressive decrease in arboreal taxa (especially *Quercus*) favoring the synchronous increase in open-vegetation taxa (Cichorioideae, Asteroideae, Poaceae). Additionally, percentages of semi-desert taxa (*Ephedra* and *Artemisia*) somewhat increase with those of *Olea*, and *Glomus* spore occurrences progressively increase. Modern climate-landscape relationships in Eurasia and northern Africa (Woodwards, 1987; Peyron et al., 1998) will be considered for pollen interpretation. A full description of main pollen results is available in Data in Brief.

4.4. Palynological quantification

For dinocyst-inferred sea-surface reconstructions, the maximum number of selected analogues is five (Figure 4) Also, a threshold of 1.35 is adopted by the MAT (Modern Analogue Technique) to exclude too dissimilar assemblages. In this study, Dmin varies around an average value of 0.87: no analogue was selected for six levels (440, 664, 800, 948, 992, 1000 cm), only one analogue for four levels (60, 746, 860, 932 cm), two analogues for one level (976 cm), three

analogues for three levels (976 cm), four analogues for nine levels (340, 532, 696, 760, 872, 880, 920, 1026, 1040 cm) and five analogues for the 63 other levels, testifying for statistical robustness of the reconstruction for about three quarters of the analysed samples.

For pollen-inferred climate reconstructions, the number of selected analogues is always four. Appropriate analogues are selected through cross-validation based on the leave-one-out approach. Stable Dmin values are about 0.39 from 1,040 cm to limit "e" and about 0.47 from limit "e" to the top of the sequence, testifying to the robustness of reconstructed climatic parameters.

Considering hydrological (cf. dinocyst-based quantifications) and climate (cf. pollen-based quantifications) parameters, SST and SSS are discussed in parallel with annual precipitation and temperature seasonality. The exhaustive dataset of reconstructed environmental parameters is available in Data in Brief.

4.5. Molecular biomarkers

Concentrations of C_{37} alkenones, plotted as the sum of $C_{37:2} + C_{37:3}$, range from 18 to 328.5 $ng.g^{-1}$, with a mean value of about 75.6 $ng.g^{-1}$ (Figure 4a). The $\sum C_{37}$ follows the same trend as that of palynomorph (dinocyst and pollen) concentrations along the sequence, with higher values in the oldest interval "a-b" (1,025 to 910 cm), highlighting the common pattern in organic matter export and preservation through both biomarker and palynological approaches.

Concentrations of TERR-alkanes range between 354 and 1,071 $ng.g^{-1}$, with a mean value of 643 $ng.g^{-1}$(Figure 4b). Up to limit "b" (910 cm), they decrease to the lowest values of the record (379 $ng.g^{-1}$). From limits "b" to "d", TERR-alkane concentrations are generally higher and highly variable with above average values. They broadly decrease during intervals "d" to "f" and increase again until 370 cm before decreasing up to the top of the studied core.

Finally, the ACL (Average Chain Length; Figure 4b) calculated from the n-alkane distribution shows increasing values from interval "a" to "d", suggesting a gradual dryness (expressed by high ACL values), followed by stable values up to limit "f", followed by decreasing values close to the mean of the dataset (30,1) up to the top of the studied sequence. Mean values of the ACL are generally consistent with our palynological data underlying a strong representation of open vegetation along the sequence.

5. Discussion

5.1. Palynomorph preservation and the signature of *Brigantedinium* spp.

Fine-grained (silto-clayey) sediments and high sedimentation rates (ca. 50 cm/kyr) recorded with core MD04-2801 may have favored conditions for the preservation of fossilized palynomorphs (dinocysts and pollen grains). A recent study of the modern distribution of pollen grains in the WMB suggested that modern pollen assemblages in our study area are representative of the adjacent vegetation (e.g. *Quercus ilex*, Amaranthaceae and Cichorioideae; Coussin et al., 2022). However, previous studies have investigated taxa sensibilities to oxidation effects (e.g. Havinga, 1967, 1971; Lebreton, 2009). It has for exemple been shown that *Quercus* and Cichorioideae pollen grains are not very sensitive to degradation and could be overrepresented in pollen assemblages at the expense of other taxa. The intact aspect of all pollen grains throughout the sequence leads us to hypothesize that pollen are mainly from the coastal Algerian catchments and that over-representation of the main taxa is unlikely. Regarding dinocyst taxa, *Brigantedinium* spp. are dominant and show large fluctuations (ca. 10 to 80 %; Figure 4a, 6j) throughout core MD04-2801. *Brigantedinium* spp. are often interpreted as witnessing upwelling regimes (e.g. Marret, 1994; Zonneveld et al., 1997, 2001; Bouimetarhan et al., 2009; Penaud et al., 2016; Coussin et al., 2022). Moreover, modern occurrences of *Brigantedinium* spp. in surface sediments of the western Mediterranean Basin (around 20%; Coussin et al., 2022) in association with *T. applanatum*, *Lejeunecysta* spp., *Echinidinium* spp., *S. nephroides* and grouped *Selenopemphix quanta* and *Protoperidinium nudum*, also allowed to assign these taxa to productive surface waters and were used to highlight the major haline-upwelling front associated with the AC, itself depending on the vigour of the Alboran gyres (Coussin et al., 2022). *Brigantedinium* spp. peaking values of ca. 80% over the Holocene (Figure 6i) were never reached in western Mediterranean modern surface sediments, even along the AC (Coussin et al., 2022). Since *Brigantedinium* spp., as well as *Echinidinium* spp., are well-known for their strongest sensitivity to oxic conditions (e.g. Zonneveld et al., 1997; Kodrans-Nsiah et al., 2008; Bogus et al., 2014), their percentages must be interpreted carefully as direct tracers of primary productivity. Indeed, it has been shown that their occurrences in sediments decrease logarithmically with increasing bottom water oxygen content (Zonneveld et al., 2001, 2007, 2008). Our reconstructions therefore raise questions about potential taphonomic biases that may have affected dinocyst assemblages.

The MD04-2801 core retrieved at a water depth of 2,063 m is located in the water depth range of the Western Mediterranean Deep Waters (WMDW). The WMDW, as well as Ligurian

Intermediate Waters (LIW), contribute to the Mediterranean Outflow Water (MOW) export at the Gibraltar Strait (Stommel et al., 1973; Lionello et al., 2006) which varied through time (e.g. Voelker et al., 2006; Toucanne et al., 2007; Peliz et al., 2009; Rogerson et al., 2010; Bahr et al., 2014, 2015; Voelker and Aflidason, 2015; Hernández-Molina et al., 2014). Stronger LIW during cold climate events (Toucanne et al., 2012) such as the Younger Dryas (YD), implying a stronger WMB ventilation, is also supported by Alboran Sea records (Mc Culloc'h et al., 2010). In contrast, warmer Holocene conditions, and especially the Sapropel 1 event (10.8 ± 0.4 to 6.1 ± 0.5 ka BP) in the Eastern Mediterranean Basin (e.g. Kallel et al., 1997; Bar-Matthews et al., 2000, 2003; Mercone et al., 2000; Rohling et al., 2002; Tachikawa et al., 2015), are characterized by a weakened/cessation of the LIW formation (e.g. Toucanne et al., 2012). This shift from well-ventilated bottom waters during the YD to less-ventilated ones during the Holocene optimum (ca. 9.5-6.5 ka BP) may respectively correspond to low (around 20% such as today) or high (> 40%) percentages of *Brigantedinium* spp. (Figure 6i). There is therefore a risk that *Brigantedinium* spp. relative abundances may be modulated by oxygenation conditions despite the high sedimentation rates recorded at our studied site. In this context, Zonneveld et al. (2007) suggested to use absolute concentrations of phototrophic rather than heterotrophic taxa (or total dinocyst) ones, combined with dinocyst diversity (or species richness), to better assess productivity conditions. In the following discussion, these recommendations are considered to limit potential biases due to diagenesis or ventilation when discussion dinocyst assemblage reconstructions.

5.2. From the Bölling-Alleröd to the Younger Dryas

5.2.1. Hydrological conditions

Alkenone SSTs show a strong cooling from the Bölling-Alleröd (B/A: zone MD04-1) to the Younger Dryas (YD: zone MD04-2 or "a-b"; Figure 6) featuring the lowest SST values (i.e. 15.5°C; 4.1°C below modern annual SSTs), consistent with the heaviest planktonic $\delta^{18}O$ values greater than 2‰ (Figure 6a,b). These low temperatures corresponds to the lowest reconstructed seasonality values (Figure 7h). This cold SST trend is synchronously observed in both the WMB sequences (Figure 8d,h,k,n,q). During the YD, cool-water dinocyst taxa (*N. labyrinthus*, *B. tepikiense* and *S. lazus* ; Figure 6c) dominating today polar to subpolar environments (Rochon et al., 1999; Van Nieuwenhove et al., 2020) show maximum percentages, while dinocyst-derived SSTs are not able to provide modern analogues representative of the environmental conditions of this cold climate event (Figure 6b). Indeed, all selected analogues

had statistical distances higher than the accepted threshold (cf. Data in Brief). SSTs lower by 3.5 and 8.5°C with respect to present-day winter conditions were reconstructed using foraminifera and dinocysts in SW Portugal and Cadiz-NW Morocco, respectively (Penaud et al., 2011). At these northeastern Atlantic subtropical sites, the same YD assemblages (*N. labyrinthus*, *B. tepikiense* and *S. lazus*) were observed with slight differences in percentages: *B. tepikiense* hardly occurred in the Gulf of Cadiz and further south, while *S. lazus* was not found off Portugal (Penaud et al., 2011). These observations support the mixed northern and subtropical North Atlantic influences in the AM. Also, as observed in the Alboran Sea (Turon and Londeix, 1988), *N. labyrinthus*, a stratigraphical marker of the YD, testifies of the southward shift of the bioclimatic belts during this cold event of the last deglaciation. In the AM, percentages around or slightly higher than 30% are closer to those reconstructed off the Iberian margin (slightly higher than 20%) than in NW Morocco (about 5%), and point to an enhanced advection of cold Atlantic waters in the WMB. In addition, *O. centrocarpum* (i.e. North Atlantic taxon) shows four-time stronger representation than *L. machaerophorum* estuarine taxon, suggesting the prevailing oceanic influence in the AM and associated low fluvial input (Figure 5a). This is supported by the higher values of Ocen/Lmac dinocyst ratio for all the compared WMB sites (Fig. 8)

Heavy planktonic $\delta^{13}C$ values (Figure 6g) and higher concentrations of alkenones (Figure 4a) and phototrophic dinocyst concentrations (Figure 6f) as well as a strong dinocyst diversity (Figure 4a) suggest enhanced primary productivity, despite lower percentages of *Brigantedinium* spp. (Figure 6i) that may result from a lower preservation of heterotrophic cysts under stronger bottom-water ventilation (cf. section 5.1). More productive conditions may be attributed to a stronger vigour of the AC resulting from the strengthening of the Alboran gyres during the YD (Combourieu-Nebout et al., 1999; Barcena et al., 2001; Penaud et al., 2011; Rouis-Zargouni et al., 2012; Ausín et al., 2015). This finding can also be explained by enhanced vertical mixing triggered by stronger winds replenishing surface waters with deep water nutrients.

5.2.2. Climate and continental context

Enhanced YD productivity could result from fertilization of the photic zone by Saharan dust deposition (Moreno et al., 2002; Bout-Roumazeilles et al., 2007; Jimenez-Espejo et al., 2008; Rodrigo-Gamiz et al., 2011; Bout-Roumazeilles et al., 2013). Unfortunately, the clayey fraction of core MD04-2801 only represents ca. 20% of the sediment lithology. The high sedimentation rates (ca. 50 cm/kyr), mainly characterized by silts, do not allow characterizing aeolian-

743 transported clayey minerals such as the typical palygorskite signature which is drowned in other
744 clayey minerals amount signals.
745 During the YD, the strong representation of semi-arid (*Artemisia, Ephedra*) and steppic-coastal
746 (Amaranthaceae) taxa, and the weak representation of Mediterranean forest taxa indicate
747 extremely dry conditions characterized by an open and steppic landscape (Figure 7g). This open
748 landscape is expressed by the lowest forest taxa representation in the WMB sequences (Figure
749 8g,j,m,p). Previous studies in the Western Mediterranean Sea already showed this cold-dry
750 event as characterized by a first dry phase followed by a more humid period (e.g. Combourieu
751 Nebout et al., 1998, 2002; Turon et al., 2003; Naughton et al., 2007; Kotthoff et al., 2008;
752 Fletcher and Sanchez-Goñi, 2008; Dormoy et al., 2009; Combourieu-Nebout et al., 2009;
753 Desprat et al., 2013). This bipartite structure is not obvious at the resolution of our study, except
754 for a slight decreasing trend of *Artemisia* from the start to the end of the YD (Figure 5b).
755 Additionally, increasing ACL values from 29.8 to 30.2 (Figure 4b) are consistent with a higher
756 plant adaptation to water stress.
757 The YD sedimentary facies of core MD04-2801 highlights coarse carbonate sediments with
758 minor advection of small-sized silico-clastic and ferro-magnetic sediments (Figure 3d).
759 Consequently, arid conditions during the YD, as revealed by pollen grains, may have favored
760 erosion of sedimentary formations onland and aeolian transport of carbonate particles amplified
761 by strengthened atmospheric circulation. Indeed, low Kaolinite values (cf. Data in Brief)
762 suggest reduced chemical alteration, while low concentrations of *Glomus* spores evidence weak
763 runoff due to low precipitations (Figure 7c). Sporadic but intense erosive runoff events may be
764 linked to peaks of reworked cysts originating from the alteration of Tertiary carbonate
765 formations (Figure 5a). Indeed, Algerian oued discharge intensifies during intense rainfalls
766 events responsible for flash floods with strong erosive effects. However, the scarce occurrences
767 of continental NPPs and generally low concentrations of reworked dinocysts rather attest low
768 alteration and low fluvial delivery to the AM.
769 Finally, unusual occurrences of *Cedrus* (about 20 %, peaking at 40 % ; Figure 7j) are recorded.
770 Considering the modern distribution of *Cedrus atlantica* in Northern Africa (Bell et al., 2019),
771 in the highest altitudinal vegetation belts (Ben Tiba and Reille, 1982; Stambouli-Essassi et al.,
772 2007), and the modern distribution of *Cedrus* percentages (around 0.5%) in KMDJ-23 core
773 (Coussin et al., 2022), we suggest that a wider altitudinal *Cedrus-Pinus* forest developed in the
774 high reliefs of the Tell Atlas. Even if stronger aeolian transport of coniferous pollen grains
775 better dispersed by winds than other pollen grains is possible under stronger atmospheric
776 circulation, synchronous peaks of *Cedrus* and reworked cyst concentrations (Figure 4), rather

suggest remaining mild conditions in altitudinal zones enhancing fluvial transport (i.e. strong seasonal erosive runoff) of *Cedrus,* even under the prevailing arid conditions of the YD.

5.3. The Early Holocene (11.7–8.2 ka BP)

5.3.1. Delayed Mediterranean forest expansion

The Early Holocene is characterized by a strong decrease of the semi-arid and coastal-steppic vegetation (Figure 7g), replaced by typical mattorals (xerophytous open vegetation) mainly represented by Cichorioideae (Figure 5b). At the same time, the altitudinal forest represented by *Cedrus* is no longer recorded along the Holocene with high percentages (i.e. values close to modern ones; Figure 7j), due to reduced extent of these altitudinal vegetation belts in the Atlas Mountains in a context of increasing temperatures allowing other taxa to colonise altitudinal belts. Previous studies also discussed the limited altitudinal area where *Cedrus* retracted at the YD-Holocene transition, while warmer Holocene conditions favors the evergreen *Quercus* forest expansion (Marret and Turon, 1994; Cheddadi et al., 1998, 2009; Zielhofer et al., 2017). Until 8 ka BP, the progressive increase of Mediterranean forest taxa, combined with the persistent signature of the open vegetation (e.g. Cichorioideae, Poaceae; Figure 7 f,g), suggest a progressive increase of moisture, which is a critical limiting factor for the forest expansion in the southern Mediterranean area (Quezel, 1999). Increasing moisture is also supported by sedimentological, bioindicator, and biochemical runoff tracers (i.e. higher magnetic susceptibility (Figure 7e) and Ti/Ca-XRF values (Figure 6h), higher concentrations of *Glomus* spores (Figure 7c) and of pre-quaternary cysts (Figure 4a), higher TERR-alkane fluxes (Figure 7d)). In the AM, *Quercus* maximal values thus appear delayed, while Mediterranean mattorals (mainly represented by Cichorioideae, Poaceae and Asteraceae) associated with typical sclerophytous trees (*Olea* and *Pistacia*), are still observed.

The delayed expansion of forest appears consistent with current Mediterranean observations suggesting that, following moisture deficiency, three millennia are necessary for a full Mediterranen forest recovery (e.g. Combourieu-Nebout et al., 1998, 2002; Allen et al., 2002;; Turon et al., 2003; Naughton et al., 2006; Fletcher and Sanchez-Goñi, 2008; Jalut et al., 2009; Tzedakis, 2007; Fletcher et al., 2010; Zielhofer et al., 2017). The Early Holocene corresponds to the highest values of boreal summer insolation (Berger and Loutre, 1991; Figure 8b), responsible for high summer temperatures that may have enhanced summer Mediterranean droughts, therefore slowing down the development of trees, especially evident in the more sensitive eastern part of the basin (Figure 8m,p). Previous studies conducted in northwestern

Africa also discussed the maximal forest development at around 8.5 ka BP (Ballouche, 1986; Brun 1989; Lamb et al., 1989), consistently with the maximal values reached at the end of the Early Holocene in our study core (ca. 8 ka BP). Climate quantifications also suggest relatively low precipitation before 8.5 ka BP while the temperature seasonality indicates a strong thermal amplitude explained by high summer temperatures (Figure 7h). The Alboran Sea and by extension the AM are extremely sensitive to the Atlantic moisture through the influence of westerlies (i.e. for Mediterranean cyclogenesis). From 11.7 to 10 ka BP, the extended dry period post-YD has also been reported across the SW and NE Mediterranean basin (Dormoy et al., 2009) and is probably linked to a still weak influence of westerly cyclones (Kotthoff et al., 2008). Indeed, the North Atlantic storm tracks may have been maintained in a southern position under the influence of the Fennoscandian Ice Sheet still persistent until 9 ka BP (Magny et al., 2003). There, the forest expansion is directly in phase with the climate change of northern Atlantic latitudes (cf. NGRIP oxygen isotopes *versus* Alboran Sea forest signal in Figure 8a,g,j), in agreement with numeric simulations (Carlson et al., 2008). The Atlantic influence, and associated moisture transport, follows a decreasing gradient from west to east (Figure 8h,j,m,p) between the Alboran Sea to Algeria, whatever the climate interval considered over the last 14 kyrs.

5.3.2. Warmer oligotrophic conditions

In parallel with the Mediterranean forest expansion (Combourieu-Nebout et al., 1998, 1999, 2002, 2009), alkenone, dinocyst and planktonic $\delta^{18}O$ data (Figure 6a,b,c) point to a strong increase of SSTs at the start of the Holocene, with a 4.5°C increase of alkenone-based annual SST (i.e. from 16°C during the YD to ca. 20.5°C during the Holocene). It is worth noting that alkenone-based SSTs exhibit mean annual values consistent with the dinocyst-based SST seasonal variability range (Figure 6b). Furthermore, both alkenone- and dinocyst-derived SST, as well as percentages of cold water dinocyst taxa, point to slightly cooler SST conditions during the Early Holocene regarding the following conditions of the Middle Holocene. The warmest conditions are therefore not reached yet during the Early Holocene, and the prevalence of runoff signatures (significant peaks of *Glomus* and pre-Quaternary cysts; Figure 4a, 7a) may result from increasing moisture combined with a still high erodability of soils in a continental context of persistent opened landscape.

The Holocene transition is also characterized by a pronounced drop of dinocyst and alkenone C_{37} concentrations (Figure 4a), as well as lighter planktonic $\delta^{13}C$ values (Figure 7f), likely

accounting for less productive conditions. Interestingly, heterotrophic cyst percentages (Figure 7j) increase with a plateau of high values (about 50 %) persistent until 6.5 ka BP. However, the Early Holocene also corresponds to the maximum of the boreal summer insolation and the related northward migration of the intertropical convergence zone. This configuration drives the formation of Sapropel S1 (cf. Figure 6; Rohling, 1994; Rohling et al., 2004, 2015) added to the enhanced river discharge in the Eastern Mediterranean Basin, as observed eastward in the Siculo-Tunisian strait between ca. 9.5–6 ka BP (Bout-Roumazeille et al., 2013). We suggest that enhanced African monsoons (e.g. Emeis et al., 2000 ; Kallel et al., 1997 ; De Menocal et al., 2000 ; Tachikawa et al., 2015 ; Siani et al., 2013), associated with the cessation of deep and intermediate water formation (Frigola et al., 2007; Toucanne et al., 2012), may have favored organic matter and therefore heterotrophic cyst preservation, and especially that of the most sensitive taxa *Brigantedinium* spp., under anoxic bottom waters in the Mediterranean Sea. Low productive conditions in the AM, as also confirmed by significant co-occurrences of *I. aculeatum* and *S. mirabilis* (Coussin et al., 2022), resonate with the oligotrophic conditions recorded in the Gulf of Cadiz (Penaud et al., 2016) that may have propagated in the WMB through advection of nutrient-poor subtropical North Atlantic Central Waters.

5.4. Middle Holocene (8.2–4.2 ka BP)

After an increasing trend across the Early Holocene, the Mediterranean forest reaches maximal values higher than 20% during the Mid-Holocene, while the Eurosiberian taxa do not show a significant increase (Figure 7f). These latter arboreal taxa require high moisture conditions and a reduced seasonality in the precipitation regime, therefore suggesting still moderate precipitation in the southern Mediterranean Basin as also confirmed by sclerophylous and mattorral observations (Figure 7g). The best coincidence interval for high-forest percentages in the three western Mediterranean sequences is recorded between 10 and 5.5 ka BP (green colored band in Figure 8). More specifically, the Mid-Holocene can be subdivided into three main phases.

5.4.1. The “8.2 ka BP” event

The first event, centered around 8.2 ka BP, lasting for about 100 to 200 years, is characterized by a significant drop in forest distribution (Figure 7f). This is reminiscent of the so-called “8.2 ka event” (Alley et al., 1997) that led to cold climate and hydrological conditions in the Northern Hemisphere and also affected the WMB (Combourieu Nebout et al., 1998, 2002; Magny et al., 2003; Zanchetta et al., 2007; Fletcher and Sanchez-Goñi, 2008; Pross et al., 2009;

Depreux et al., 2021) by limiting the precipitation pattern (Berger and Guilaine, 2009; Morrill et al., 2013). During this arid event, anomalously low fluvial discharge may be responsible for lower concentrations of pre-Quaternary cysts, *Glomus* spores, and freshwater microalgae in the AM (Figure 5a, 7b,c). This drought interval is also obvious with low values of the ratios Ti/Ca-XRF ratio (Figure 6h) and Kaolinite/Illite (Figure 7a) thus respectively suggesting both lower river runoff and chemical alteration. The 8.2 ka BP event is also known as a cold event with lowered SSTs, as recorded by alkenone SST (Figure 6b).

5.4.2. The African Humid Period

Between 8 and 6 ka BP, evergreen oaks largely dominated the Mediterranean forest (Figure 5b, 7f), with the maxima recorded at that time, associated with the highest representation of *Pistacia* and *Olea*, and the lowest representation of coastal-steppic and semi-arid taxa (Figure 7g), suggesting decreasing summer aridity and mild winters. From 8 to 6 ka BP, this important increase in moisture is consistent with previous studies conducted in the southwestern Mediterranean lowland areas (Fletcher et al., 2013; Jaouadi et al., 2016).

In addition, high river discharges are highlighted by increasing pre-Quaternary cyst and *Glomus* spore concentrations, as well as by the first significant increases in freshwater microalgae concentrations (Figure 7b) and significant low excursions of dinocyst-based SSS estimates (salinity drops of around 1.5 psu; Figure 6d). Simultaneously, higher Kaolinite (Figure 7a) and Ti/Ca-XRF (Figure 6h) values attest to increasing chemical alteration and river runoff, in a context of warmer SSTs suggested by dinocyst-derived and alkenone reconstructions (1.5°C higher than present; Figure 6b,c). This interval of increased precipitation in the Algerian highlands is synchronously recorded by several studies in the Maghreb region (Jaouadi et al., 2016; Lebreton et al., 2019; Depreux et al., 2021) and by Mediterranean simulations (Brayshaw et al., 2011; Peyron et al., 2017). At this time, rains grew stronger and spread northward into the Sahara with enhanced summer rainfall in Africa and other parts of the tropics (e.g. de Menocal et al., 2000; McGee et al., 2013). No monsoon precipitations are recorded in the studied Western Mediterranean area (Tzedakis, 2007; Brayshaw et al., 2011), but increasing moisture attests to the strongest phase of summer rainfall (average annual precipitation of 650 mm; 270 mm higher than the present) in a context of enhanced temperature seasonality (Figure 7h).

After the oligotrophic cooler conditions of the Early Holocene, higher nutrient-enriched fluvial discharge may explain a slight increase in productivity, as suggested by increasingly heavy values of planktonic $\delta^{13}C$ and a slight increase in phototrophic cyst concentrations (Figure 6f,g).

However, the Middle Holocene also records the strongest representation of the subtropical taxon *I. aculeatum*, concomitantly with Alboran Sea and Gulf of Cadiz sequences (Penaud et al., 2011, 2016; Rouis-Zargouni et al., 2012), this taxon signing for warmer-oligotrophic sea surface conditions. We therefore suggest that the high mid-Holocene SSTs may have prolonged the seasonal length of water column stratification and thus the deepening of the thermocline. We hypothesize that the subsequent deepening of the nutricline mitigated the productive conditions, explaining the low contrast between early and Middle Holocene productivity regimes.

At ca 8 ka BP, the shift between the Early and Middle-Holocene is marked by the onset of the Western Alboran Gyre circulation (Rohling et al., 1995; Pérez-Folgado et al., 2003; Ausín et al., 2015), promoting enhanced Atlantic water inflow into the Mediterranean Basin and the onset of the AC flow through the east, consistently with the increased Ocen/Lmac ratio from Cadiz to Algeria (Figure 8f,i,l,o). Interestingly, from 8 ka BP, the easternmost Ocen/Lmac signature shows an inverse trend to that of all western Mediterranean sequences, suggesting a strong depletion of the Atlantic influence from the Middle-Holocene at the Siculo-Tunisian strait, while increasing Ocen/Lmac ratios were synchronously recorded for the cold YD from west to east in the five sediment cores (Figure 8f,i,l,o,r).

5.4.3. Mediterranean forest retreat onset

From 6 ka BP, the progressive decline in forest taxa and the increase in coastal-steppic taxa percentages, associated with decreasing fluxes of TERR-alkanes as well as decreasing concentrations of pollen, *Glomus* spores, freshwater microalgea and pre-Quaternary cysts (Figure 7b,c,d,f,g) suggest decreasing precipitation rates and runoff in the AM. Summer precipitation therefore gradually declined (Figure 7i), due to the decrease in summer solar radiation in the tropics (Berger and Loutre, 1991), and climate conditions became too dry for plants. The sharp drops in Ti/Ca-XRF (Figure 6h) and Kaolinite values (Figure 7a) also suggest dusty-desert conditions, in agreement with previous western Mediterranean aridification signals (e.g. Fletcher and Zielhofer, 2013; Depreux et al., 2021), therefore characterizing the end of the AHP (Shanahan et al., 2015). The aridity trend, that started after 6 ka BP, ranged from about 5.5 to 3 ka BP (yellow band identified between limits “d” and “e” in Figures 6 and 7), consistently with an extremely dry interval described in western Mediterranean studies at the end of the African Humid Period (Cacho et al., 2001; Combourieu-Nebout et al., 2009), and also corresponding to increasing flash floods in Tunisia and Morocco due to erodible soils in

open landscape (Zielhofer and Faust, 2008; Depreux et al., 2021). During this interval, phototrophic productivity and higher dinocyst diversity (Figure 4a) coincide with ever-increasing heavy values of planktonic $\delta^{13}C$ (Figure 6g). Productive conditions are related to decreasing percentages of *I. aculeatum* (i.e. SST cooling) and increasing percentages of *S. mirabilis* (i.e. Atlantic water influence), suggesting, as for the YD (section 5.2.a.), a stronger vigour of the AC resulting from the strengthening of the Alboran gyres. Lower *Brigantedinium* spp. values may result from a lower preservation under stronger ventilation of Mediterranean bottom waters at that time.

5.5. Late Holocene (4.2 ka BP to present)

5.5.1. The "4.2 ka BP" event

Peak values of coastal-steppic and semi-arid taxa percentages culminated between 4.3 and 3.9 ka BP, coupled with the lowest *Glomus* spore concentrations recorded in the sequence, and may correspond to a phase of megadrought in Algeria (MDA in Figure 7) that lasted for about 400 years (Figure 7g), consistent with a regional speleothem study from Ruan et al. (2016). The highest summer droughts recorded in the study area therefore appear synchronous with the well-known 4.2 ka BP event (e.g. Jalali et al., 2016; Bini et al., 2019, Kaniewski et al., 2019; Di Rita and Magri, 2019), within the 5.5–3 ka BP interval. This also coincides with the development of the plateau of the heaviest planktonic $\delta^{13}C$ values (i.e. strongest productivity from 4.2 ka BP onward) in a context where the lowest percentages of *Brigantedinium* spp. were recorded, likely due to a strengthening of deep-water circulation at 4.2 ka BP (Figure 6g,i).

5.5.2. Settling of Modern conditions

The Late Holocene is characterized by the end of the 5.5–3 ka BP most arid Holocene interval followed by the last 3 kyrs BP occurring in a context of orbitally-driven climate aridity. From the Middle to Late Holocene, Mediterranean landscapes are strongly influenced by human impacts and fire activity (Pausas and Vallejo 1999, Vannière et al., 2008; Mercuri et al., 2019). Over the last 3 kyrs BP, two phases are identifiable in this study. First, from 3 to 1.5 ka BP, strong river discharge to the AM and associated runoff are recognized through increasing Ti/Ca-XRF (Figure 6h) and Kaolinite/Illite (Figure 7a) values. Pre-Quaternary cyst (Figure 5a), *Glomus* spore and freshwater microalgae (Figure 7b,c) concentrations, even reached their highest values over this period. Stronger signals of alteration-erosion and river runoff to the

AM directly follow the 5.5–3 ka BP interval, as observed during the Early Holocene right after the YD. Only the freshwater algae remain stable with low values during the Early Holocene compared with the 3–1.5 ka BP interval. The 3 to 1.5 ka BP interval also corresponds to increasing advection of Anthropogenic Pollen Indicators (*Rumex*, *Cerealia*-type and *Plantago lanceolata*) as well as Amaranthaceae and *Artemisia* (Figure 5b), likely resulting from pastures, as previously suggested in arid climates (Jaouadi et al., 2010; Florenzano *et al*., 2012; Florenzano *et al*., 2015). Two factors may have amplified the signature of river erosion-runoff: i) the arid conditions prevailing that favored strong erodability of soils, and ii) the superimposed growing anthropic impacts opening the landscapes in adjacent watersheds (e.g. Pastoralism, culture parcels and land clearing).

The second phase, from 1.5 ka BP to the top of the sequence, presents a sharp drop in Mediterranean forest taxa percentages in parallel with the highest Kaolinite/Illite (strongest chemical alteration ; Figure 7a) and Ti/Ca-XRF values (strongest erosional-runoff processes; Figure 6h). The antagonist pattern between "*Glomus* spore - freshwater microalgae" concentrations and Kaolinite/Illite values (i.e. opposite their general covariation during the whole sequence) lead to interpret this interval as driven by anthropogenic forcing.

Regarding surface waters, the plateau of heavy planktonic $\delta^{13}C$ values, starting at 3 ka BP coincides with decreasing *Impagidinium* spp. percentages and concentrations. At this period, *Brigantedinium* spp. percentages and concentrations maintain their highest values, with concentrations of heterotrophic cysts (Figure 6f) even significantly exceeding those of autotrophic cysts for the first time of the whole study sequence. From 3 ka BP, the upwelling taxon *T. applanatum* reaches its highest percentages and concentrations (Figure 5a). We therefore argue for the development of the current hydrographic conditions (cf. Figure 1a), where productivity is sustained by both vertical mixing due to the AC in the AM (wind-driven eddies) and nutrient-enriched fluvial discharge intensified by anthropic-driven land-use. Interestingly, the threshold previously highlighted at 1.5 ka BP (limit "f" in Figure 6) corresponds to a marked drop in alkenone and dinocyst-derived SST estimates, that also corresponds to reduced dinocyst-derived SSS estimates. From 1.5 ka BP to present, this SST and SSS decrease would confirm that strong advection of continental waters, accelerated by anthropic-driven erosional processes, can be superimposed on the post-3 ka BP setup of modern sea surface conditions, participating in the present-day primary productivity in the AM.

5.6. West to East Mediterranean Basin transect

5.6.1. Regional disparities in hydrological-climatic trends along the Holocene

Pollen records from north-eastern Algeria, and more specifically marine records from the Siculo-Tunisian Strait, show a progressive Late Holocene evolution characterized by higher precipitation rates (Figure 8g, j, m, p). This may be due to the Mediterranean storm track carrying increased moisture from the Atlantic through the Gulf of Lion to the north-eastern Algeria, northern Tunisian and Sicilian areas (Desprat et al., 2013; Lionello et al., 2016). During the Late Holocene, the northward storm track, affecting less frequently the westernmost Mediterranean regions (i.e. Alboran Sea for instance characterized by increasing aridity despite lower summer temperatures), would be responsible for stronger Mediterranean storms from the Gulf of Lion to the Central Mediterranean Sea as presently observed (Lionello et al., 2006).

This dichotomy between climate trends recorded in the Alboran Sea and AM is furthermore reflected by highest alkenone SST reached between 10–8 ka BP westward (and decreasing afterwards following NGRIP temperatures; cf. ODP 976 data in Figure 8a, h). These temperature ranges are reached from 8 ka BP eastward (particularly obvious with core MD04-2801 data in Figure 8n). The increasing SST gradient from west to east is also evident whatever the interval considered over the last 14 kyrs.

5.6.2. Rapid Holocene climate changes

Rapid decline of forest at the infra-millennial timescale suggests events of enhanced continental aridity, synchronously with alkenone SST coolings at 9, 8.2, 7.3 and 6.5 ka BP (horizontal dotted lines in Figure 8). These cold, arid events have already been described in marine and continental studies from SW Iberia to the WMB (Cacho et al., 2001; Frigola et al., 2007; Jalut et al., 2000, 2009; Fletcher and Sanchez-Goñi, 2008; Combourieu-Nebout et al., 2009; Chabaud et al., 2014; Jalali et al., 2016; Azuara et al., 2020) and are associated with the North Atlantic Bond events (Bond et al., 2001; Figure 8e). Several studies suggest that changes in North Atlantic thermohaline circulation could have triggered the multi-centennial scale climate variability of the WMB (Bianchi and McCave, 1999; Bond et al., 2001; Oppo et al., 2006; Fletcher and Sanchez-Goñi, 2008; Combourieu-Nebout et al., 2009, Chabaud et al., 2014).

From the Early Holocene, the AM forest decline events are generally synchronous with lower alkenone SST and higher *O. centrocarpum* occurrences figured out by positive values of the Ocen/Lmac ratio (Figure 8n,o). This suggests enhanced inflow of Atlantic waters in the WMB and stronger moisture transport by the westerlies track directed northward and affecting to a lesser extent the westernmost part of the Mediterranean Sea. By analogy, this would correspond to recurrent positive modes of the North Atlantic Oscillation (NAO). Interestingly, these

positive “NAO-like” events are expressed in contrast in the Siculo-Tunisian strait with lower *O. centrocarpum* and higher values of *L. machaerophorum* occurrences, suggesting stronger river discharge eastward. This pattern could illustrate the west-east modeled dipole response to NAO-like changes in the SW Mediterranean Basin according to Bini et al. (2019) and Perşoiu et al. (2019).

Dryer conditions, under enhanced wind strength in northern Atlantic latitudes (i.e. Bond event under recurrent phases of positive “NAO-like” conditions), may therefore explain lower tree percentages (Fletcher et al., 2010, 2013), and reversely higher tree percentages during recurrent phases of negative “NAO-like” conditions (Figure 8). Our study reveals the rapid response of Mediterranean vegetation and hydrological dynamics and the strong influence of the North Atlantic climate through atmosphere-ocean interactions and ocean circulation at a multi-centennial time scale.

6. Conclusion

Multiproxy investigation of dinoflagellate cysts, pollen, non-pollen palynomorphs, stable isotopes, clay mineral assemblages, grain-size analyses, marine and continental biomarkers, and climate and hydrological quantitative reconstructions were conducted on the marine core MD04-2801 on the Algerian Margin (AM). This study reveals the strong influence of orbital, multi-centennial and centennial forcing on hydrological conditions and vegetation dynamics over the last 14 kyrs BP. We show that dry and cold conditions prevailed during the Younger Dryas as well as strong marine productivity. Warmer conditions of the Early to Middle Holocene allowed for Mediterranean forest expansion, while the AM became oligotrophic until 6 ka BP. At an orbital timescale, the end of the African Humid Period led to aridification of the western Mediterranean at the Middle to Late Holocene transition, with a dramatic forest retreat, particularly pronounced between 4.3 and 3.9 ka BP. This event is referred to here as the Algerian Mega Drought event, that appeared synchronously with the « 4.2 ka BP » event. Sensitivity of the western Mediterranean to Northern Atlantic climate is also evidenced at an infra-orbital timescale through several cold-dry events around 9, 8.1, 7.3 and 6.5 ka BP. The forest decline from the Alboran Sea to the AM may result from the coupling of the North Atlantic Bond events with prevailing positive modes of the North Atlantic Oscillation (NAO) with a marked west to east dipole highlighted between the northern African coast up to Algeria and Tunisia. Finally, over the last 3 kyrs BP, we have underlined the development of modern productive conditions on the AM due to both vertical mixing (haline front and wind-driven eddies of the Algerian Current) and nutrient-enriched fluvial discharge intensified by anthropic-driven land-use.

7. Acknowledgements

This work was part of a PhD thesis (V.C.) financed by the *Région Bretagne* and UBO (Univ Brest). The work was supported by the French national programme (CNRS) LEFE-EC2CO (“DATAPOL”) and by the ISblue project, Interdisciplinary graduate school for the blue planet (ANR-17-EURE-0015), co-funded by a grant from the French government under the program "Investissements d'Avenir". The work was also supported by the INSU-Mistrals Progam - PaleoMex part. We thank Yannick Miras for his help in Non Pollen Palynomorph determination and discussions on their ecological signature. Thanks also to ISEM for their contribution.

8. Data availability

MD04-2801 data discussed in the manuscript are available in the SEANOE repository: https://doi.org/10.17882/89514

9. Table captions

Table 1: MD04-2801 AMS-^{14}C dates. Grey cells represent levels averaged for the final age model. Dates in italic (with the annotation « * ») were rejected for the final age model (Figure 2).

Table 2: This table presents MD04-2801 palynological data discussed in this study and describes each pollen zone for dinocyst and pollen grains assemblages.

10. Figure captions

Figure 1: a) Map presenting studied part of the Western Mediterranean Basin (WMB) on the globe (red square on global scale map) , sea-surface temperature, as well as major sea-surface and atmospheric currents (a simplified vegetation model according to Tassin (2012). b) Map presenting the local scale map (red square on regional scale map) figure topography and hydrographic network, high-resolution bathymetric data from the Algerian Margin (Babonneau et al., 2012), morphological entities of the Kramis deep-sea fan and location of the study core and selected corresponding modern sediments (Coussin et al., in prep.).

Figure 2: Age model for core MD04-280 based on the combination of age model a (lower section (1031 to 431 cm)) and age model b (upper section (431 to 0 cm)) from rbacon package calculation (Blaauw and Christen, 2011) performed under the R interface (version 4.1.0; R Development Core Team, 2021; http://www.r-project.org/) and rejected dates. Stratigraphic data includes the corresponding section number and photography, lithology, sediments density (g/cm^3), sedimentation rates (cm/kyrs) and Vp (m/s) values. Core disturbance by potential piston effect is represented as a red square on the age model.

Figure 3: Sedimentological data of core MD04-2801 in function of depth, core section and lithology. a) XRF Ca/Al ratio, b) XRF Ti/Al ratio, c) Magnetic susceptibility (SI). d) Low

resolution total sediment D50 (µm) in blue reported in faded blue on high-resolution total grain-size (d) and $CaCO_3$-free D50 in red. e) Planktonic (*G. bulloides*; in green) and endobenthic (*G. affinis*; in yellow) δ13C (‰ VPDB), higher planktonic signal suggests stronger primary productivity while lower endobenthic signal suggests stronger organic matter remineralisation. f) Planktonic (*G. bulloides*; in red) and endobenthic (*G. affinis*; in violet) δ18O (‰). g) Clay mineral fractions of Interstratified Illite-Smectite (In), Chlorite (Ch), Kaolinite (Kao) and Illite (Il).

Figure 4: MD04-2801 a) marine and b) continental palynological, biomarkers and MAT reconstruction data against depth (cm). a) Dinocyst diversity indexes are shown in red and blue, in parallel with percentages of the major species *Brigantedinium* spp. (red dotted line). Concentration of the total sum of dinocysts is shown in black, total sum of dinocysts without *Brigantedinium* spp. is represented in blue and *Brigantedinium* spp. concentration is represented in red. Concentration of C_{37} alkenones is represented in light blue (sum of C_{37}, ng/g). Total dinocyst (blue) and pollen with *Pinus* (orange) concentrations are represented in the logarithmic scale. b) Pollen diversity indexes are in green, in parallel with percentages of total trees (green) and total trees with *Pinus* (orange). Concentration of the total sum of pollen is shown in orange, total sum of dinocysts without *Pinus* in green. Concentration of TERR-alkanes in brown (sum of TERR-alkanes, ng/g) and Average Chain Length (ACL) in yellow with average sequence value as a dotted line.

Figure 5: a) Dinocyst diagram (percentages of selected taxa exceeding at least once 1% in all studied samples) of the MD04-2801 core, with related ecological groups (cf. Coussin et al., 2022). Dinocyst zones are based on a CONISS statistical analysis on the Tilia program. b) Pollen diagram (percentages of selected taxa when exceeding at least once 1% in all studied samples, *Pinus* excluded from the main pollen sum) for the MD04-2801 core, with related ecological groups. For both a) and b), continental non-pollen palynomorphs (NPPs) and pre-quaternary cysts are highlighted in concentrations (number of palynomorphs per cm^3 of sediment). (For interpretation of the references to color in this figure legend, the reader is referred to the web version of this article.)

Figure 6: Oceanic proxies from the MD04-2801 core plotted in age (Cal years BP) with related pollen zones, sedimentological, stratigraphical limits and remarquable periods (S1 = Sapropel 1). Modern values from KMDJ-23 core are plotted as colored stars in the left band of the figure

(1 - 0 ka). a) Planktonic δ18O (‰), b) Alkenone derived annual Sea Surface Temperatures (SST, shaded from low temperatures in blue to high temperatures in red, °C), c) Cold water dinocyst taxa percentages (*N. labyrinthus, B. tepikiense* and *S. lazus*, cf. Figure 5) in reversed logarithmic scale, d) Dinocysts-derived Winter (blue) and Summer (red) SST (°C) with shaded reconstructed minima and maxima and alkenone annual SST as a dotted blue line. e) Dinocyst-derived Winter (blue) and Summer (red) Sea Surface Salinity (SSS, psu) with shaded reconstructed minima and maxima, f) Heterotrophic (orange) and Phototrophic (green) dinocyst concentration in logarithmic scale, g) Planktonic (*G. bulloides*; in green) and endobenthic (*G. affinis*; in orange) δ13C (‰ VPDB), h) XRF Ti/Ca ratio, i) *Brigantedinium* spp. percentages (%), j) *Brigantedinium* spp. concentration (red line), k) *Impagidinium* spp. percentages (%), l) *Impagidinium* spp. concentration (brown).

Figure 7: Continental proxies from the MD04-2801 core plotted in age (Cal years BP) with related pollen zones, sedimentological, stratigraphical limits and exceptional periods (S1 = Sapropel 1, Megadrought Algeria = MDA). Modern values from KMDJ-23 core are plotted as colored stars in the left band of the figure (1 - 0 ka). a) Kaolinite/Illite percentages of the clayey phase ratio with higher Illite values in green and higher values in Kaolinite in red, b) freshwater algae concentration (green) , c) Glomus (HDV-207) concentration (grey), d) superior plant leaf wax produced TERR-alkane (shaded green silhouette) and major represented n-C29 + n-C-31 (green dotted line) fluxes ($ng.g^{-1}.yrs^{-1}$), e) Siliciclastic coarse grain inputs schematized by magnetic susceptibility (SI), f) Mediterranean and Eurosiberian forest (cf. Figure 5) percentages, g) Coastal-steppic and Semi-arid vegetation (cf. Figure 5) percentages, h) Temperature seasonality index calculated with pollen-derived Mean Temperature of the Warmest Month (MTWA) and Mean Temperature of the Coldest Month (MTCO) as (MTWA-MTCO). i) Pollen-derived annual precipitation reconstructions (mm, blue line), j) Altitudinal forest (cf. Figure 5), k) Human impact taxa (cf. Figure 5) percentages.

Figure 8: West to east transect of sequences from the Gulf of Cadiz (MD99-2339), Alboran sea (ODP site 976 and MD95-2043), Algerian Margin (MD04-2801, this study) and Sicilian strait (MD04-2797) with paleoenvironmental data plotted in age (Cal years BP) both on their published chronology and their geographical situation on the map versus Orbital parameters (a) NGRIP δ18O (‰, Vinther et al., 2006) in black, b) 65°N insolation in yellow (W/m^2) from Berger and Loutre (1991), c) Precession in blue and e) Hematite-stained quartz % in red (Bond

et al., 2001). For both represented cores, (d,h,k,n,q) Alkenone SST are represented (black line, °C), (f,I,l,o,r) OCEN/LMAC log ratio representing oceanic dinocyst taxa *O. centrocarpum* versus estuarine dinocyst taxa *L. machaerophorum* log ratio (blue shaded silhouette, higher ratios represent lower river discharge conditions), (g,j,m,p) Summed Mediterranean and Eurosiberian forest (%) with total sum as a green silhouette and eurosiberian proportion as a brown dotted line. Spotted forest retreat events are shown as dotted horizontal lines with corresponding ages. The regional map figures all cited sequences, geographical coordinates and zonal correlations with negative NAO conditions (modified after Perşoiu et al. (2019) in Bini et al. (2019). Green zones show positive correlations with NAO- conditions indicating stronger precipitations than average during NAO- and orange zones figure negative correlations with NAO- conditions indicating lower precipitations than average during NAO-.

11. References

Allen, J.R.M., Watts, W.A., McGee, E., Huntley, B., 2002. Holocene environmental variability—the record from Lago Grande di Monticchio, Italy. Quaternary International 88, 69–80.

Alley, R.B., Mayewski, P.A., Sowers, T., Stuiver, M., Taylor, K.C., Clark, P.U., 1997. Holocene climatic instability: A prominent, widespread event 8200 yr ago. Geology 25, 483–486.

Arnone, R.A., La Violette, P.E., 1986. Satellite definition of the bio-optical and thermal variation of coastal eddies associated with the African Current. Journal of Geophysical Research: Oceans 91, 2351–2364.

Arnone, R.A., Wiesenburg, D.A., Saunders, K.D., 1990. The origin and characteristics of the Algerian Current. Journal of Geophysical Research: Oceans 95, 1587–1598.

Ausín, B., Flores, J.A., Sierro, F.J., Cacho, I., Hernández-Almeida, I., Martrat, B., Grimalt, J.O., 2015. Atmospheric patterns driving Holocene productivity in the Alboran Sea (Western Mediterranean): a multiproxy approach. The Holocene 25, 583–595.

Azuara, J., Sabatier, P., Lebreton, V., Jalali, B., Sicre, M.-A., Dezileau, L., Bassetti, M.-A., Frigola, J., Combourieu-Nebout, N., 2020. Mid- to Late-Holocene Mediterranean climate variability: Contribution of multi-proxy and multi-sequence comparison using wavelet spectral analysis in the northwestern Mediterranean basin. Earth-Science Reviews 208, 103232.

Babonneau, N., Cattaneo, A., Savoye, B., Barjavel, G., Déverchère, J., Yelles, K., 2012. The Kramis fan offshore western Algeria: the role of sediment waves in turbiditic levee growth. SEPM Special Publication 99, 293–308.

Bahr, A., Jiménez- Espejo, F.J., Kolasinac, N., Grunert, P., Hernández- Molina, F.J., Röhl, U.,

Voelker, A.H., Escutia, C., Stow, D.A., Hodell, D., 2014. Deciphering bottom current velocity and paleoclimate signals from contourite deposits in the G ulf of C ádiz during the last 140 kyr: An inorganic geochemical approach. Geochemistry, Geophysics, Geosystems 15, 3145–3160.

Bahr, A., Kaboth, S., Jiménez-Espejo, F.J., Sierro, F.J., Voelker, A.H., Lourens, L., Röhl, U., Reichart, G.-J., Escutia, C., Hernandez-Molina, F.J., 2015. Persistent monsoonal forcing of Mediterranean Outflow Water dynamics during the late Pleistocene. Geology 43, 951–954.

Bakun, A., Agostini, V.N., 2001. Seasonal patterns of wind-induced upwelling/downwelling in the Mediterranean Sea. scimar 65, 243–257.

Barbéro, M., Quézel, P., Rivas-Martínez, S., 1981. Contribution à l'étude des groupements forestiers et préforestiers du Maroc. Phytocoenologia 311–412.

Bárcena, M.A., Cacho, I., Abrantes, F., Sierro, F.J., Grimalt, J.O., Flores, J.A., 2001. Paleoproductivity variations related to climatic conditions in the Alboran Sea (western Mediterranean) during the last glacial–interglacial transition: the diatom record. Palaeogeography, Palaeoclimatology, Palaeoecology 167, 337–357.

Bar-Matthews, M., Ayalon, A., Gilmour, M., Matthews, A., Hawkesworth, C.J., 2003. Sea–land oxygen isotopic relationships from planktonic foraminifera and speleothems in the Eastern Mediterranean region and their implication for paleorainfall during interglacial intervals. Geochimica et Cosmochimica Acta 67, 3181–3199.

Bar-Matthews, M., Ayalon, A., Kaufman, A., 2000. Timing and hydrological conditions of Sapropel events in the Eastern Mediterranean, as evident from speleothems, Soreq cave, Israel. Chemical Geology 169, 145–156.

Beaudouin, C., Suc, J.-P., Escarguel, G., Arnaud, M., Charmasson, S., 2007. The significance of pollen signal in present-day marine terrigenous sediments: The example of the Gulf of Lions (western Mediterranean Sea). Geobios 40, 159–172.

Belkebir, L., Labdi, A., Mansour, B., Bessedik, M., Saint-Martin, J.-P., 2008. Biostratigraphie et lithologie des séries serravallo-tortoniennes du massif du Dahra et du bassin du Chélif (Algérie). Implications sur la position de la limite serravallo-tortonienne. Geodiversitas 30, 9–19.

Ben Tiba, B., Reille, M., 1982. Recherches pollenanalytiques dans les montagnes de Kroumirie (Tunisie septentrionale): premiers résultats. Ecologia mediterranea 8, 75–86.

Berger, A., Loutre, M.-F., 1991. Insolation values for the climate of the last 10 million years. Quaternary Science Reviews 10, 297–317.

Berger, J.-F., Guilaine, J., 2009. The 8200 cal BP abrupt environmental change and the Neolithic transition: A Mediterranean perspective. Quaternary international 200, 31–49.

Béthoux, J.P., 1984. Paléo-hydrologie de la Méditerranée au cours des derniers 20 000 ans. Oceanologica acta 7, 43–48.

Bethoux, J.P., 1979. Budgets of the Mediterranean Sea-Their dependance on the local climate and on the characteristics of the Atlantic waters. Oceanologica acta 2, 157–163.

Bethoux, J.P., Gentili, B., 1994. The Mediterranean Sea, a Test Area for Marine and Climatic Interactions, in: Malanotte-Rizzoli, P., Robinson, A.R. (Eds.), Ocean Processes in Climate Dynamics: Global and Mediterranean Examples, NATO ASI Series. Springer Netherlands, Dordrecht, pp. 239–254.

Bianchi, G.G., McCave, I.N., 1999. Holocene periodicity in North Atlantic climate and deep-ocean flow south of Iceland. Nature 397, 515–517.

Biebow, N., 1996. Dinoflagellatenzysten als Indikatoren der spät-und postglazialen Entwicklung des Auftriebsgeschehens vor Peru (PhD Thesis). GEOMAR Forschungszentrum für marine Geowissenschaften der Christian ….

Bini, M., Zanchetta, G., Perşoiu, A., Cartier, R., Català, A., Cacho, I., Dean, J.R., Di Rita, F., Drysdale, R.N., Finnè, M., 2019. The 4.2 ka BP Event in the Mediterranean region: an overview. Climate of the Past 15, 555–577.

Blaauw, M., Christen, J.A., 2011. Flexible paleoclimate age-depth models using an autoregressive gamma process. Bayesian analysis 6, 457–474.

Bliedtner, M., Schäfer, I.K., Zech, R., von Suchodoletz, H., 2018. Leaf wax n-alkanes in modern plants and topsoils from eastern Georgia (Caucasus)–implications for reconstructing regional paleovegetation. Biogeosciences 15, 3927–3936.

Bogus, K., Mertens, K.N., Lauwaert, J., Harding, I.C., Vrielinck, H., Zonneveld, K.A.F., Versteegh, G.J.M., 2014. Differences in the chemical composition of organic-walled dinoflagellate resting cysts from phototrophic and heterotrophic dinoflagellates. Journal of Phycology 50, 254–266.

Bond, G., Kromer, B., Beer, J., Muscheler, R., Evans, M.N., Showers, W., Hoffmann, S., Lotti-Bond, R., Hajdas, I., Bonani, G., 2001. Persistent solar influence on North Atlantic climate during the Holocene. science 294, 2130–2136.

Bond, G., Showers, W., Cheseby, M., Lotti, R., Almasi, P., deMenocal, P., Priore, P., Cullen, H., Hajdas, I., Bonani, G., 1997. A Pervasive Millennial-Scale Cycle in North Atlantic Holocene and Glacial Climates. Science 278, 1257–1266.

Bordon, A., Peyron, O., Lézine, A.-M., Brewer, S., Fouache, E., 2009. Pollen-inferred late-glacial and Holocene climate in southern Balkans (Lake Maliq). Quaternary International 200, 19–30.

Bouimetarhan, I., Marret, F., Dupont, L., Zonneveld, K., 2009. Dinoflagellate cyst distribution in marine surface sediments off West Africa (17–6 N) in relation to sea-surface conditions, freshwater input and seasonal coastal upwelling. Marine Micropaleontology 71, 113–130.

Bout-Roumazeilles, V., Combourieu Nebout, N., Peyron, O., Cortijo, E., Landais, A., Masson-

Delmotte, V., 2007. Connection between South Mediterranean climate and North African atmospheric circulation during the last 50,000yrBP North Atlantic cold events. Quaternary Science Reviews 26, 3197–3215.

Bout-Roumazeilles, V., Combourieu-Nebout, N., Desprat, S., Siani, G., Turon, J.-L., Essallami, L., 2013. Tracking atmospheric and riverine terrigenous supplies variability during the last glacial and the Holocene in central Mediterranean. Climate of the Past 9, 1065–1087.

Bout-Roumazeilles, V., Cortijo, E., Labeyrie, L., Debrabant, P., 1999. Clay mineral evidence of nepheloid layer contributions to the Heinrich layers in the northwest Atlantic. Palaeogeography, Palaeoclimatology, Palaeoecology 146, 211–228.

Brayshaw, D.J., Hoskins, B., Black, E., 2010. Some physical drivers of changes in the winter storm tracks over the North Atlantic and Mediterranean during the Holocene. Philosophical Transactions of the Royal Society A: Mathematical, Physical and Engineering Sciences 368, 5185–5223.

Brayshaw, D.J., Rambeau, C.M., Smith, S.J., 2011. Changes in Mediterranean climate during the Holocene: Insights from global and regional climate modelling. The Holocene 21, 15–31.

Brun, A., 1989. Microflores et paléovégétations en Afrique du Nord depuis 30 000 ans. Bulletin de la Société géologique de France 25–33.

Bryden, H.L., Kinder, T.H., 1991. Steady two-layer exchange through the Strait of Gibraltar. Deep Sea Research Part A. Oceanographic Research Papers 38, S445–S463.

Cacho, I., Grimalt, J.O., Canals, M., Sbaffi, L., Shackleton, N.J., Schönfeld, J., Zahn, R., 2001. Variability of the western Mediterranean Sea surface temperature during the last 25,000 years and its connection with the Northern Hemisphere climatic changes. Paleoceanography 16, 40–52.

Cacho, I., Grimalt, J.O., Pelejero, C., Canals, M., Sierro, F.J., Flores, J.A., Shackleton, N., 1999. Dansgaard- Oeschger and Heinrich event imprints in Alboran Sea paleotemperatures. Paleoceanography 14, 698–705.

Castañeda, I.S., Werne, J.P., Johnson, T.C., Filley, T.R., 2009. Late Quaternary vegetation history of southeast Africa: the molecular isotopic record from Lake Malawi. Palaeogeography, Palaeoclimatology, Palaeoecology 275, 100–112.

Chabaud, L., Sánchez Goñi, M.F., Desprat, S., Rossignol, L., 2014. Land–sea climatic variability in the eastern North Atlantic subtropical region over the last 14,200 years: atmospheric and oceanic processes at different timescales. The Holocene 24, 787–797.

Cheddadi, R., Fady, B., François, L., Hajar, L., Suc, J.-P., Huang, K., Demarteau, M., Vendramin, G.G., Ortu, E., 2009. Putative glacial refugia of Cedrus atlantica deduced from Quaternary pollen records and modern genetic diversity. Journal of Biogeography 36, 1361–1371.

Cheddadi, R., Lamb, H.F., Guiot, J., van der Kaars, S., 1998. Holocene climatic change in Morocco: a quantitative reconstruction from pollen data. Climate dynamics 14, 883–890.

Combourieu Nebout, N.C., Londeix, L., Baudin, F., Turon, J.-L., von Grafenstein, R., Zahn, R., 1999. Quaternary marine and continental paleoenvironmentsin the Western Mediterranean (Site 976, Alboran Sea): palynological evidence.

Combourieu Nebout, N.C., Peyron, O., Dormoy, I., Desprat, S., Beaudouin, C., Kotthoff, U., Marret, F., 2009. Rapid climatic variability in the west Mediterranean during the last 25 000 years from high resolution pollen data. Clim. Past 19.

Combourieu Nebout, N.C., Turon, J.L., Zahn, R., Capotondi, L., Londeix, L., Pahnke, K., 2002. Enhanced aridity and atmospheric high-pressure stability over the western Mediterranean during the North Atlantic cold events of the past 50 ky. Geology 30, 863–866.

Combourieu-Nebout, N., Paterne, M., Turon, J.-L., Siani, G., 1998. A high-resolution record of the last deglaciation in the central Mediterranean Sea: Palaeovegetation and palaeohydrological evolution. Quaternary Science Reviews 17, 303–317.

Coussin V., Penaud A., Combourieu-Nebout N., Peyron O., Schmidt S., Zaragosi S., De Vernal A., Babonneau N., 2022. Distribution of modern dinocyst and pollen grains in the Western Mediterranean Sea (Algerian margin and Gulf of Lion). Marine Micropaleontology 175, 102157.

Cugny, C., Mazier, F., Galop, D., 2010. Modern and fossil non-pollen palynomorphs from the Basque mountains (western Pyrenees, France): the use of coprophilous fungi to reconstruct pastoral activity. Veget Hist Archaeobot 19, 391–408.

Damsté, J.S.S., Verschuren, D., Ossebaar, J., Blokker, J., van Houten, R., van der Meer, M.T., Plessen, B., Schouten, S., 2011. A 25,000-year record of climate-induced changes in lowland vegetation of eastern equatorial Africa revealed by the stable carbon-isotopic composition of fossil plant leaf waxes. Earth and Planetary Science Letters 302, 236–246.

De Menocal, P.B., Ortiz, J., Guilderson, T., Adkins, J., Sarnthein, M., Baker, L., Yarusinsky, M., 2000. Abrupt onset and termination of the African Humid Period:: rapid climate responses to gradual insolation forcing. Quaternary science reviews 19, 347–361.

De Vernal, A., Eynaud, F., Henry, M., Hillaire-Marcel, C., Londeix, L., Mangin, S., Matthießen, J., Marret, F., Radi, T., Rochon, A., 2005. Reconstruction of sea-surface conditions at middle to high latitudes of the Northern Hemisphere during the Last Glacial Maximum (LGM) based on dinoflagellate cyst assemblages. Quaternary Science Reviews 24, 897–924.

De Vernal, A., Henry, M., Bilodeau, G., 1999. Techniques de préparation et d'analyse en micropaléontologie. Les cahiers du GEOTOP 3, 41.

De Vernal, A., Radi, T., Zaragosi, S., Van Nieuwenhove, N., Rochon, A., Allan, E., De

Schepper, S., Eynaud, F., Head, M.J., Limoges, A., Londeix, L., Marret, F., Matthiessen, J., Penaud, A., Pospelova, V., Price, A., Richerol, T., 2020. Distribution of common modern dinoflagellate cyst taxa in surface sediments of the Northern Hemisphere in relation to environmental parameters: The new n=1968 database. Marine Micropaleontology, Taxonomy and distribution of modern organic-walled dinoflagellate cysts in surface sediments from the Northern Hemisphere: an update of Rochon et al., 1999 159, 101796.

Depreux, B., Lefèvre, D., Berger, J.-F., Segaoui, F., Boudad, L., El Harradji, A., Degeai, J.-P., Limondin-Lozouet, N., 2021. Alluvial records of the African Humid Period from the NW African highlands (Moulouya basin, NE Morocco). Quaternary Science Reviews 255, 106807.

Desprat, S., Combourieu-Nebout, N., Essallami, L., Sicre, M.-A., Dormoy, I., Peyron, O., Siani, G., Bout Roumazeilles, V., Turon, J.-L., 2013. Deglacial and Holocene vegetation and climatic changes in the southern Central Mediterranean from a direct land–sea correlation. Climate of the Past 9, 767–787.

Di Rita, F., Lirer, F., Bonomo, S., Cascella, A., Ferraro, L., Florindo, F., Insinga, D.D., Lurcock, P.C., Margaritelli, G., Petrosino, P., 2018. Late Holocene forest dynamics in the Gulf of Gaeta (central Mediterranean) in relation to NAO variability and human impact. Quaternary Science Reviews 179, 137–152.

Di Rita, F., Magri, D., 2019. The 4.2 ka event in the vegetation record of the central Mediterranean. Climate of the Past 15, 237–251.

Dormoy, I., Peyron, O., Combourieu Nebout, N., Goring, S., Kotthoff, U., Magny, M., Pross, J., 2009. Terrestrial climate variability and seasonality changes in the Mediterranean region between 15 000 and 4000 years BP deduced from marine pollen records. Climate of the Past 5, 615–632.

Dugerdil, L., Joannin, S., Peyron, O., Jouffroy-Bapicot, I., Vannière, B., Boldgiv, B., Unkelbach, J., Behling, H., Ménot, G., 2021. Climate reconstructions based on GDGT and pollen surface datasets from Mongolia and Baikal area: calibrations and applicability to extremely cold–dry environments over the Late Holocene. Climate of the Past 17, 1199–1226.

Emeis, K.-C., Struck, U., Schulz, H.-M., Rosenberg, R., Bernasconi, S., Erlenkeuser, H., Sakamoto, T., Martinez-Ruiz, F., 2000. Temperature and salinity variations of Mediterranean Sea surface waters over the last 16,000 years from records of planktonic stable oxygen isotopes and alkenone unsaturation ratios. Palaeogeography, Palaeoclimatology, Palaeoecology 158, 259–280.

Fatela, F., Taborda, R., 2002. Confidence limits of species proportions in microfossil assemblages. Marine Micropaleontology 45, 169–174.

Fensome, R.A., 1993. A classification of living and fossil dinoflagellates. Micropaleontology, special publication 7, 1–351.

Fink, H.G., Wienberg, C., De Pol-Holz, R., Hebbeln, D., 2015. Spatio-temporal distribution

patterns of Mediterranean cold-water corals (Lophelia pertusa and Madrepora oculata) during the past 14,000 years. Deep Sea Research Part I: Oceanographic Research Papers 103, 37–48.

Fletcher, W.J., Debret, M., Goñi, M.F.S., 2013. Mid-Holocene emergence of a low-frequency millennial oscillation in western Mediterranean climate: Implications for past dynamics of the North Atlantic atmospheric westerlies. The Holocene 23, 153–166.

Fletcher, W.J., Sanchez Goñi, M., 2008. Orbital-and sub-orbital-scale climate impacts on vegetation of the western Mediterranean basin over the last 48,000 yr. Quaternary Research 70, 451–464.

Fletcher, W.J., Sanchez Goñi, M.F., Peyron, O., Dormoy, I., 2010. Abrupt climate changes of the last deglaciation detected in a Western Mediterranean forest record. Climate of the Past 6, 245–264.

Florenzano, A., Marignani, M., Rosati, L., Fascetti, S., Mercuri, A.M., 2015. Are Cichorieae an indicator of open habitats and pastoralism in current and past vegetation studies? Plant Biosystems - An International Journal Dealing with all Aspects of Plant Biology 149, 154–165.

Florenzano, A., Torri, P., Rattighieri, E., N'Siala, I.M., Mercuri, A.M., 2012. Cichorioideae-Cichorieae as pastureland indicator in pollen spectra from southern Italy 12.

Frigola, J., Moreno, A., Cacho, I., Canals, M., Sierro, F.J., Flores, J.A., Grimalt, J.O., Hodell, D.A., Curtis, J.H., 2007. Holocene climate variability in the western Mediterranean region from a deepwater sediment record. Paleoceanography 22.

Gautier, F., LUBES-NIEL, H., Sabatier, R., Masson, J.M., Paturel, J.-E., Servat, E., 1998. Variabilité du régime pluviométrique de l'Afrique de l'Ouest non sahélienne entre 1950 et 1989. Hydrological sciences journal 43, 921–935.

Gilman, C., Garrett, C., 1994. Heat flux parameterizations for the Mediterranean Sea: The role of atmospheric aerosols and constraints from the water budget. Journal of Geophysical Research: Oceans 99, 5119–5134.

Grimm, E., 1987. CONISS: a FORTRAN 77 program for stratigraphically constrained cluster analysis by the method of incremental sum of squares. Computers & Geosciences 13, 13–35.

Grimm, E.C., 1990. TILIA 2.0, Software. Illinois State Museum, Springfield.

Guiot, J., 1990. Methodology of the last climatic cycle reconstruction in France from pollen data. Palaeogeography, Palaeoclimatology, Palaeoecology 80, 49–69.

Guiot, J., de Vernal, A., 2007. Chapter thirteen transfer functions: Methods for quantitative paleoceanography based on microfossils. Developments in marine geology 1, 523–563.

Guizien, K., Charles, F., Lantoine, F., Naudin, J.-J., 2007. Nearshore dynamics of nutrients and chlorophyll during Mediterranean-type flash-floods. Aquat. Living Resour. 20, 3–14.

Hammer, O., Harper, D., Ryan, P., 2001. PAST: Paleontological Statistics Software Package for Education and Data Analysis. Palaeontologia Electronica, Palaeontologia Electronica 4, 1–9.

Harnickell, E., Mueller-Dombois, D., 1975. Climate-diagram maps of the individual continents and the ecological climatic regions of the earth. Springer-Verlag.

Havinga, A.J., 1971. An experimental investigation into the decay of pollen and spores in various soil types, in: Sporopollenin. Elsevier, pp. 446–479.

Havinga, A.J., 1967. Palynology and pollen preservation. Review of Palaeobotany and Palynology 2, 81–98.

Hernández-Molina, F.J., Stow, D.A., Alvarez-Zarikian, C.A., Acton, G., Bahr, A., Balestra, B., Ducassou, E., Flood, R., Flores, J.-A., Furota, S., 2014. Onset of Mediterranean outflow into the North Atlantic. Science 344, 1244–1250.

Heusser, L.E., Balsam, W.L., 1985. Pollen sedimentation in the Northwest Atlantic: Effects of the Western Boundary Undercurrent. Marine Geology 69, 149–153.

Howell, M.W., Thunell, R.C., 1992. Organic carbon accumulation in Bannock Basin: evaluating the role of productivity in the formation of eastern Mediterranean sapropels. Marine Geology 103, 461–471.

Jalali, B., Sicre, M.-A., Bassetti, M.-A., Kallel, N., 2016. Holocene climate variability in the North-Western Mediterranean Sea (Gulf of Lions). Clim. Past 12, 91–101.

Jalali, B., Sicre, M.-A., Kallel, N., Azuara, J., Combourieu-Nebout, N., Bassetti, M.-A., Klein, V., 2017. High-resolution Holocene climate and hydrological variability from two major Mediterranean deltas (Nile and Rhone). The holocene 27, 1158–1168.

Jalut, G., Dedoubat, J.J., Fontugne, M., Otto, T., 2009. Holocene circum-Mediterranean vegetation changes: climate forcing and human impact. Quaternary international 200, 4–18.

Jaouadi, S., Lebreton, V., Bout-Roumazeilles, V., Siani, G., Lakhdar, R., Boussoffara, R., Dezileau, L., Kallel, N., Mannai-Tayech, B., Combourieu-Nebout, N., 2016. Environmental changes, climate and anthropogenic impact in south-east Tunisia during the last 8 kyr. Climate of the Past 12, 1339–1359.

Jaouadi, S., Lebreton, V., Mulazzani, S., Boussofara, R., Mannai-Tayech, B., 2010. Analyses polliniques en contexte anthropisé: le cas du site holocène SHM-1 (Hergla, Tunisie centrale). Sezione di Museologia Scientifica e Naturalistica 6, 25–32.

Jimenez- Espejo, F.J., Martinez- Ruiz, F., Rogerson, M., González- Donoso, J.M., Romero, O.E., Linares, D., Sakamoto, T., Gallego- Torres, D., Rueda Ruiz, J.L., Ortega- Huertas, M., 2008. Detrital input, productivity fluctuations, and water mass circulation in the westernmost Mediterranean Sea since the Last Glacial Maximum. Geochemistry, Geophysics, Geosystems 9.

Kallel, N., Paterne, M., Duplessy, J.C., Vergnaudgrazzini, C., Pujol, C., Labeyrie, L., Arnold, M., Fontugne, M., Pierre, C., 1997. Enhanced rainfall in the Mediterranean region during the last sapropel event. Oceanolica Acta 20, 697–712.

Kaniewski, D., Marriner, N., Bretschneider, J., Jans, G., Morhange, C., Cheddadi, R., Otto, T., Luce, F., Van Campo, E., 2019. 300-year drought frames Late Bronze Age to Early Iron Age transition in the Near East: new palaeoecological data from Cyprus and Syria. Regional Environmental Change 19, 2287–2297.

Kodrans-Nsiah, M., de Lange, G.J., Zonneveld, K.A., 2008. A natural exposure experiment on short-term species-selective aerobic degradation of dinoflagellate cysts. Review of Palaeobotany and Palynology 152, 32–39.

Kotthoff, U., Müller, U.C., Pross, J., Schmiedl, G., Lawson, I.T., van de Schootbrugge, B., Schulz, H., 2008a. Lateglacial and Holocene vegetation dynamics in the Aegean region: an integrated view based on pollen data from marine and terrestrial archives. The Holocene 18, 1019–1032.

Kotthoff, U., Pross, J., Müller, U.C., Peyron, O., Schmiedl, G., Schulz, H., Bordon, A., 2008b. Climate dynamics in the borderlands of the Aegean Sea during formation of sapropel S1 deduced from a marine pollen record. Quaternary Science Reviews 27, 832–845.

Lamb, H.F., Eicher, U., Switsur, V.R., 1989. An 18,000-year record of vegetation, lake-level and climatic change from Tigalmamine, Middle Atlas, Morocco. Journal of biogeography 65–74.

Lebreton, V., Jaouadi, S., Bruneau, M., Karbouch, M., Boujelben, A., Montaldi, M., Berger, J.-F., 2019. History of semi-arid and arid environments in the Eastern Maghreb during the Middle Holocene: first results of the pollen analysis from Sebkha Kelbia (Central Tunisia), in: The Mediterranean Palynological Societies Symposium 2019. Abstract Book. Université de Bordeaux, p. 98.

Lebreton, V., Messager, E., Marquer, L., Renault-Miskovsky, J., 2010. A neotaphonomic experiment in pollen oxidation and its implications for archaeopalynology. Review of Palaeobotany and Palynology 162, 29–38.

Lewis, J., Dodge, J., Powell, A., 1990. Quaternary dinoflagellate cysts from the upwelling system offshore Peru, Hole 686b, odp leg 1121, in: Proceedings of the Ocean Drilling Program, Scientific Results. pp. 323–328.

Lionello, P., Malanotte-Rizzoli, P., Boscolo, R., Alpert, P., Artale, V., Li, L., Luterbacher, J., May, W., Trigo, R., Tsimplis, M., 2006. The Mediterranean climate: an overview of the main characteristics and issues. Elsevier.

Lionello, P., Trigo, I.F., Gil, V., Liberato, M.L.R., Nissen, K.M., Pinto, J.G., Raible, C.C., Reale, M., Tanzarella, A., Trigo, R.M., Ulbrich, S., Ulbrich, U., 2016. Objective climatology of cyclones in the Mediterranean region: a consensus view among methods with different system identification and tracking criteria. Tellus A: Dynamic Meteorology and Oceanography 68, 29391. https://doi.org/10.3402/tellusa.v68.29391

Lohrenz, S.E., Wiesenburg, D.A., DePalma, I.P., Johnson, K.S., Gustafson, D.E., 1988. Interrelationships among primary production, chlorophyll, and environmental conditions in frontal regions of the western Mediterranean Sea. Deep Sea Research Part A. Oceanographic Research Papers 35, 793–810.

Magny, M., Bégeot, C., Guiot, J., Peyron, O., 2003. Contrasting patterns of hydrological changes in Europe in response to Holocene climate cooling phases. quaternary science reviews 22, 1589–1596.

Marret, F., 1994. Distribution of dinoflagellate cysts in recent marine sediments from the east Equatorial Atlantic (Gulf of Guinea). Review of Palaeobotany and Palynology 84, 1–22.

Marret, F., Turon, J.-L., 1994. Paleohydrology and paleoclimatology off Northwest Africa during the last glacial-interglacial transition and the Holocene: Palynological evidences. Marine Geology 118, 107–117.

Mayewski, P.A., Rohling, E.E., Stager, J.C., Karlén, W., Maasch, K.A., Meeker, L.D., Meyerson, E.A., Gasse, F., Kreveld, S. van, Holmgren, K., Lee-Thorp, J., Rosqvist, G., Rack, F., Staubwasser, M., Schneider, R.R., Steig, E.J., 2004. Holocene climate variability. Quaternary Research 62, 243–255. https://doi.org/10.1016/j.yqres.2004.07.001

McCulloch, M., Taviani, M., Montagna, P., Correa, M.L., Remia, A., Mortimer, G., 2010. Proliferation and demise of deep-sea corals in the Mediterranean during the Younger Dryas. Earth and Planetary Science Letters 298, 143–152.

McGee, D., deMenocal, P.B., Winckler, G., Stuut, J.-B.W., Bradtmiller, L.I., 2013. The magnitude, timing and abruptness of changes in North African dust deposition over the last 20,000 yr. Earth and Planetary Science Letters 371, 163–176.

Meghraoui, M., Morel, J.-L., Andrieux, J., Dahmani, M., 1996. Tectonique plio-quaternaire de la chaine tello-rifaine et de la mer d'Alboran; une zone complexe de convergence continent-continent. Bulletin de la Société géologique de France 167, 141–157.

Mercone, D., Thomson, J., Croudace, I.W., Siani, G., Paterne, M., Troelstra, S., 2000. Duration of S1, the most recent sapropel in the eastern Mediterranean Sea, as indicated by accelerator mass spectrometry radiocarbon and geochemical evidence. Paleoceanography 15, 336–347.

Mercuri, A.M., Florenzano, A., Burjachs, F., Giardini, M., Kouli, K., Masi, A., Picornell-Gelabert, L., Revelles, J., Sadori, L., Servera-Vives, G., 2019. From influence to impact: The multifunctional land use in Mediterranean prehistory emerging from palynology of archaeological sites (8.0-2.8 ka BP). The Holocene 29, 830–846.

Mertens, K.N., Verhoeven, K., Verleye, T., Louwye, S., Amorim, A., Ribeiro, S., Deaf, A.S., Harding, I.C., De Schepper, S., González, C., 2009. Determining the absolute abundance of dinoflagellate cysts in recent marine sediments: the Lycopodium marker-grain method put to the test. Review of Palaeobotany and Palynology 157, 238–252.

Millot, C., 1999. Circulation in the Western Mediterranean Sea. Journal of Marine Systems 20, 423–442.

Millot, C., 1987. The circulation of the Levantine Intermediate Water in the Algerian Basin. Journal of Geophysical Research: Oceans 92, 8265–8276.

Millot, C., 1985. Some features of the Algerian Current. Journal of Geophysical Research: Oceans 90, 7169–7176.

Millot, C., Taupier-Letage, I., 2005. Circulation in the Mediterranean Sea, in: Saliot, A. (Ed.), The Mediterranean Sea, Handbook of Environmental Chemistry. Springer, Berlin, Heidelberg, pp. 29–66.

Miola, A., 2012. Tools for Non-Pollen Palynomorphs (NPPs) analysis: A list of Quaternary NPP types and reference literature in English language (1972–2011). Review of Palaeobotany and Palynology 186, 142–161.

Moreno, A., Cacho, I., Canals, M., Prins, M.A., Sánchez-Goñi, M.-F., Grimalt, J.O., Weltje, G.J., 2002. Saharan dust transport and high-latitude glacial climatic variability: the Alboran Sea record. Quaternary Research 58, 318–328.

Morrill, C., LeGrande, A.N., Renssen, H., Bakker, P., Otto-Bliesner, B.L., 2013. Model sensitivity to North Atlantic freshwater forcing at 8.2 ka. Climate of the Past 9, 955–968.

Naughton, F., Sánchez Goñi, M.F., Drago, T., Conceição Freitas, M., Oliveira, A., 2007. Holocene changes in the Douro estuary (Northwestern Iberia). Journal of Coastal Research 23, 711–720.

Oppo, D.W., McManus, J.F., Cullen, J.L., 2006. Evolution and demise of the Last Interglacial warmth in the subpolar North Atlantic. Quaternary Science Reviews 25, 3268–3277.

Osman, M.K., Bessedik, M., Belkebir, L., Mansouri, M.E.H., Atik, A., Belkhir, A., Rubino, J.-L., Satour, L., Belhadji, A., 2021. Messinian to Piacenzian deposits, erosion, and subsequent marine bioevents in the Dahra Massif (Lower Chelif Basin, Algeria). Arabian Journal of Geosciences 14, 1–36.

Ozenda, P., 1975. Sur les étages de la végétation dans les montagnes du bassin méditerranéen., Documentation de cartographie écologique 16, 1–32.

Pausas, J.G., Vallejo, V.R., 1999. The role of fire in European Mediterranean ecosystems, in: Remote Sensing of Large Wildfires. Springer, pp. 3–16.

Peliz, A., Marchesiello, P., Santos, A.M.P., Dubert, J., Teles- Machado, A., Marta- Almeida, M., Le Cann, B., 2009. Surface circulation in the Gulf of Cadiz: 2. Inflow- outflow coupling and the Gulf of Cadiz slope current. Journal of Geophysical Research: Oceans 114.

Peñalba, M.C., Arnold, M., Guiot, J., Duplessy, J.-C., de Beaulieu, J.-L., 1997. Termination of

the last glaciation in the Iberian Peninsula inferred from the pollen sequence of Quintanar de la Sierra. Quaternary Research 48, 205–214.

Penaud, A., Eynaud, F., Sánchez-Goñi, M., Malaizé, B., Turon, J.-L., Rossignol, L., 2011. Contrasting sea-surface responses between the western Mediterranean Sea and eastern subtropical latitudes of the North Atlantic during abrupt climatic events of MIS 3. Marine Micropaleontology 80, 1–17.

Penaud, A., Eynaud, F., Voelker, A.H.L., Turon, J.-L., 2016. Palaeohydrological changes over the last 50 ky in the central Gulf of Cadiz: complex forcing mechanisms mixing multi-scale processes. Biogeosciences 13, 5357–5377.

Pérez-Folgado, M., Sierro, F.J., Flores, J.A., Cacho, I., Grimalt, J.O., Zahn, R., Shackleton, N., 2003. Western Mediterranean planktonic foraminifera events and millennial climatic variability during the last 70 kyr. Marine Micropaleontology 48, 49–70.

Perkins, H., Pistek, P., 1990. Circulation in the Algerian Basin during June 1986. Journal of Geophysical Research: Oceans 95, 1577–1585.

~~Perrodon, A., 1957. Etude géologique des bassins néogènes sublittoraux de l'Algérie occidentale.~~

Perşoiu, A., Ionita, M., Weiss, H., 2019. Atmospheric blocking induced by the strengthened Siberian High led to drying in west Asia during the 4.2 ka BP event–a hypothesis. Climate of the Past 15, 781–793.

Polunin, O., Walters, M., 1985. Guide to the vegetation of Britain and Europe. Oxford University Press.

Pons, A., Reille, M., 1988. The Holocene-and Upper Pleistocene pollen record from Padul (Granada, Spain): a new study. Palaeogeography, Palaeoclimatology, Palaeoecology 66, 243–263.

Pross, J., Kotthoff, U., Müller, U.C., Peyron, O., Dormoy, I., Schmiedl, G., Kalaitzidis, S., Smith, A.M., 2009. Massive perturbation in terrestrial ecosystems of the Eastern Mediterranean region associated with the 8.2 kyr BP climatic event. Geology 37, 887–890.

Raimbault, P., Coste, B., Boulhadid, M., Boudjellal, B., 1993. Origin of high phytoplankton concentration in deep chlorophyll maximum (DCM) in a frontal region of the Southwestern Mediterranean Sea (Algerian Current). Deep Sea Research Part I: Oceanographic Research Papers 40, 791–804.

Reille, M., 1992. Pollen et spores d'Europe et d'Afrique du Nord. Laboratoire de Botanique historique et Palynologie.

Reimer, P.J., Austin, W.E., Bard, E., Bayliss, A., Blackwell, P.G., Ramsey, C.B., Butzin, M., Cheng, H., Edwards, R.L., Friedrich, M., 2020. The IntCal20 Northern Hemisphere radiocarbon age calibration curve (0–55 cal kBP). Radiocarbon 62, 725–757.

1777 Richter, T.O., Van der Gaast, S., Koster, B., Vaars, A., Gieles, R., de Stigter, H.C., De Haas,
1778 H., van Weering, T.C., 2006. The Avaatech XRF Core Scanner: technical description
1779 and applications to NE Atlantic sediments. Geological Society, London, Special
1780 Publications 267, 39–50.
1781
1782 Rochon, A., De Vernal, A., Turon, J.-L., Matthießen, J., Head, M.J., 1999. Distribution of recent
1783 dinoflagellate cysts in surface sediments from the North Atlantic Ocean and adjacent
1784 seas in relation to sea-surface parameters. American Association of Stratigraphic
1785 Palynologists Contribution Series 35, 1–146.
1786
1787 Rodrigo-Gámiz, M., Martínez-Ruiz, F., Jiménez-Espejo, F.J., Gallego-Torres, D., Nieto-
1788 Moreno, V., Romero, O., Ariztegui, D., 2011. Impact of climate variability in the
1789 western Mediterranean during the last 20,000 years: oceanic and atmospheric responses.
1790 Quaternary Science Reviews 30, 2018–2034.
1791
1792 Rogerson, M., Colmenero- Hidalgo, E., Levine, R.C., Rohling, E.J., Voelker, A.H.L., Bigg,
1793 G.R., Schönfeld, J., Cacho, I., Sierro, F.J., Löwemark, L., 2010. Enhanced
1794 Mediterranean- Atlantic exchange during Atlantic freshening phases. Geochemistry,
1795 Geophysics, Geosystems 11.
1796
1797 Rohling, E., 1994. Review and new aspects concerning the formation of eastern Mediterranean
1798 sapropels. Marine Geology 122, 1–28.
1799
1800 Rohling, E., Den Dulk, M., Pujol, C., Vergnaud-Grazzini, C., 1995. Abrupt hydrographic
1801 change in the Alboran Sea (western Mediterranean) around 8000 yrs BP. Deep Sea
1802 Research Part I: Oceanographic Research Papers 42, 1609–1619.
1803
1804 Rohling, E., Hayes, A., De Rijk, S., Kroon, D., Zachariasse, W.J., Eisma, D., 1998. Abrupt cold
1805 spells in the northwest Mediterranean. Paleoceanography 13, 316–322.
1806
1807 Rohling, E., Marino, G., Grant, K.M., 2015. Mediterranean climate and oceanography, and the
1808 periodic development of anoxic events (sapropels). Earth-Science Reviews 143, 62–97.
1809
1810 Rohling, E., Mayewski, P., Abu-Zied, R., Casford, J., Hayes, A., 2002. Holocene atmosphere-
1811 ocean interactions: records from Greenland and the Aegean Sea. Climate Dynamics 18,
1812 587–593.
1813
1814 Rohling, E., Sprovieri, M., Cane, T., Casford, J.S., Cooke, S., Bouloubassi, I., Emeis, K.C.,
1815 Schiebel, R., Rogerson, M., Hayes, A., 2004. Reconstructing past planktic foraminiferal
1816 habitats using stable isotope data: a case history for Mediterranean sapropel S5. Marine
1817 Micropaleontology 50, 89–123.
1818
1819 Rohling, E.J., Abu-Zied, R., Casford, J.S.L., Hayes, A., Hoogakker, B.A.A., 2009. The marine
1820 environment: present and past. The physical geography of the Mediterranean 33–67.
1821
1822 Rossignol-Strick, M., 1985. Mediterranean Quaternary sapropels, an immediate response of the
1823 African monsoon to variation of insolation. Palaeogeography, palaeoclimatology,
1824 palaeoecology 49, 237–263.
1825
1826 Rossignol-Strick, M., Nesteroff, W., Olive, P., Vergnaud-Grazzini, C., 1982. After the deluge:

Mediterranean stagnation and sapropel formation. Nature 295, 105–110.

Rouis-Zargouni, I., Turon, J.-L., Londeix, L., Essallami, L., Kallel, N., Sicre, M.-A., 2010. Environmental and climatic changes in the central Mediterranean Sea (Siculo–Tunisian Strait) during the last 30 ka based on dinoflagellate cyst and planktonic foraminifera assemblages. Palaeogeography, Palaeoclimatology, Palaeoecology 285, 17–29.

Rouis-Zargouni, I., Turon, J.-L., Londeix, L., Kallel, N., Essallami, L., 2012. The last glacial-interglacial transition and dinoflagellate cysts in the western Mediterranean Sea. Comptes Rendus Geoscience 344, 99–109.

Ruan, J., Kherbouche, F., Genty, D., Blamart, D., Cheng, H., Dewilde, F., Hachi, S., Edwards, R.L., Régnier, E., Michelot, J.-L., 2016. Evidence of a prolonged drought ca. 4200 yr BP correlated with prehistoric settlement abandonment from the Gueldaman GLD1 Cave, Northern Algeria. Climate of the Past 12, 1–14.

Sanchez Goñi, M.F., Cacho, I., Turon, J.-L., Guiot, J., Sierro, F.J., Peypouquet, J.P., Grimalt, J.O., Shackleton, N.J., 2002. Synchroneity between marine and terrestrial responses to millennial scale climatic variability during the last glacial period in the Mediterranean region. Climate dynamics 19, 95–105.

Schäfer, I.K., Lanny, V., Franke, J., Eglinton, T.I., Zech, M., Vysloužilová, B., Zech, R., 2016. Leaf waxes in litter and topsoils along a European transect. Soil 2, 551–564.

Siani, G., Magny, M., Paterne, M., Debret, M., Fontugne, M., 2013. Paleohydrology reconstruction and Holocene climate variability in the South Adriatic Sea. Clim. Past 9, 499–515.

Siani, G., Paterne, M., Arnold, M., Bard, E., Métivier, B., Tisnerat, N., Bassinot, F., 2000. Radiocarbon reservoir ages in the Mediterranean Sea and Black Sea. Radiocarbon 42, 271–280.

Sicre, M.-A., Ternois Y., Miquel J.-C., and Marty J-C, Alkenones in the Mediterranean Sea: interannual variability and vertical transfer. *Geophysical Research Letters* ***26***, 12, 1735-1738, 1999.

Sicre, M.-A., Jalali, B., Eiríksson, J., Knudsen, K.-L., Klein, V., Pellichero, V., 2021. Trends and centennial-scale variability of surface water temperatures in the North Atlantic during the Holocene. Quaternary Science Reviews 265, 107033.

Sicre, M.-A., Jalali, B., Martrat, B., Schmidt, S., Bassetti, M.-A., Kallel, N., 2016. Sea surface temperature variability in the North Western Mediterranean Sea (Gulf of Lion) during the Common Era. Earth and Planetary Science Letters 456, 124–133.

Stambouli-Essassi, S., Roche, E., Bouzid, S., 2007. Evolution de la végétation et du climat dans le Nord-ouest de la Tunisie au cours des 40 derniers millénaires. Geo-Eco-Trop 31, 171–214.

Stockmarr, J.A., 1971. Tabletes with spores used in absolute pollen analysis. Pollen spores 13, 615–621.

Stommel, H., Bryden, H., Mangelsdorf, P., 1973. Does some of the Mediterranean outflow

come from great depth? Pure and Applied Geophysics 105, 879–889.

Stuiver, M., Reimer, P.J., 1993. Extended 14C data base and revised CALIB 3.0 14C age calibration program. Radiocarbon 35, 215–230.

Tachikawa, K., Vidal, L., Cornuault, M., Garcia, M., Pothin, A., Sonzogni, C., Bard, E., Menot, G., Revel, M., 2015. Eastern Mediterranean Sea circulation inferred from the conditions of S1 sapropel deposition. Climate of the Past 11, 855–867.

Targarona, J., Warnaar, J., Boessenkool, K.P., Brinkhuis, H., Canals, M., 1999. Recent dinoflagellate cyst distribution in the North Canary Basin, NW Africa. Grana 38, 170–178.

Tassin, C., 2012. Paysages végétaux du domaine méditerranéen: Bassin méditerranéen, Californie, Chili central, Afrique du Sud, Australie méridionale. IRD éditions.

Tinner, W., van Leeuwen, J.F., Colombaroli, D., Vescovi, E., van der Knaap, W.O., Henne, P.D., Pasta, S., D'Angelo, S., La Mantia, T., 2009. Holocene environmental and climatic changes at Gorgo Basso, a coastal lake in southern Sicily, Italy. Quaternary Science Reviews 28, 1498–1510.

Tintore, J., Violette, P.E.L., Blade, I., Cruzado, A., 1988. A Study of an Intense Density Front in the Eastern Alboran Sea: The Almeria–Oran Front. Journal of Physical Oceanography 18, 1384–1397.

Toucanne, S., Jouet, G., Ducassou, E., Bassetti, M.-A., Dennielou, B., Minto'o, C.M.A., Lahmi, M., Touyet, N., Charlier, K., Lericolais, G., 2012. A 130,000-year record of Levantine Intermediate Water flow variability in the Corsica Trough, western Mediterranean Sea. Quaternary Science Reviews 33, 55–73.

Toucanne, S., Mulder, T., Schönfeld, J., Hanquiez, V., Gonthier, E., Duprat, J., Cremer, M., Zaragosi, S., 2007. Contourites of the Gulf of Cadiz: a high-resolution record of the paleocirculation of the Mediterranean outflow water during the last 50,000 years. Palaeogeography, Palaeoclimatology, Palaeoecology 246, 354–366.

Turon, J.-L., 1984. Direct land/sea correlations in the last interglacial complex. Nature 309, 673–676.

Turon, J.-L., Lézine, A.-M., Denèfle, M., 2003. Land–sea correlations for the last glaciation inferred from a pollen and dinocyst record from the Portuguese margin. Quaternary Research 59, 88–96.

Turon, J.-L., Londeix, L., 1988. Les assemblages de kystes de dinoflagellés en Méditerranée occidentale (Mer d'Alboran). Mise en évidence de l'évolution des paléoenvironnements depuis le dernier maximum glaciaire. Bulletin des Centres de recherches exploration-production Elf-Aquitaine 12, 313–344.

Tzedakis, P.C., 2007. Seven ambiguities in the Mediterranean palaeoenvironmental narrative. Quaternary Science Reviews 26, 2042–2066.

Tzoraki, O., Nikolaidis, N.P., 2007. A generalized framework for modeling the hydrologic and biogeochemical response of a Mediterranean temporary river basin. Journal of Hydrology 346, 112–121.

Van Geel, B., 1972. Palynology of a section from the raised peat bog 'Wietmarscher moor ', with special reference to fungal remains. Acta Botanica Neerlandica 21, 261–284.

Van Nieuwenhove, N., Pospelova, V., Anne, de V., Rochon, A., 2020. A historical perspective on the development of the Northern Hemisphere modern dinoflagellate cyst database. Marine Micropaleontology 159, 101824.

Vannière, B., Colombaroli, D., Chapron, E., Leroux, A., Tinner, W., Magny, M., 2008. Climate versus human-driven fire regimes in Mediterranean landscapes: the Holocene record of Lago dell'Accesa (Tuscany, Italy). Quaternary Science Reviews 27, 1181–1196.

Viúdez, Á., Tintoré, J., 1995. Time and space variability in the eastern Alboran Sea from March to May 1990. Journal of Geophysical Research: Oceans 100, 8571–8586.

Voelker, A.H., Aflidason, A., 2015. Refining the Icelandic tephrachronology of the last glacial period–the deep-sea core PS2644 record from the southern Greenland Sea. Global and Planetary Change 131, 35–62.

Voelker, A.H., Lebreiro, S.M., Schönfeld, J., Cacho, I., Erlenkeuser, H., Abrantes, F., 2006. Mediterranean outflow strengthening during northern hemisphere coolings: a salt source for the glacial Atlantic? Earth and Planetary Science Letters 245, 39–55.

Vogts, A., Moossen, H., Rommerskirchen, F., Rullkötter, J., 2009. Distribution patterns and stable carbon isotopic composition of alkanes and alkan-1-ols from plant waxes of African rain forest and savanna C3 species. Organic Geochemistry 40, 1037–1054.

Wall, D., Dale, B., Lohmann, G.P., Smith, W.K., 1977. The environmental and climatic distribution of dinoflagellate cysts in modern marine sediments from regions in the North and South Atlantic Oceans and adjacent seas. Marine micropaleontology 2, 121–200.

Watts, W.A., Allen, J.R.M., Huntley, B., Fritz, S.C., 1996. Vegetation history and climate of the last 15,000 years at Laghi di Monticchio, southern Italy. Quaternary Science Reviews 15, 113–132.

Zanchetta, G., Drysdale, R.N., Hellstrom, J.C., Fallick, A.E., Isola, I., Gagan, M.K., Pareschi, M.T., 2007. Enhanced rainfall in the Western Mediterranean during deposition of sapropel S1: stalagmite evidence from Corchia cave (Central Italy). Quaternary Science Reviews 26, 279–286.

Zielhofer, C., Faust, D., 2008. Mid-and Late Holocene fluvial chronology of Tunisia. Quaternary Science Reviews 27, 580–588.

Zielhofer, C., Fletcher, W.J., Mischke, S., De Batist, M., Campbell, J.F., Joannin, S., Tjallingii, R., El Hamouti, N., Junginger, A., Stele, A., 2017. Atlantic forcing of Western Mediterranean winter rain minima during the last 12,000 years. Quaternary Science

Reviews 157, 29–51.

Zonneveld, K.A.F., Bockelmann, F., Holzwarth, U., 2007. Selective preservation of organic-walled dinoflagellate cysts as a tool to quantify past net primary production and bottom water oxygen concentrations. Marine Geology 237, 109–126.

Zonneveld, K.A.F., Ganssen, G., Troelstra, S., Versteegh, G.J., Visscher, H., 1997. Mechanisms forcing abrupt fluctuations of the Indian Ocean summer monsoon during the last deglaciation. Quaternary Science Reviews 16, 187–201.

Zonneveld, K.A.F., Hoek, R.P., Brinkhuis, H., Willems, H., 2001. Geographical distributions of organic-walled dinoflagellate cysts in surficial sediments of the Benguela upwelling region and their relationship to upper ocean conditions. Progress in Oceanography 48, 25–72.

Zonneveld, K.A.F., Versteegh, G., Kodrans-Nsiah, M., 2008. Preservation and organic chemistry of Late Cenozoic organic-walled dinoflagellate cysts: A review. Marine Micropaleontology 68, 179–197.

Table

Table 1

Code	Spectrometer	Depth (cm)	Dated material	^{14}C age	Error	^{14}C age – reservoir age	IntCal20 Cal BP Min-Max	Error σ
SacA43123	ECHoMICADAS	3	*G. bulloides*	170	30	-230	**0** 0-0	1 σ
SacA55619*	ARTEMIS	31[a]	*G. bulloides*	820	30	420	**491,5** 472-511	1 σ
SacA55620	ARTEMIS	231	*G. bulloides*	1400	30	1000	**928,5** 900-957	2 σ
GifA20376	ECHoMICADAS	311	*G. bulloides*	1290	60	890	**817** 716-918	2 σ
SacA55621	ARTEMIS	431	*G. bulloides*	2165	30	1765	**1644,5** 1571-1718	2 σ
GifA21150	ECHoMICADAS	522	*G. bulloides*	3610	70	3210	**3424** 3357-3723	1 σ
GifA18283	ECHoMICADAS	531	*G. bulloides*	3870	80	3470	**3737,5** 3634-3841	1 σ
SacA54337	ARTEMIS	531	*G. bulloides*	3820	30	3420	**3647,5** 4229-4522	2 σ
GifA20378	ECHoMICADAS	550	*G. bulloides*	4330	60	3930	**4375,5** 4229-4522	2 σ
GifA21151	ECHoMICADAS	559	*G. bulloides*	4390	60	3990	**4432** 4245-4619	2 σ
GifA20380	ECHoMICADAS	579	*G. bulloides*	5000	60	4600	**5342,5** 5214-5471	2 σ
GifA21152	ECHoMICADAS	581	*G. bulloides*	5060	70	4660	**5392** 5315-5469	1 σ
SacA55622	ARTEMIS	631	*G. bulloides*	6200	30	5800	**6584** 6499-6669	2 σ
GifA18282	ECHoMICADAS	731	*G. bulloides*	8470	70	8070	**8917,5** 8696-9139	2 σ
SacA54338	ARTEMIS	731	*G. bulloides*	7990	35	7590	**8392** 8374-8410	1 σ
GifA18256*	ECHoMICADAS	931[b]	*G. bulloides*	11110	270	10710	**12488,5** 11808-13169	2 σ
SacA54339	ARTEMIS	931	*G. bulloides*	10600	40	10200	**11867,5** 11739-11996	2 σ
SacA54335	ARTEMIS	978	Gastéropode	11000	40	10600	**12653** 12616-12690	1 σ
SacA54336	ARTEMIS	978	Gastéropode	11015	40	10615	**12659** 12621-12697	1 σ
SacA55623	ARTEMIS	1031	*G. bulloides*	12445	40	12045	**13920,5** 13804-14037	2 σ

2023 Table 2

2024

Pollen zones	Limits	Interval (cm)	Age (cal BP)	Description of Dinocyst zones	Pollen zones	Inferred hydrological changes	Description of pollen zone	Vegetation changes	Inferred climatic changes	Non-pollen palynomorphs remarks
MD04-5	Top - f	0 - 370	0 - 1 400	High values of *Brigantedinium* spp. (60% mainly), *S. mirabilis* and *O. centrocarpum*. Increasing values of estuarine-stratified taxa and thermophilous full-oceanic taxa. Diverse coastal productivity and upwelling heterotrophic assemblage. Occurences of *Lejeunecysta* spp.	Highest heterotrophic taxa representations. Mixed upwelling and coastal productivity.	Upwelling driven productivity mixed with river discharge induced coastal productivity. Increasing oligotrophic conditions signal	Strongest representation of *Cichorioideae* (up to 35% mainly), *Asteroideae*. Stable percentages of *Poaceae*, *Quercus ilex*, deciduous *Quercus*, *Olea*, *Pistacia, Juniperus*, *Cupressus*, *Cedrus*. Increasing percentages of *Ephedra* and *Atremisia*. Increasing occurrences and representations of human impact taxa.	Open shrubs and steppe vegetation combined with open mediterranean forest forming mattorals and maquis. Potential human activity expansion.	Increasing aridity	Freshwater algae stable representation. Glomus high abundances, ascospores stable abundances. Occasional coprophilous abundances.
	f - e	370 - 485	1 400 - 2 700	High values of *Brigantedinium* spp. (60% mainly) followed by stable represented *S. mirabilis* and *O. centrocarpum*. Diverse coastal productivity and upwelling heterotrophic assemblage. High representation of *T. applanatuml.*	Highest heterotrophic taxa representations. High upwelling and coastal productivity.	Upwelling drived productivity under relatively stable Atlantic influence.	Strong increase of *Cichorioideae* (30% mainly), *Asteroideae*. Stable percentages of *Poaceae*, *Quercus ilex,* deciduous *Quercus*, *Olea*, *Pistacia*, *Juniperus*, *Cupressus*, *Cedrus*, *Ephedra* and *Artemisia*.	Open shrubs and steppe vegetation combined with open mediterranean forest forming mattorals and maquis.	Increasing aridity	Freshwater algae stable representation. Glomus high abundances, ascospores stable abundances.
MD04-4	e- d	485 - 575	2 700 - 5 120	High values of *S. mirabilis* (30% mainly) and *I. aculeatum*. High representations of *L. machaerophorum*. Increasing percentages of *S. bentorii*, *N. labyrinthus* and *T. applanatum*.	Highrepresentation of phototrophic taxa. Upwelling cortege strong representation.	Intense upwelling activity. Intense oceanic influence. Seasonal oligotrophic stratified warm surface waters persistent signal.	Increasing of *Chenopodiaceae*, *Cichorioideae*, *Artemisia* and *Ephedra*. Small decrease of *Quercus ilex* and decrease of *Pistacia, Quercus suber* and *Cedrus*.	Open mediterranean forest with extended underbrush and maquis of Cichorioideae, Asteraceae and Poaceae steppe	Decreasing rainfalls with centennial oscillations	Lower freshwater algae and Glomus abundances. Peak of ascospores around 540 cm.
MD04-3	d - c	575 - 740	5 120 - 8 600	High values of Brigantedinium spp. increasing percentages of I. aculeatum (15-20% mainly) and S. mirabilis. Rare occurrences of *Lejeunecysta* spp. And *T. applanatum.*	Stable strong heterotrophic representation. Highest percentages of the Thermophilous full-oceanic taxa majorly represented by Impagidinium aculeatum.	Strongest oligotrophic surface conditions, increasing stratification and sea surface temperature. Persitant upwelling productivity signal.	Highest trees percentages. Increasing percentages of *Cupressaceae*, *Pistacia* and *Olea*, *Quercus ilex* and *Poaceae*. Decrease of *Chenopodiaceae* and small decrease of *Cichorioideae* which peaks from 650 to 600 cm.	Open mediterranean oak forest combined with underbrush and maquis of Cichorioideae, Asteraceae and Poaceae	Increased humidity and temperature marked with centennial oscillations	Highest representations of freshwater algae. Stable high representation of Glomus and ascospores.

	c - b	740 - 910	8600 - 11 500	High percentages of *Brigantedinium* spp. (40 % mainly). Diverse coastal productivity and upwelling heterotrophic assemblage. Highest percentages of *O. centrocarpum* (10-20% mainly).	Increasing of the heterotrophic taxa representations. Increasing representation of thermophilous full-oceanic taxa.	Oligotrophic surface conditions, stratification and sea surface temperature. Persitant upwelling driven productivity.	Strong increase of *Quercus ilex*, deciduous *Quercus*, *Pistacia, Olea, Asteroideae*, *Cichorioideae* and *Poaceae*. Decrease of *Cedrus, Chenopodiaceae*, *Artemisia* and *Ephedra*. Increasing representation of monocotyledonae and pteridophyte spores.	Open mediterranean forest and underbush or maquis	Warmer conditions and gradual increased humidity	Stable high representation of Glomus and ascospores.
MD04-2	b - a	910 - 1 025	11 500 - 13 700	Increase of the *N. labyrinthus* percentages (30 - 35% mainly). Cold water taxa *S. lazus* and *B. tepikiense* are also represented in high values. *O. centrocarpum* shows stronger representations around 910-950 cm. Highest representation og the intern neritic taxa *S. ramosus*, *S. bentorii* and *S. membranaceus*.	Decrease of the heterotrophic taxa representation with the persistance of upwelling cortege taxa. Increasing percentages of cold water taxa and extern neritic photrophic taxa. Diversified assemblage.	Cold surface temperature. Strong oceanic influence. Highest productivity period in thesequence.	Highest representations of *Cedrus* (30% mainly) with two major peaks at 970 and 1000 cm (reaching more than 40%). Increase of *Chenopodiaceae*, *Artemisia* and *Ephedra* with a decrease ogf all *Quercus ilex*, *Quercus suber* and *Cupressaceae*.	Steppe with semi-desert plants. Sparse Pine and coniferous woodlands and Cedrus forests uplands.	Dry and cold conditions	Weak or lacking freshwater algae and fungal spores signal
MD04-1	a - Bottom	1 025 - 1 042	13 700 - 14 000	Dominance of *Brigantedinium* spp.	Dominanceof the heterotrophic taxon Birgantedinium spp.	Apparent productive conditions, active upwelling.	Dominance of *Chenopodiaceae*, *Cichorioideae* and *Poaceae* associated to *Artemisia* and *Ephedra*. Low representation of *Querus ilex* (less than 10 %) and *Cupressaceae*.	Dominating steppe with sparse mediterranean woodlands.	Dry conditions	Weak or lacking freshwater algae and fungal spores signal

Table 2

Figures

Figure 1

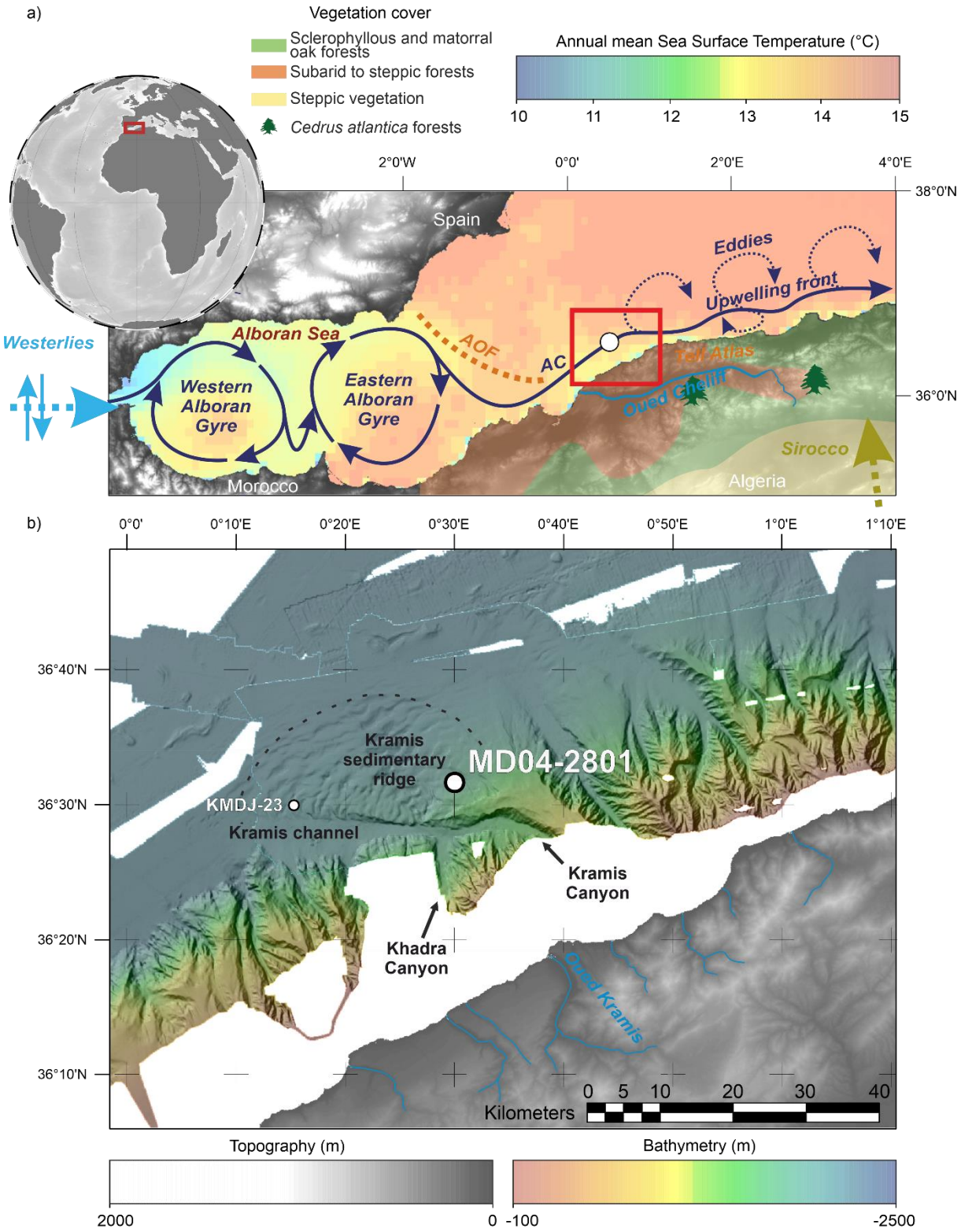

2034

2035 Figure 2

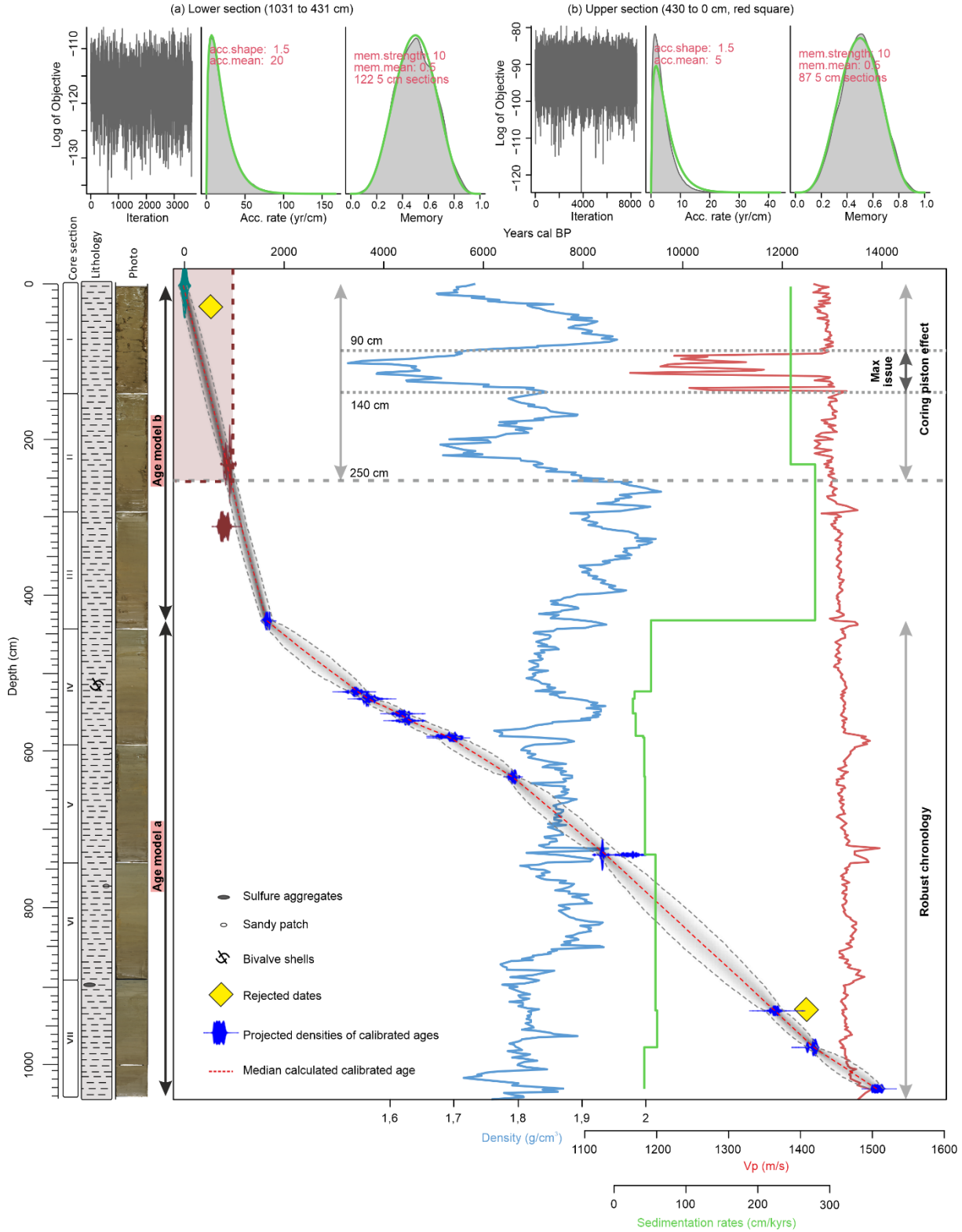

2036

2037

2038

2039

2040

2041 Figure 3

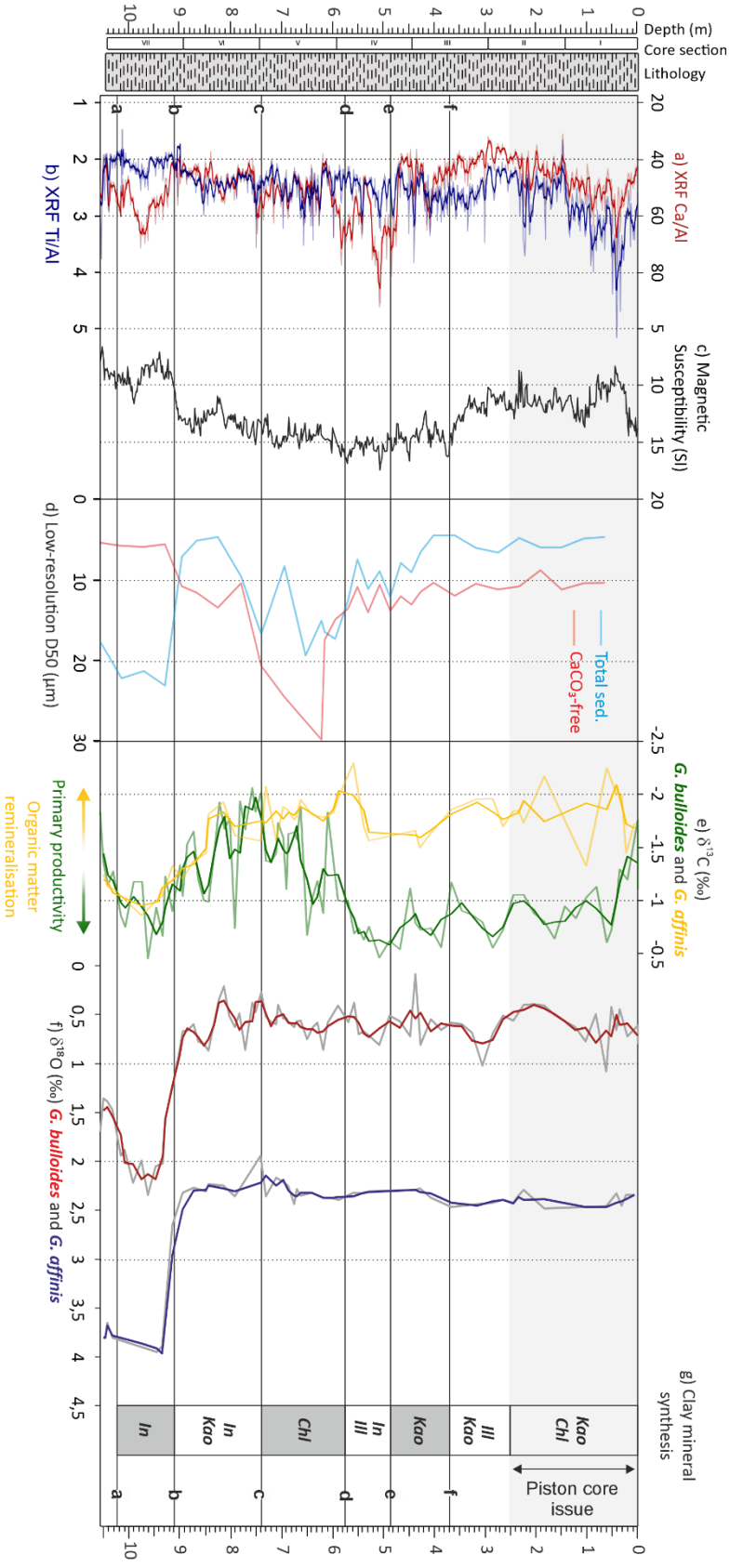

2042

2043

Figure 4

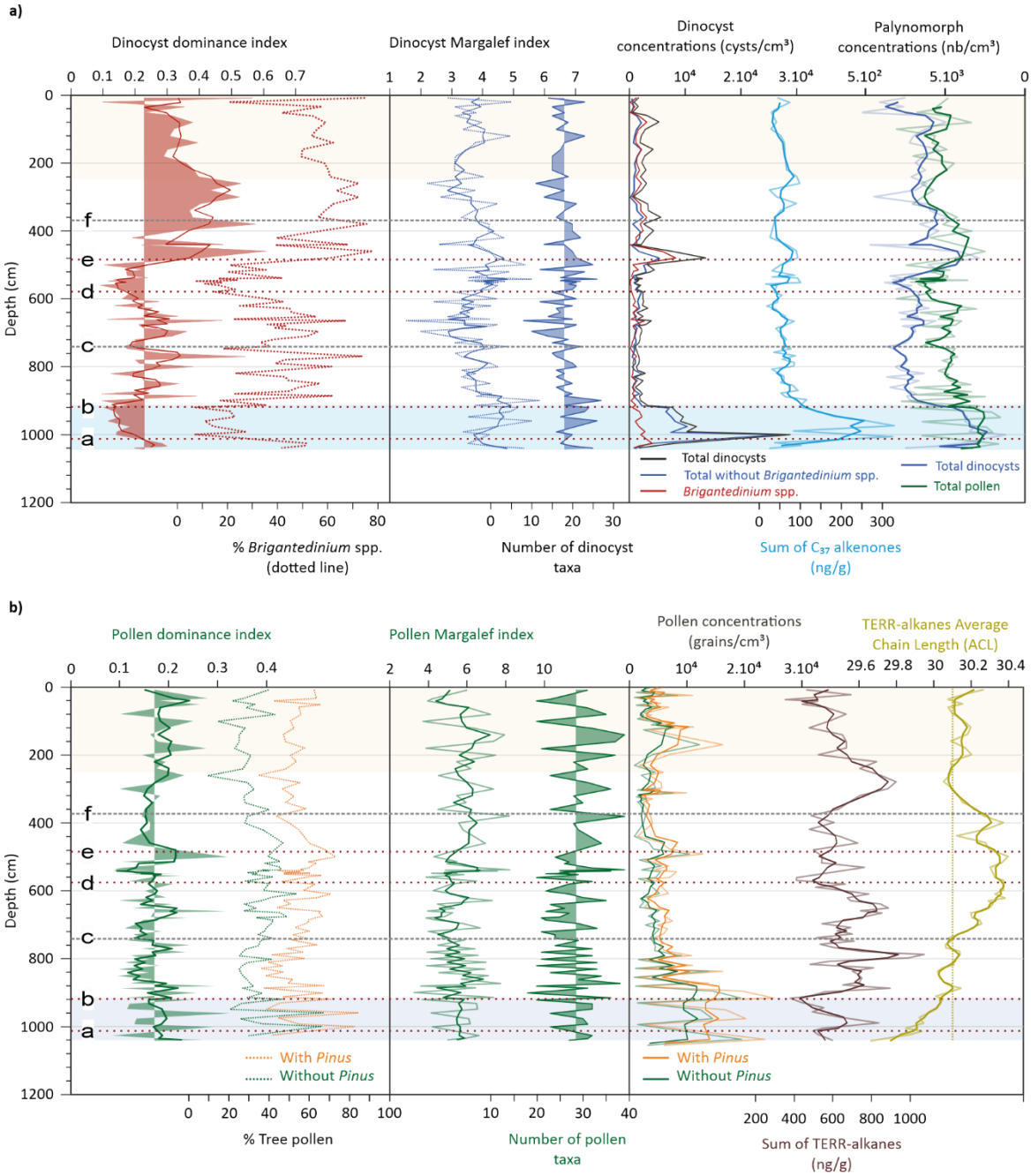
a)
Dinocyst dominance index
Dinocyst Margalef index
Dinocyst concentrations (cysts/cm³)
Palynomorph concentrations (nb/cm³)
Depth (cm)
Total dinocysts
Total without Brigantedinium spp.
Brigantedinium spp.
Total dinocysts
Total pollen
% Brigantedinium spp. (dotted line)
Number of dinocyst taxa
Sum of C37 alkenones (ng/g)
b)
Pollen dominance index
Pollen Margalef index
Pollen concentrations (grains/cm³)
TERR-alkanes Average Chain Length (ACL)
With Pinus
Without Pinus
With Pinus
Without Pinus
% Tree pollen
Number of pollen taxa
Sum of TERR-alkanes (ng/g)

2054 Figure 5

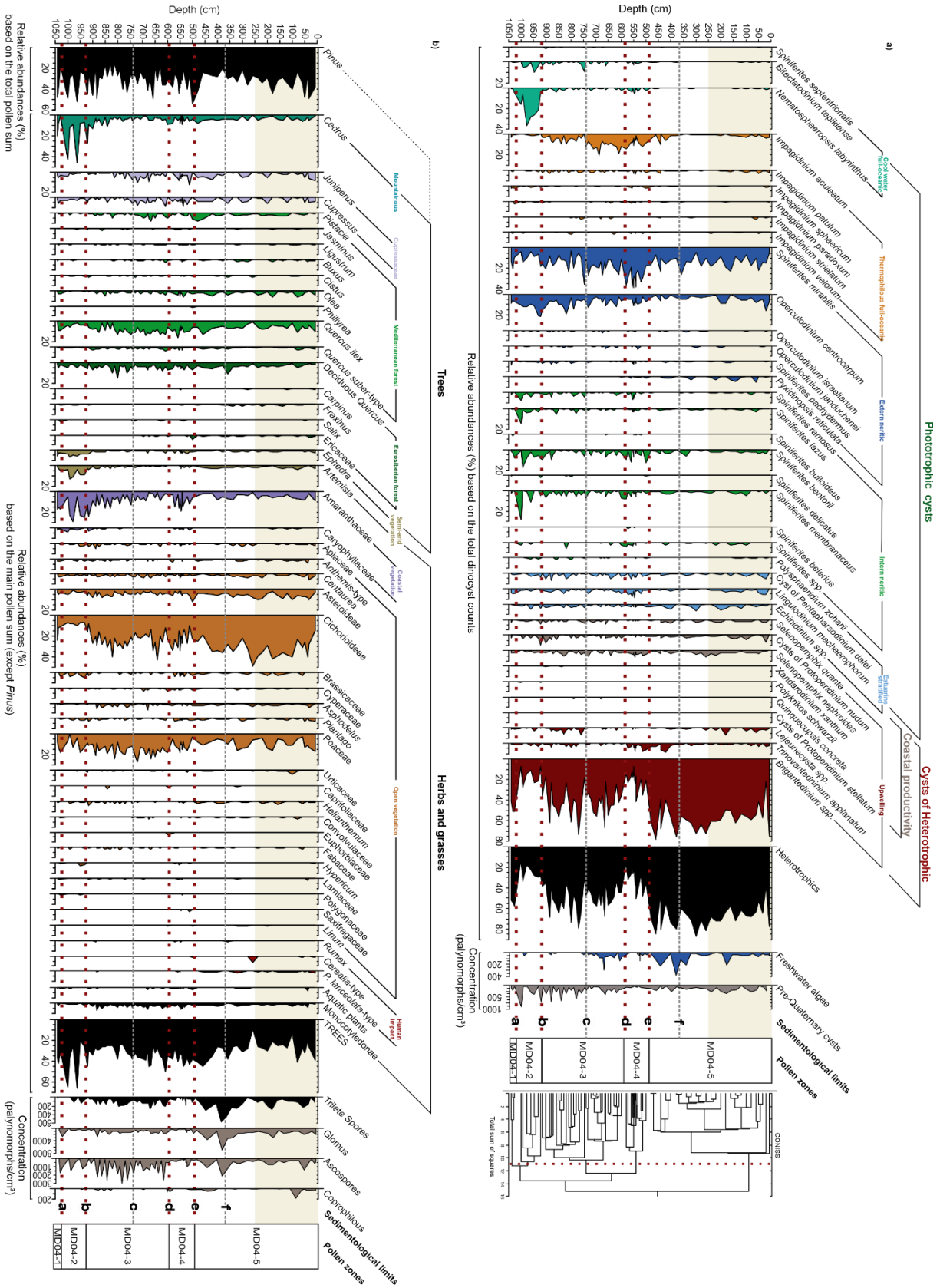

2055

2056

2057

Figure 6

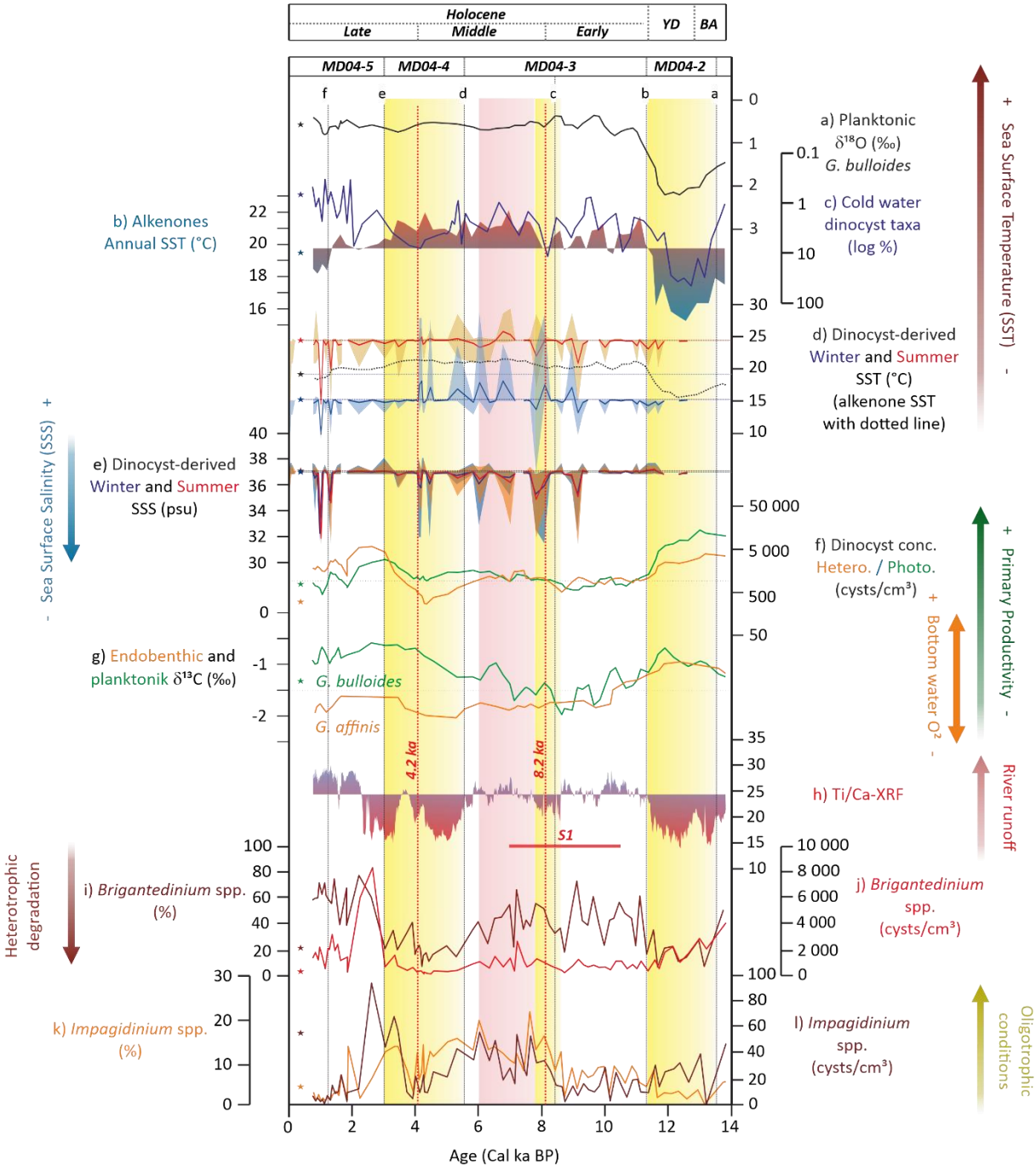
Holocene
Late
Middle
Early
YD
BA
MD04-5
MD04-4
MD04-3
MD04-2
f
e
d
c
b
a
a) Planktonic δ18O (‰) G. bulloides
b) Alkenones Annual SST (°C)
c) Cold water dinocyst taxa (log %)
d) Dinocyst-derived Winter and Summer SST (°C) (alkenone SST with dotted line)
+ Sea Surface Temperature (SST) -
- Sea Surface Salinity (SSS) +
e) Dinocyst-derived Winter and Summer SSS (psu)
f) Dinocyst conc. Hetero. / Photo. (cysts/cm³)
+ Primary Productivity -
+ Bottom water O2 -
g) Endobenthic and planktonik δ13C (‰)
G. bulloides
G. affinis
4.2 ka
8.2 ka
S1
h) Ti/Ca-XRF
River runoff
Heterotrophic degradation
i) Brigantedinium spp. (%)
j) Brigantedinium spp. (cysts/cm³)
k) Impagidinium spp. (%)
l) Impagidinium spp. (cysts/cm³)
Oligotrophic conditions
Age (Cal ka BP)

2068 Figure 7

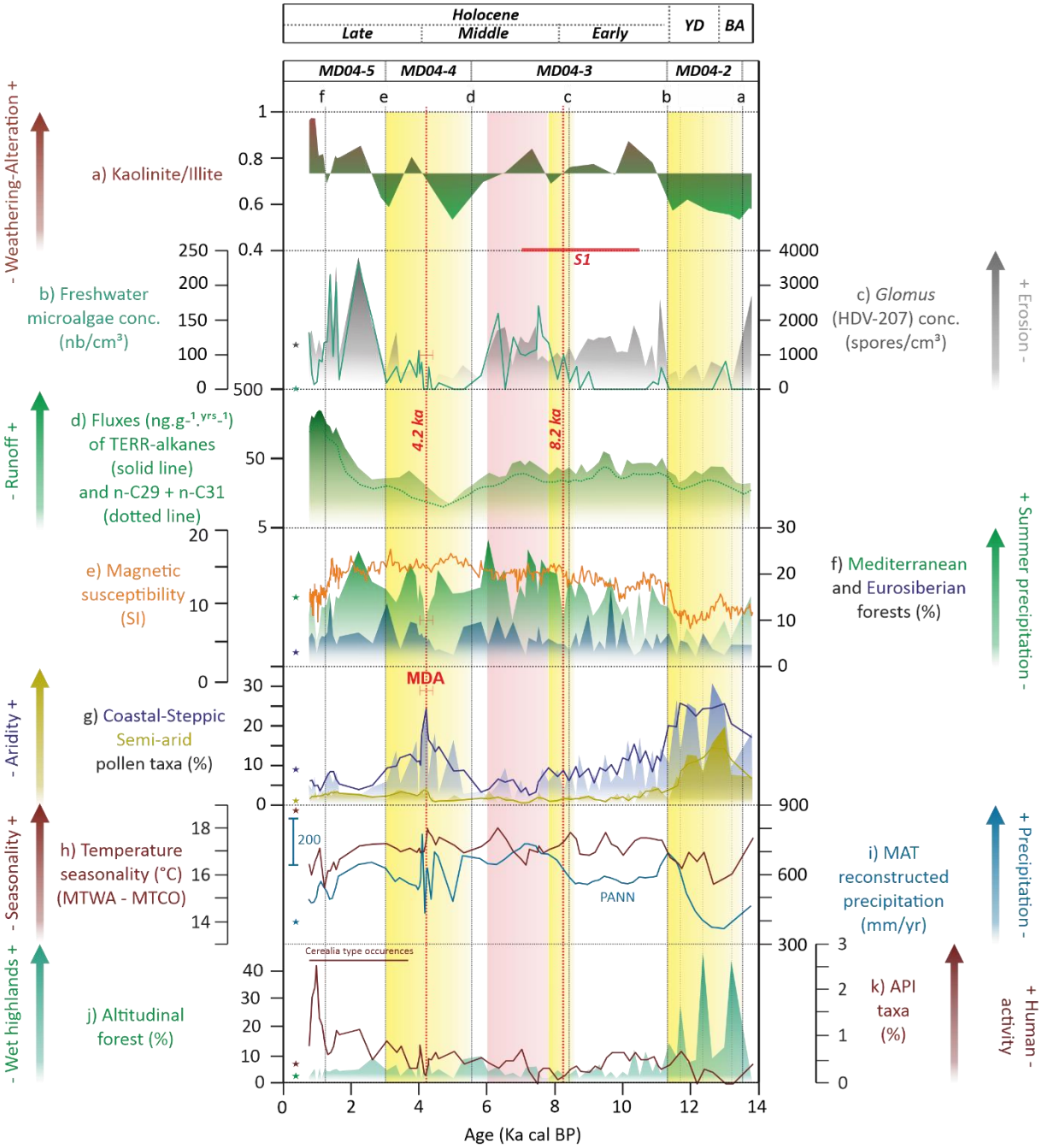

2069
2070
2071
2072
2073
2074
2075
2076
2077

2078 Figure 8

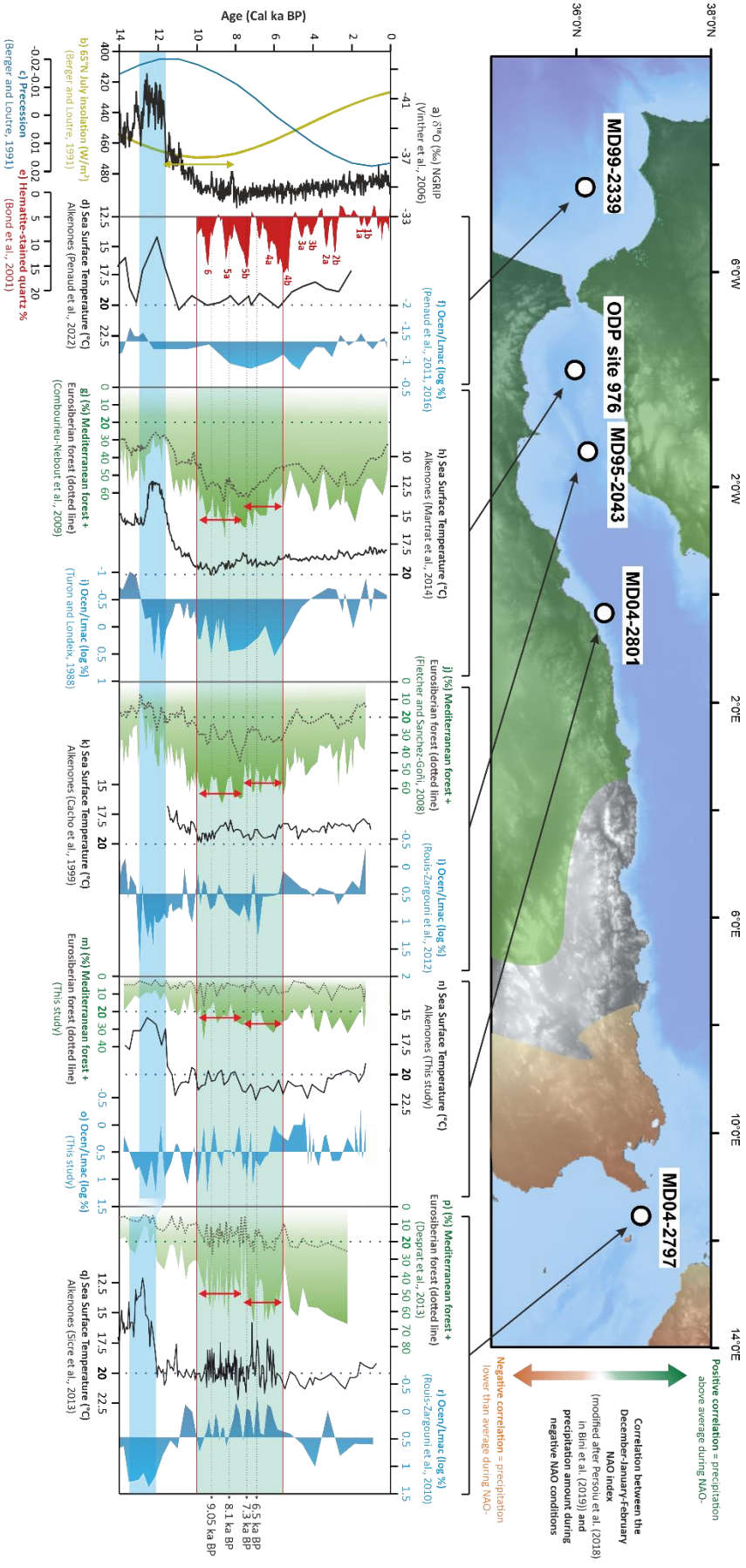

2079

Date:	Apr 05, 2023
To:	"Vincent Coussin" vincent.coussin@univ-brest.fr
From:	"Palaeogeography, Palaeoclimatology, Palaeoecology" support@elsevier.com
Subject:	Decision on submission to Palaeogeography, Palaeoclimatology, Palaeoecology
Attachment(s):	PALAEO-D-22-00553_R1.pdf

Manuscript Number: PALAEO-D-22-00553R1

Land-sea linkages on the Algerian Margin over the last 14 kyrs BP: climate variability at orbital to centennial timescales

Dear Dr. Coussin,

Thank you for submitting your manuscript to Palaeogeography, Palaeoclimatology, Palaeoecology.

I have completed my evaluation of your manuscript. I am happy with the responses to the reviewers however I have made corrections and suggestions for improvement of the abstract and one minor change to the introduction. These are mostly stylistic to simplify the writing and make the concrete results evident. Please see the PDF.

I invite you to resubmit your manuscript after addressing the comments below. Please resubmit your revised manuscript by Jun 04, 2023.

When revising your manuscript, please consider all issues mentioned in the reviewers' comments carefully: please outline every change made in response to their comments and provide suitable rebuttals for any comments not addressed. Please note that your revised submission may need to be re-reviewed.

To submit your revised manuscript, please log in as an author at https://www.editorialmanager.com/palaeo/, and navigate to the "Submissions Needing Revision" folder under the Author Main Menu.

Research Elements (optional)
This journal encourages you to share research objects - including your raw data, methods, protocols, software, hardware and more – which support your original research article in a Research Elements journal. Research Elements are open access, multidisciplinary, peer-reviewed journals which make the objects associated with your research more discoverable, trustworthy and promote replicability and reproducibility. As open access journals, there may be an Article Publishing Charge if your paper is accepted for publication. Find out more about the Research Elements journals at https://www.elsevier.com/authors/tools-and-resources/research-elements-journals?dgcid=ec_em_research_elements_email.

Palaeogeography, Palaeoclimatology, Palaeoecology values your contribution and I look forward to receiving your revised manuscript.

Kind regards,

Paul Hesse

Editor

Palaeogeography, Palaeoclimatology, Palaeoecology

Dear Editor,

We thank the editor for the suggestions and comments to improve the abstract and introduction of the paper. Modifications following comments and suggestions have been carefully addressed and are highlighted in red in the change reported version of the manuscript.

Please find the revised manuscript in the submission package.

Kind regards,

Vincent Coussin

More information and support

FAQ: How do I revise my submission in Editorial Manager?

https://service.elsevier.com/app/answers/detail/a_id/28463/supporthub/publishing/

You will find information relevant for you as an author on Elsevier's Author Hub:
https://www.elsevier.com/authors

FAQ: How can I reset a forgotten password?
https://service.elsevier.com/app/answers/detail/a_id/28452/supporthub/publishing/
For further assistance, please visit our customer service site:
https://service.elsevier.com/app/home/supporthub/publishing/
Here you can search for solutions on a range of topics, find answers to frequently asked questions, and learn more about Editorial Manager via interactive tutorials. You can also talk 24/7 to our customer support team by phone and 24/7 by live chat and email

#AU_PALAEO#

To ensure this email reaches the intended recipient, please do not delete the above code

Highlights

- Land-sea multiproxy approach on the Algerian Margin over the last 14 kyrs
- Productivity regimes closely associated with the vigour of the Algerian Current
- Settlement of modern production conditions since 3 ka BP
- First record of the Algerian Mega Drought event between 4.3 and 3.9 ka BP
- NPP fingerprint in marine sediments related to erosion and river runoff

" ***Palaeogeography, Palaeoclimatology, Palaeoecology*** "

Declaration of competing interest

Date : 24th of March, 2023

Your Name: Vincent Coussin

Manuscript Title: Land-sea linkages on the Algerian Margin over the last 14 kyrs BP: climate variability at orbital and multi-centennial timescales

We disclose any financial and personal relationships with other people or organizations that could inappropriately influence (bias) our work. We don't have any interests to declare.

We, the authors, declare that this manuscript is original, has not been published before and is not currently being considered for publication elsewhere.

We confirm that the manuscript has been read and approved by all named authors and that there are no other persons who satisfied the criteria for authorship but are not listed. We further confirm that the order of authors listed in the manuscript has been approved by all of us.

We understand that the Corresponding Author is the sole contact for the Editorial process.

He is responsible for communicating with the other authors about progress, submissions of revisions and final approval of proofs.

Sincerely,

On behalf of all authors

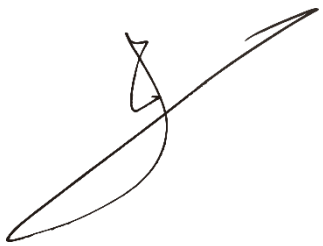

Revised Manuscript clean file (With no changes Marked) Click here to view linked References

Land-sea linkages on the Algerian Margin over the last 14 kyrs BP: climate variability at orbital to centennial timescales

Coussin V.[(a)], Penaud A.[(a)], Combourieu-Nebout N.[(b)], Peyron O. [(c)], Sicre M.-A.[(d)], Tisnérat-Laborde N.[(e)], Cattaneo A.[(a)], Babonneau N.[(a)]

(a) Univ. Brest, CNRS, Ifremer, Geo-Ocean, UMR 6538, F-29280 Plouzané, France

(b) HPNP, CNRS, UMR 7194, Département de Préhistoire du Muséum d'Histoire Naturelle, F-75013 Paris, France

(c) Univ. Montpellier 2, CNRS, UMR 5554, Institut des Sciences de l'Evolution de Montpellier (ISEM), 34095 Montpellier cedex 05, France

(d) LOCEAN, CNRS, Sorbonne Université, Campus Pierre et Marie Curie, F75005 Paris, France

(e) Laboratoire des Sciences du Climat et de l'Environnement, LSCE/IPSL, UMR 8212 UVSQ-CNRS-CEA, Avenue de la Terrasse, 91198 Gif-sur-Yvette, France.

*Corresponding author. Tel.: 02.89.49.87.41

E-mail address: vincent.coussin@univ-brest.fr vincent.coussin@gmail.com aurelie.penaud@univ-brest.fr

Highlights

- Land-sea multiproxy approach on the Algerian Margin over the last 14 kyrs
- Productivity regimes closely associated with the vigour of the Algerian Current
- Settlement of modern production conditions since 3 ka BP
- First record of the Algerian Mega Drought event between 4.3 and 3.9 ka BP
- NPP fingerprint in marine sediments related to erosion and river runoff

Abstract

Past and present environmental conditions over the Holocene along the Algerian coast involve complex atmosphere-hydrosphere-biosphere interactions and anthropogenic activities on adjacent watersheds. Atlantic Ocean surface waters entering the western Mediterranean Sea at the Gibraltar Strait create the Algerian Current, which flows along the North African coast in a succession of strong and large-scale eddies. Deep-water upwelling plumes are other recurrent hydrological features of the Algerian margin affecting regional environmental features. However, vegetation and paleohydrological changes that have occurred over the Holocene have not yet been described. To bridge this gap, a suite of paleoclimate proxies was analysed in marine core MD04-2801 (2,067 m water depth) at a secular-scale resolution over the last 14 kyrs BP. Terrestrial (pollen grains) and marine (dinoflagellate cysts or dinocysts) palynological assemblages, as well as sedimentological (grain-size analysis and XRD-based quantitative analysis of clay minerals) and biomarkers (alkenones and n-alkanes), were determined to explore the links between past sea surface hydrological conditions and regional environmental changes on nearby watersheds.

The over-representation of heterotrophic dinocyst taxa (*Brigantedinium* spp.) indicates strong planktonic productivity in the study area. Results shows that the links between dryness on land and surface hydrological conditions are expressed by : (i) recurrent upwelling cells during the relatively dry climate conditions of the Younger Dryas (12.7 to 11.7 ka BP), the Early Holocene (11.7 to 8.2 ka BP) and from 6 ka BP onwards, (ii) enhanced fluvial discharges between 8.2 and 6 ka BP during the African Humid Period concomitant with the colonization of coastal lands by Mediterranean forest. Middle to Late Holocene transition around 4.2 ka BP characterizes by the intense event reffered to here as the Algerian Mega Drought (4.3 to 3.9 ka BP).

Keywords: Holocene; Dinocysts; Pollen; Biomarkers; Clay analysis; Algerian Current

Abbreviations: AM: Algerian Margin; AC: Algerian Current; WMB: Western Mediterranean Basin; WMDW: Western Mediterranean Deep Waters; LIW: Ligurian Intermediate Waters; MOW: Mediterranean Outflow Waters; YD: Younger Dryas; B/A: Bölling-Alleröd.

1. Introduction

Interactions between low- and mid-latitude atmospheric circulations and local-scale configurations such as orography and coastal geomorphology, have created the specificities of the Mediterranean climate (Brayshaw et al., 2011). Furthermore, the summer season length depending on the vigor of the Hadley cell directly impacts summer droughts in the Mediterranean Basin (Lionello et al., 2006). In contrast, Mediterranean storm activity driving the main seasonal precipitation is strongly associated with the position and strength of the North-Atlantic mid-latitude storm tracks (Brayshaw et al., 2010). Consequently, the interactions between tropical convection and North-Atlantic storm tracks constitute a complex but essential element in understanding the long-term, rapid climate change that took place in the WMB during the Holocene. Climate changes during the last climatic cycle (e.g. Combourieu-Nebout et al., 1999, 2002; Sánchez-Goñi et al., 2002; Beaudouin et al., 2007; Bout-Roumazeilles et al., 2007; Brauer et al., 2007; Fletcher and Sánchez-Goñi, 2008; Kotthoff et al., 2008) have driven rapid paleoenvironmental changes in the Mediterranean basin.

Global warming, together with the generally high climatic and environmental sensitivity of this region raises questions concerning future environmental and human trajectories in the Mediterranean Basin, in particular due to subtropical aridification (IPCC report, 2019).

In this context, the Algerian Margin (AM) appears ideal to investigate both terrestrial (i.e. landscape changes) and marine (i.e. hydrological changes) ecosystems inherited from climate change and land-use practices over the Holocene. The AM, and mostly its westernmost part, is a highly productive area contrasting with the predominantly oligotrophic waters of the Western Mediterranean Basin (Sournia, 1973; Lohrenz et al., 1988). Strong riverine inputs (i.e. flash-flood episodes) to coastal waters and upwelling cells result in nutrient-enriched surface waters (Raimbault et al., 1993). These hydrological patterns provide understanding of the distribution of planktonic organisms as recently discussed for fossilized dinocysts at the scale of the Western Mediterranean Basin (WMB) (Coussin *et al*., 2022).

Numerous studies have shown the rapid response of Mediterranean environments to Holocene climate variability (e.g. Rohling et al., 2002; Fletcher et al., 2013; Chabaud et al., 2014; Sicre et al., 2016; Jalali et al., 2016; 2017, 2018; Di Rita et al., 2018; Bini et al., 2021), including research on remote short-term events of the North Atlantic Basin (e.g. Bond et al., 1997, 2001; Mayewski et al., 2004; Sicre et al., 2021). However, Holocene paleoenvironmental changes along the northern African margin, between the Alboran Sea (e.g. Combourieu-Nebout et al.,

1999, 2009 ; Fletcher et al., 2013) and the Sicilian Strait (e.g. Rouis-Zargouni et al., 2010, 2012; Desprat et al., 2013 ; Di Rita et al., 2018), remain poorly documented.

Here, we present new results for the AM based on the multi-proxy analysis of the marine core MD04-2801 (36°30.99'N; 0°30.03'E) over the last 14 kyrs BP, with a focus on the Holocene interval. This study benefited from a detailed sedimentological description (including X-ray fluorescence-XRF and grain-size analyses, clay mineral identification and conventional stable isotopes of O and C), centennial-scale resolution reconstructions of palynological proxies (pollen grains, dinocysts and other non-pollen palynomorphs or NPP), and molecular biomarkers (alkenones and n-alkanes). Our main objectives are i) to characterize upwelling variations through dinocyst assemblages and North-Atlantic atmospheric and hydrological influences on ecosystem variability, ii) to explore dryness and moisture conditions on land in relation with river discharge, iii) to assess the non-pollen palynomorphs (NPP) fingerprint in marine sediments and their relationship with erosion and river runoff on adjacent watersheds, iv) to evaluate the first pollen- and dinocyst-based quantifications of climate and hydrological parameters, respectively, in the study area. This dataset finally contributes to improve knowledge on north to south and west to east climatic and environmental gradients across the WMB.

2. Environmental context

2.1. Geographical and geomorphological background

The marine sediment core MD04-2801 was retrieved on the AM, 24 km from the coast, on the eastern side of the Kramis deep-sea fan (Babonneau et al., 2012; Figure 1b). From a geomorphological point of view, the Algerian coast is limited to the south by the Dahra Mountains (Cretaceous schist clay substratum) that reach an altitude of 1550 m and is bordered by the Tellian Atlas chain. The study area is surrounded by Tortonian (blue marls and sandstones), Messinian (gypsum, gypsy marls, diatomites and diatomitic marls), Pliocene (marine blue marls, sandstones and limestones), and Quaternary (calcareous sandstones, sands and alluvial deposits) geological land formations (e.g. Perrodon, 1957; Meghraoui et al., 1996; Belkebir et al., 2008; Osman et al., 2021). The proximity of the AM to high relief means that its environment includes small coastal watersheds and small, fluctuating river flows (i.e. oueds). The oued Cheliff, whose mouth is located around 60 km to the west of the MD04-2801 core site (Figure 1b), is the largest oued of the region and is characterized by an average weak flow of 15 $m^3.s^{-1}$, varying from 1.5 $m^3.s^{-1}$ during the dryest episodes to 1,500 $m^3.s^{-1}$ during flash-flood events (Gautier et al., 1998). The source of the oued Kramis (Figure 1b) is located in the Saharian Atlas and flows to the sea through the Dahra Mountains, distally feeding the Kramis deep-sea fan (Babonneau et al., 2012).

Two major climate features characterize the study area: i) mild conditions under the strong influence of mid-latitude westerly atmospheric circulation over the North Atlantic (i.e. westerlies), especially during winter, and ii) dry conditions (about 3 to 5 months per year) due to the strengthened Azores High, especially during summer (Lionello et al., 2006). The meteorological station at Mostaganem (near the Cheliff mouth) reports an average annual temperature of 18.7°C (minimum of 5°C and maximum of 25°C) between 1981 and 2010. Over this period, seasonal flash floods of nearby oueds, mainly during the "humid" season (fall to spring), represent the largest part of annual precipitation (i.e. average amount of 383 mm/yr, minimum of 1 mm/month and maximum of 71 mm/month). Flash floods drive huge amounts of terrigenous sediments (i.e. organic and inorganic particles and nutrients) to coastal waters due to their high erosive capacity (e.g. Pouquet, 1967; Guizien et al., 2007; Tzoraki and Nikolaidis, 2007).

2.2. Landscape

The Mediterranean landscapes shaping the study area are characterized by an altitudinal belt type organization split into three major subdivisions (Barbero et al., 1981; Polunin and Walters, 1985; Quezel and Medail, 2003). The thermo-Mediterranean belt covers lowlands and areas up from the coast to a 1,000 m altitude and is composed of *Olea*, *Pistacia,* sclerophillous shrublands and xerophytous taxa, associated with steppe and semi-desert representative taxa (e.g. *Artemisia,* Amaranthaceae, *Ephedra*). From 1,000 to 1,500 m, the meso-Mediterranean belt is composed of the sclerophyllous oak forest (e.g. *Quercus ilex, Quercus suber, Buxus* and *Myrtus)* and the humid-temperate oak forest (dominated by deciduous *Quercus* and Ericaceae, in association with *Juniperus* and *Cupressus*). At higher altitudes, from 1500 to 2300 m, the supra-Mediterranean belt is characterized by a specific coniferous forest (i.e. North African species of *Pinus, Abies* and *Cedrus*). The oro-Mediterranean belt extends up to 2800 m in the high Atlas with a high rate of representation of *Juniperus* (open forest taxon or arborescent mattorals). Finally, the alti-Mediterranean belt (i.e. mountainous regions) is composed of scattered Chamaephytae taxa (e.g. *Erica, Romarinus* and other Lamiaceae, *Ilex* or *Artemisia*) and represents the highest vegetation belt in the area. It corresponds to the grassland belt of European mountains (Quezel and Medail, 2003).

2.3. Hydrological context

The semi-enclosed Mediterranean Sea undergoes excess evaporation over freshwater input, resulting in a deficient water balance (Béthoux, 1979, 1984). The western Mediterranean Sea is strongly influenced by the Modified Atlantic Waters (MAW) entering through the Gibraltar strait, flowing along the Spanish coast and forming two anticyclonic gyres (i.e. the Western Alboran Gyre-WAG and the Eastern Alboran Gyre-EAG; Figure 1a). The Almeria-Oran front (35 km wide; 200 m deep; Figure 1a) position and intensity depends on the degree of development of the EAG (Tintoré et al., 1988; Rohling et al, 1995; Viúdez and Tintoré, 1995; Rohling et al., 2009). The MAW follow the Almeria-Oran front, which marks a deflection along the AM, forming the Algerian Current (AC, Figure 1; Millot, 1987; Millot, 1999, Millot and Taupier-Letage, 2005). The AC undulates eastward up to 30–40 km from the coast to 3°E (Millot, 1985, 1987; Arnone and La Violette, 1986; Arnone et al., 1990; Perkins and Pistek, 1990) where North African coast irregularities generate wind-driven eddies (cf. dotted arrows in Figure 1a). These eddies are responsible for northward coastal current extensions as well as the associated offshore propagation of low-salinity surface waters (Millot, 1999; Millot and Taupier-Letage, 2005).

The AC shows a salinity gradient from the Alboran Sea (< 37 psu; Arnone and La Violette, 1986) to the east and the internal zones of the WMB (psu > 37.5). In its coherent form, the AC marks a haline density front (Arnone et al., 1990; Perkins and Pistek, 1990) responsible for vertical mixing (i.e. upwelling; Sournia, 1973; Lohrenz et al., 1988; Raimbault et al., 1993), while the Alboran Sea is characterized by a general oligotrophic regime. On the coastal side of the density front, isopycnal mixing brings nutrient-enriched waters from the nutricline to the photic zone while, on the offshore side, diapycnal mixing brings deeper nutrients to the surface (i.e. nutrient export crossing the haline front; Raimbault et al., 1993), promoting enhanced productivity (Raimbault et al., 1993; Coussin et al., 2022). Additionally, seasonal offshore winds induce coastal upwelling, probably supported by low barometric pressure cells due to solar heating (Bakun and Agostini, 2001).

Finally, the regional climate (cf. section 2.1) is responsible for weak and irregular fluvial discharge especially during the dryest season (i.e. April to September) while strong oued discharge (i.e. flash floods) occasionally occurs during autumn and winter, transporting terrigenous material and nutrients to the sea (Guizien et al., 2007; Tzoraki and Nikolaidis, 2007).

2.3. Sedimentological context

Core MD04-2801 (36°30.99'N; 00°30.03'E; 24.82 m long; 2,063 m water depth) is located about 6 km north of the Kramis Canyon, which has an east to west orientation in the lower slope (Figure 1b). The core is located at the base of the slope and is separated from the canyon by a canyon terrace. Turbidity current overflow from the canyon to the core site is currently assumed to be very low (Babonneau et al., 2012). However, a contribution of diluted mud plumes at the top of the turbidity currents could explain the high sedimentation rates in the area. Finally, a large sediment wave field develops downslope along the right side of the Kramis Canyon. These sedimentary features mark the overflow zone of turbidity currents of the Kramis and Khadra canyons on the Kramis sedimentary ridge. Core MD04-2801 is located at the top of this field and was affected by intense overflow currents in the early phase of the formation of the Kramis sedimentary ridge (Babonneau et al., 2012).

The uppermost 10 m of MD04-2801 are not affected by gravity-driven sediment instability processes (i.e. turbidity currents and resulting turbidites; Babonneau et al., 2012). From 1045 cm upward (From section VII to section I; Figure 2), sediment generally consists of hemipelagic clays. Below 1,045 cm, section VIII consists of fine-grained turbidite beds (of approximately 1 cm thick) within a silty-clay matrix representing repeated destabilization of the shelf sediments via turbiditic plumes. Silty to sandy deposits lie on the slopes of the fan with a wide dispersal of turbiditic overflows across the abyssal plain (Babonneau et al., 2012). Around the Kramis fan, a canyon levee crest, 200 m higher than the channel bottom, only releases overflow of the largest turbidity currents, resulting in interfingered turbiditic levee deposits of the Kramis system with hemipelagic sediment (Babonneau et al., 2012). The absence of turbidites in the upper sections of core MD04-2801 (above 1,045 cm, Sections I to VII; Figure 2) reflects the isolation of the core site from the turbiditic channel due to aggradation of the levees.

3. Methodology

3.1. Sediment cores and stable isotope analyses

The log of core MD04-2801 was established through visual description of the sedimentary facies (Figure 2). The physical properties of the core (i.e. P-wave velocity, magnetic susceptibility and gamma-ray attenuation density) were measured using a 'Geotek Multi Sensor Core Logger' (MSCL) with a 2-cm-step (average 30 yrs) resolution at the Ifremer Marine Geosciences laboratory (Plouzané, France). X-ray fluorescence (XRF) profiles, for the semi-quantitative chemical composition analysis of the study core, were acquired with an "Avaatech

core-scanning XRF" with a 1-cm-step (average 15 yrs) resolution (Ifremer Marine Geosciences laboratory, Plouzané, France). In sediments, the Ti element is commonly interpreted as a terrigenous-siliclastic signature while the Ca element is related to carbonate materials of detritic and/or biogenic sources (Richter et al., 2006). Based on this assumption, the XRF-Ti/Ca ratio has been commonly used on silico-clastic margins (where Ca mainly originates from biogenic carbonates) to estimate varying terrigenous inputs to the marine realm. In this study, even if geological formations on land are mainly composed of carbonates, we will use this ratio combined with other proxies to track fluvial input to the marine realm.

Grain-size analyses were first performed at high resolution on total sediments (Master thesis of Si Bachir Roza, IUEM) and, in a second step, at a lower resolution on both total and decarbonated sediments (after HCl 30% treatment) at the IUEM (*Institut Universitaire Européen de la Mer*, Plouzané, France) using a Malvern MASTERSIZER 2000. The software GRADISTAT was used to produce particle grain-size distribution and size statistics from the laser granulometer data, including median grain size (D50) as well as sediment volumetric phase percentages (i.e. clays: $0 < Ø < 10$ µm, silts: $10 < Ø < 63$ µm, and sands: $Ø > 63$ µm).

Semi-quantitative mineralogical composition of the clay fraction was measured by X-ray diffraction (XRD) at the Ifremer Marine Geosciences laboratory (Plouzané, France) with a Bruker D2 PHASER set (with a Lynxeye fast detector; Cu X-ray tube; 30 kV voltage; 10 mA intensity). After decarbonation and decantation to retain only the < 2µm fraction, the sample was deposited on oriented glass. Each sample was routinely analyzed from 2 to 30° with a resolution of 0.02° lasting 1 s, with three XRD runs: i) air-dried, ii) ethylene-glycol saturated and iii) after calcination at 490°C. The characterization of each clayey mineral followed the description of Bout-Roumazeilles et al. (1999). Semi-quantitative estimation of clay mineral abundances (%) was performed using the Macintoch MacDiff® 4.2.5 software (R. Petschick, http://www.geologie.uni-frankfurt.de/Staff/Homepages/Petschick/RainerE.html).

Finally, stable isotopes were performed on planktonic *Globigerinoides bulloides* as well as endobenthic *Globobulimina affinis* foraminifera, hand-picked in the >150 µm sediment fraction. Isotopic analyses were conducted at the "*Pôle Spectrométrie Océan*" (IUEM, University of Brest, France) on a Finnigan MAT253 equipped with a Kiel-device automated introduction line. Analytical precisions for this spectrometer are <0.05‰ for the $\delta^{18}O$ and <0.03‰ for the $\delta^{13}C$ using, respectively, the certified NBS-19 and NBS-18 standards.

Core KMDJ-23 (36°30.006'N; 0°15.422'E; 7.52 m long; 2542 m water depth) was collected close to core MD04-2801 (Figure 1b). In this study, modern palynological assemblages related to current hydrological conditions are considered thanks to the top sediments of core KMDJ-

23 with radionucleide dating that confirmed the contemporaneous deposits at the study site (Coussin et al., 2022). We compare dinocyst data (i.e. *O. centrocarpum* for the North Atlantic influence (i.e. AC strengthening) *versus L. machaerophorum* for the estuarine influence (i.e. surface stratification) or Ocen/Lmac ratio), pollen data (sum of Mediterranean and Eurosiberian forest taxa), and alkenone SST, with coeval records of the Gulf of Cadiz (core MD99-2339), the Alboran Sea (ODP site 976 and core MD95-2043), the Algerian Margin-AM (MD04-2801, this study) and the Siculo-Tunisian strait (core MD04-2797).

3.2. Palynological analyses

3.3.1. Palynological treatments and palynomorph identifications

About 1 to 2 cm^3 of sediments were sampled every 20 cm in the upper MD04-2801 core (0 to 500 cm) at about 100 yrs resolution and every 10 cm in the lower part (500 to 1042 cm) at about 150 yrs resolution. Eighty-six samples were processed using the same palynological protocol as for palynomorph extraction, allowing direct comparison between terrestrial (pollen, spores, freshwater microalgae, and other continental non-pollen palynomorphs-NPPs) and marine (dinocysts and other marine NPPs such as marine microalgae or foraminiferal linings) microfossils on the same palynological slides. The preparation technique (Geo-Ocean laboratory, IUEM, France) was performed on the <150 µm fraction following the standardized palynological protocol of de Vernal et al. (1999), slightly adapted at the EPOC laboratory (University of Bordeaux, http://www.epoc.u-bordeaux.fr/index.php?lang=fr&page=eq_paleo_pollens). It includes chemical treatments (cold HCl: 10, 25 and 50%; cold HF: 45 and 70%, to remove carbonates and silicates, respectively) and sieving through single-use 10 µm nylon mesh screens. To avoid selective dinocyst degradation during sample treatment, no oxidative agent or heavy liquid technique was applied. Microscopic identification was performed with a Zeiss (Axio Scope.A1) microscope at x630 magnification. Absolute concentrations of palynomorphs were calculated using the marker grain method (Stockmarr, 1971; de Vernal et al., 1999; Mertens et al., 2009). Accordingly, aliquot volumes of *Lycopodium* spores were added to each sample before chemical treatment to allow the calculation of palynomorph concentrations as a number of palynomorphs/cm^3 of dry sediments (i.e. these exotic spores are counted simultaneously with studied palynomorphs for each sample).

A threshold of 100 individuals (> 5% in the total assemblage) is required to identify major species (Fatela and Taborda, 2002). In this study, 88 samples were analysed, with a minimum

count of 100 dinocysts (taxonomy following Fensome et al., 1993) and 150 pollen grains except for the over-represented taxon *Pinus* (Turon, 1984; Heusser and Balsam, 1985; taxonomy following Reille, 1992). Minimal counts were not reached for two dinocyst (40-41 and 541-542 cm) and three pollen (20-21, 440-441, 441-442 cm) assemblages. Their corresponding levels were therefore excluded from the discussion. Among dinocysts, *Brigantedinium* spp. includes all round-brown cysts, *Echinidinium* spp. includes all brown cysts with typical *Echinidinium* spine-like processes not determined on a species level, and *Spiniferites* spp. includes all *Spiniferites* taxa not determined on a species level. In addition, heterotrophic dinocysts (i.e. derived from dinoflagellates with a strict heterotrophic nutrional strategy) are indirectly related to food resources, especially diatoms, as commonly shown in upwelling areas (Wall et al., 1977; Lewis et al., 1990; Marret, 1994; Biebow, 1996; Zonneveld et al., 1997, 2001; Targarona et al., 1999; Bouimetarhan et al., 2009; Penaud et al., 2016). Therefore, the sum of heterotrophic taxa was made to account for "strict" heterotrophic dinocysts. Among continental palynomorphs, "undetermined fungal spores" include all fungal spores that cannot be determined on type-code, genus or species levels. Regarding relative abundance of pollen assemblages, percentages of *Pinus* were based on the total pollen sum, while continental NPP relative abundances were calculated on a total sum that includes the pollen main sum (i.e. without *Pinus*) and the sum of spores and other continental NPPs (van Geel et al., 1972; Cugny et al., 2010; Miola, 2012).

3.3.2. Statistical analysis on palynological results

Palynological diagrams of pollen and dinocyst assemblages were performed with the Tilia software (Grimm, 1990), also defining the more parsimonious statistically homogeneous palynological zonations according to the CONNIS model (Grimm, 1987).

Taxonomical diversity indexes were calculated using the "PAST version 4.06b" software (Hammer et al., 2001), including the species richness (i.e. number of taxa per sample), the Margalef's richness index (diversity index), and the dominance index (i.e. the value "0" indicates equal presence of all taxa while the value "1" indicates the dominance of one taxon in the assemblage). In addition, multivariate analyses (Detrended Correspondence Analysis, DCA) were performed with the PAST program for semi-quantitative geochemical XRF data (cf. Data Availability section).

3.3.3. Dinocyst-inferred environmental reconstructions

Dinocyst-based sea-surface environmental quantifications were performed using R version 2.7.0 software (R Development Core Team, 2008; http://www.r-project.org/) and the Modern Analogue Technique (MAT; e.g. Guiot, 1990; Guiot and de Vernal, 2007). This method consists of selecting (based on a dissimilarity index) a limited number of analogue surface dinocyst assemblages and associated environmental values. A modern surface database is thus required. Dinocyst fossil assemblages were compared to the most recent standardized Northern Hemisphere "modern" database (n=1,968 sites; de Vernal et al., 2020), recently upgraded with new modern assemblages of the Western Mediterranean Basin (WMB; + n=23: 6 in the Gulf of Lion and 17 in the AM; Coussin et al., 2022). The dinocyst dataset includes 71 different taxa in relation with 17 modern environmental parameters (de Vernal et al., 2020). Five modern analogues were found by the MAT, which allowed to calculate environmental parameters considering an average of related parameter values, with the maximum weight attributed to the statistically closest analogue (e.g. Guiot and de Vernal, 2007). Considering the statistical threshold distance of the MAT (d_T= 1.2), analogues are considered as i) remote when the distance $d > d_T$, acceptable when $d_T/2 < d < d_T$, and good when $d < d_T/2$ (de Vernal et al., 2005). Root Mean Square Errors (RMSE) are used to discuss uncertainties in fossil quantifications, often caused by the lack of corresponding modern analogues of fossil assemblages (Guiot and de Vernal, 2007; de Vernal et al., 2020). In this study, we have estimated summer and winter sea surface temperature (SST_{winter} and SST_{summer}; RMSE of 1.2°C and 1.8°C, respectively), sea surface salinity (SSS_{winter} and SSS_{summer}; RMSE of 1.1 psu and 2.1 psu, respectively), and mean annual Primary Productivity (PP_{annual}; RMSE of 436.1 gC m^{-2} yr^{-1}).

3.3.4. Pollen-inferred climate reconstruction

Pollen reconstructions were also generated with the MAT applying the same general principles as for the dinocyst-based reconstructions. In this case, the method calculates a dissimilarity index between fossil pollen obtained on core MD04-2801 and modern pollen assemblages extracted from the database updated in Dugerdil et al. (2021). Modern climate parameters associated with the best analogues are then weighted (according to the similarity of the best four analogues) to provide values for fossil-pollen assemblages. Climate reconstructions were obtained with a leave-one-out approach. In this study, the climate variables are Mean Temperature of the Coldest Month (MTCO; RMSE of 4.7°C), Mean Temperature of the Warmest Month (MTWA; RMSE of 2.6°C), Annual Temperature (TANN; RMSE of 3.1°C),

Annual Precipitation (PANN; RMSE of 199 mm/yr), and Summer Precipitation (SUMMERPR; RMSE of 51.3 mm/summer). We also calculated a temperature seasonality index as the difference between MTWA and MTCO reconstructions using the Rioja package in R (Juggins, 2012).

3.4. Biomarker analyses

Biomarker analyses were performed at a temporal resolution of about 150 years. Lipids were extracted from 1.5 to 2 g of freeze-dried sediments using a mixture of dichloromethane/methanol (2:1 v/v). Silica gel chromatography was used to isolate alkenones and n-alkanes from the total lipid extracts. They were then analysed by gas chromatography, following Sicre et al. (1990). We used the global calibration from Conte et al. (2006) to convert the unsaturation ratio of C_{37} alkenones ($U^{k'}_{37} = C_{37:2}/(C_{37:2} + C_{37:3})$ into sea surface temperature (SST) using the following equation ($SST = -0.957 + 54.293(U^{k'}_{37}) - 52.894(U^{k'}_{37})^2 + 28.321(U^{k'}_{37})^3$).

Simultaneously, high molecular-weight terrestrial n-alkane concentrations were determined. The C_{29}, C_{31}, C_{33} and C_{35} homologues produced from higher plants were quantified. Their sum, thereafter named TERR-alkanes, was used to reflect terrestrial inputs to the studied site (Castañeda et al., 2009; Jalali et al., 2017). Vegetation types can be distinguished based on the relative homologue distribution of leaf wax n-alkanes. Deciduous trees and shrubs are thought to mainly produce n-alkanes with n-C_{27} and n-C_{29} while grasses and herbs mainly produce n-C_{31} and n-C_{33} (Vogts et al., 2009; Schäfer et al., 2016; Bliedtner et al., 2018). Average Chain Length (ACL) of n-alkanes was also calculated to produce information on water availability and compare this to vegetation-type indicators from pollen analyses (Jalali et al., 2017).

4. Results

4.1. Age model of core MD04-2801

The age model of core MD04-2801 was built by integrating 20 AMS ^{14}C dates (11 from the ARTEMIS spectrometer of the Laboratoire de mesure du Carbone 14, CEA Paris-Saclay, and nine from the ECHoMICADAS spectrometer; Table 1): 18 samples consist of monospecific planktonic foraminifera (*G. bulloides*) and two samples consist of gastropods (Table 1). All radiocarbon dates were calibrated using the CALIB 8.2 software (Stuiver and Reimer, 1993) and the IntCal20 calibration curve (Reimer et al., 2020), first considering a reservoir age of -400 years (Siani et al., 2000). To establish the age model (Figure 2), the rbacon package (Blaauw and Christen, 2011) was used under R (version 4.1.0; R Development Core Team, 2021; http://www.r-project.org/). Two dates were discarded at 931 cm (large analytical error of 270 years; Table 1) and 31 cm (considered as an outlier regarding the first 4 m of the core; yellow diamonds in Figure 2).

It is worth noting that the stratigraphy of the upper section is suspected to be influenced by a core disturbance by piston effect. This is supported by decreasing values of the sediment density from 250 cm upward, with very low Vp values between 140 and 90 cm (Figure 2). For this reason, the age model was calculated independently for the upper (431 to 0 cm) and lower (1,031 to 431 cm) parts of the studied core, and then brought together (Figure 2). Considering the density as the artefact clue, abrupt change in sedimentation rates at 431 cm (Figure 2) is suggested while the artefact in the sampling appears from 250 cm upward. Furthermore, laminations are visible below 400 cm but less clear above this level (especially from 250 cm upward), where sediments appear to be more homogenous (Figure 2). At the MD04-2801 core site, situated beyond the crest of a turbidite channel-levee system, the expected sedimentary record could be composed of hemipelagites and fine-grained turbidites from turbidity currents overspilling the levee. These high accumulation rates (i.e. around 150 cm/kyr on the 431–0 cm section; Figure 2) cannot therefore be expected to reflect gravity-driven sedimentary processes. In light of these features, a coring artefact in MD04-2801 is probable (Figure 2). Overall, a robust chronology is assumed from 431 cm to the base of the core with average sedimentation rates of about 40 cm/kyr (stable Vp and density values with a two-step density trend at around 870 cm; Figure 2), while a less robust chronology is assumed from 431 cm upward with a two-step trend in physical sediment properties. From 431 to 250 cm, well-layered sediments, as observed in the basal section, correspond to a strong increase in density values and still stable Vp values and may be related to an acceleration in sedimentation rates (280 cm/kyr; Figure 2).

From 250 cm upward, the creep of sediments appears very likely affected by the piston effect (strong decrease in density values at 250 cm and unexpected low Vp values between 120 and 70 cm). According to the age model (Figure 2), the base of the studied core is dated at 14 cal ka BP.

4.2. Sedimentological signals

The core MD04-2801 mainly consists of homogeneous silty sediments that can be separated by six limits (a to f in Figure 3) based on the trends in graphs of sedimentological parameters. KMDJ23 is a core very close to the MD04-2801 coring site whose top sample (water-sediment interface) was analyzed and presented in Coussin et al., 2022 (https://doi-org.scd-proxy.univ-brest.fr/10.1016/j.marmicro.2022.102157). It constitutes a modern assemblage useful as a reference point.

4.2.1. X-ray Fluoresence

In order to investigate the co-occurrences of major elements of the XRF dataset, we performed a Detrended Component Analysis (DCA) on selected elements (Ca, Si, Al, K, S, Ti, Fe, Mn, Sr; cf. Data in brief). In the study area, the silico-clastic detrital signature is well expressed by Ti and Fe, while Si and Al are the main chemical components of alluminosilicates. Ti, FE, Si and Al show similar trends suggesting that these elements potentially relate to the clayey fraction formed by the chemical alteration of soils. Conversely, common patterns of Sr and Ca point to biomineralized and/or detrital carbonates. The DCA statistical analysis (Data in Brief) led to the most relevant XRF ratios for the following discussion. Given the difficulty in deconvoluting terrigenous and marine sources in the Ca-XRF signature, we considered both Ca/Al-XRF (mixed detrital-biogenic signature, Figure 3a) and Ti/Al-XRF (detrital signature; Figure 3b) for the paleoenvironmental interpretation conducted in the AM sediments. Both ratios generally show similar fluctuations in temporal variations over time and amplitudes, suggesting a stronger detrital source in the Ca-XRF signature except for two intervals characterized by high Ca/Al-XRF and low Ti/Al-XRF ratios from the base of the core to 910 cm (limit “b”) and between 575 and 485 cm (limits d and e). The Ti/Ca-XRF ratio is considered as primarily detrital and linked to silico-clastic *versus* carbonate sources to the AM.

4.2.2. Magnetic Susceptibility and grain size

The Magnetic Susceptibility (MS) signal shows distinct fluctuations between 3.8 and 17.5 SI. Three main phases are identifed with average values of 9.2 SI from the base to 910 cm (limit

"b"), of 14.3 SI between 910 and 370 cm (limit "f") and of 11.6 SI from 370 cm upward (Figure 3c).

In addition, according to the high-resolution grain-size data of total sediments (Data In Brief), the 4–63 µm fraction largely dominates (silt, average of 66%), followed by the fraction <4 µm (clay, average of 23%) and the fraction >63 µm (sand, average of 11%). More specifically, from the base of the sequence to 910 cm (limit "b"), the high proportion of the >63 µm fraction (Figure 3d) is associated with low amounts of ferro-magnetic minerals (low MS values; Figure 3c), high Ca/Al values *versus* low Ti/Al (Figure 3 a,b), and extremely low median (D50) grain size of $CaCO_3$-free sediments *versus* high D50 grain size of total sediments (Figure 3d). This may indicate that coarser sediments are mainly inherited from the erosion of carbonate formations, with little advection of small-sized silico-clastic and ferro-magnetic sediments.

Then, from 910 cm (limit "b") to 370 cm (limit "f"), higher MS values (Figure 3c) combined with D50 values of $CaCO_3$-free sediments higher than D50 values of total sediments (Figure 3d) indicate increasing advection of silico-clastic and ferro-magnetic silto-clayey material with a lower proportion of detritic carbonate particles. Across limits "b" to "f", the coarsest detrital particles of the mix (silicates and carbonates) are particularly evident in the 740–575 cm interval (between limits "c" and "d" or interval "c-d"), and correspond to two remarkable peaks of sandy sediments at 580 and 600 cms (Data in Brief). It is worth noting that the 575 to 485 cm interval ("d-e") coincides with the second interval of high Ca/Al-XRF values (as in zone "a-b") and lower D50 grain-size values (Figure 3d), with coarser sediments corresponding to silty rather than sandy particles as in the interval "a-b".

From 370 cm (limit "f") to 250 cm, MS values as well as grain-size properties point to finer silto-clayey sediments (Figure 3c). Finally, from 250 cm upward, wide ranges of coarse *versus* fine-sediment fluctuations (Data in Brief), associated with low D50 grain-size values (Figure 3d), can be reconciled by invoking a small proportion of very coarse sediments which would bias the mean but hardly alter the particle-size medians. A grey band in Figure 3 highlights this section, suspected to be affected by core disturbance through piston effect.

4.2.3. Clay mineral composition

Clay mineral averages are about 8% of Illite-Smectite (Interstratified), 18% of Chlorite, 32% of Kaolinite and 43% of Illite (Data In Brief). Clay results are represented as anomalies relative to the mean of each dataset (Data In Brief). Due to high sedimentation rates (around 50 cm/kyr; Figure 2), palygorskite was not significantly detected. The boxes in Figure 3g highlight the Majorly different clay mineral phases (relative to their mean values). The two intervals of

enhanced Ca/Al-XRF values ("a-b" and "d-e") are also characterized by the highest interstratified values and lowest kaolinite percentages. Conversely, kaolinite percentages increase during intervals of both increasing proportions of clays and finer grain-size sediments ("b-c" and "e"-250cm). This suggests that increasing kaolinite values could evidence strengthened chemical alteration on land. We consequently use the Kaolinite/Illite ratio as a proxy of chemical alteration throughout the sequence.

4.3. Stable isotope signals

4.3.1. Carbon isotopes in foraminifera

The $\delta^{13}C$ values of endobenthic *Globobulimina affinis* and planktonic *Globigerinoides bulloides* foraminifera range between -0.9 and -2.1‰ (mean of -1.6‰) and between -0.6 and -2‰ (mean of -1.1‰), respectively (Figure 3e). Planktonic and endobenthic $\delta^{13}C$ signals show similar values until 740 cm (limit "c"), but exhibit a significant offset (average of 0.7 ‰) after 575 cm (limit "d").

Heavier planktonic $\delta^{13}C$ values observed during the interval "a-b", as well as after 575 cm (limit "d") reveal strong primary productivity. Conversely, the $\delta^{13}C$ of endobenthic foraminifera generally reflects the $\delta^{13}C$ of pore waters, which depends on the export flux of organic matter and availability of dissolved oxygen in bottom waters (e.g. McCorkle et al., 1990; Mackensen & Licari, 2003; Fontanier et al., 2006). Lighter benthic $\delta^{13}C$ values after limit "b" may be indicative of remineralization of enhanced organic matter in bottom sediments.

4.3.2. Oxygen isotopes

Endobenthic (*G. affinis*) and planktonic (*G. bulloides*) $\delta^{18}O$ values range between 2.1 and 4 ‰ (mean of 2.6 ‰) and between 0.4 and 2.2 ‰ (mean of 0.8 ‰), respectively, and show similar patterns throughout the sequence (Figure 3f). Heavier $\delta^{18}O$ values (colder sea surface temperatures) in the interval "a-b" are reflected by values of 1.9 and 3.8 ‰ for planktonic and endobenthic taxa, respectively. Lighter mean $\delta^{18}O$ values after limit "b" are stable around 0.6 ‰ (standard deviation of 0.2 ‰) and 2.4 ‰ (standard deviation of 0.1 ‰) for planktonic and endobenthic taxa, respectively. However, wider ranges of planktonic $\delta^{18}O$ isotope value variations, with slightly lower values since interval "b-d", may be indicative of either decreasing salinities and/or increasing temperatures.

4.4. Palynological analyses

4.4.1. Dinoflagellate cysts

- *Diversity and concentrations*

Thirty-nine different dinocyst taxa were identified over the whole sequence, with a mean species richness of 18 different taxa per slide (Figure 4a). Species richness is lower than average from the base of the sequence to limit "a" (1,025 cm), in the "b-d" interval (910–575cm), and after limit "e". Conversely, species richness is higher than average in "a-b" (1,025–910 cm) and "d-e" (575–485 cm) intervals. Both intervals are also characterized by low kaolinite percentages and high Ca/Al-XRF values, as well as heavy planktonic $\delta^{13}C$ values.

The dinocyst dominance index (Figure 4a) is systematically explained by the major taxa *Brigantedinium*. The dinocyst diversity (Figure 4a), as reflected by the Margalef index (similar to species richness), shows opposite trends compared to *Brigantedinium* spp.; the lowest diversity being synchronous with high *Brigantedinium* spp. percentages.

Total dinocyst concentrations, mainly explained by *Brigantedinium* spp. occurrences, range between 450 and 29,000 cysts/cm^3, with mean values of around 3,300 cysts/cm^3 (Figure 4a). Dinocyst concentrations show higher values during intervals "a-b" (1,025 to 910 cm) and "d-e" (575 to 485 cm), both previously described by a stronger diversity. We thus plotted the concentrations of all dinocysts without *Brigantedinium* spp. against the concentrations of *Brigantedinium* spp. alone in order to evaluate the respective contribution of these heterotrophic taxa with regards to the rest of the dinocyst community (Figure 4a). Up to limit "b", other dinocysts are higher than *Brigantedinium* spp. (around 10,000 *versus* 2,000 cysts/cm^3). They follow similar patterns between limits "b" and "e" (around 1,500 cysts/cm^3) and, after limit "e", all other dinocyst concentrations are slightly lower than *Brigantedinium* spp. (1,000 vs. 1,500 cysts/cm^3). Dinocyst concentrations show lower values but similar evolution compared to pollen grain concentrations throughout the sequence, except for similar concentrations obtained from 1040 cm to limit "b" and during the interval "d-e" (575–485 cm).

- *Dinocyst assemblages and dinocyst zones*

Dinocyst assemblages are dominated by eight autotrophic taxa: *Nematosphaeropsis labyrinthus, Impagidinium aculeatum, Spiniferites mirabilis, Operculodinium centrocarpum, Spiniferites bentorii, Spiniferites membranaceus,* cysts of *Pentapharsodinium dalei, Lingulodinium machaerophorum* and seven heterotrophic taxa including *Echinidinium* spp., *Selenopemphix quanta,* cysts of *Protoperidinium nudum, Selenopemphix nephroides,*

Lejeunecysta spp. (grouping of *L. oliva* and *L. sabrina*), *Trinovantedinium* spp. and *Brigantedinium* spp. (Figure 5a).

The dinocyst assemblages led us to consider four main limits, thus five palynozones (MD04-1 to MD04-5; Fig. 5). These boundaries/zones are based on the CONNISS cluster analysis performed on dinocyst assemblages (threshold used is 11; Figure 5a). These four limits also correspond to four sedimentological limits (a-b-d-e; Figs. 3 and 4). Zone MD04-1, from the base of the sequence to limit "a", is characterized by the dominance of *Brigantedinium* spp., *S. mirabilis* and *O. centrocarpum*. The second zone MD04-2 (interval "a-b") is marked by increasing values of *N. labyrinthus* reaching 20 to 40%, associated with the increase in *B. tepikiense, S. lazus* and *O. centrocarpum.* Zone MD04-03 (interval "b-d") is characterized by a high plateau of *Brigantedinium* spp. up to ca. 40%, associated with the increase in *I. aculeatum* (up to 15 %) and *S. mirabilis*, especially in the interval "c-d", and a progressive decrease in *O. centrocarpum* percentages. Zone MD04-4 (interval "d-e") shows a sharp drop in *Brigantedinium* spp. percentages reaching 20%, while *S. mirabilis* increases to 30%. Finally, zone MD04-5 (from limit "e" onward) is characterized by the highest values of *Brigantedinium* spp. (about half of the total assemblage) associated with *S. mirabilis* (around 15%). A full description of main dinocyst results is available in Data in Brief.

4.4.2. Pollen grains

- *Diversity and concentrations*

Seventy-one different pollen taxa were identified for the whole sequence, with a mean species richness of 28 different taxa per slide (Figure 4b). Species richness ranges between 18 and 29 taxa per slide with lower values between limits "c" and "f "(740 to 370 cm) which also correspond to the strongest representation of forest taxa (cf. percentages of total trees and total trees with *Pinus*; Figure 4b). In contrast, increased diversity coincides with the diversification of herbaceous plants. Mean total pollen concentrations are approximately of 6200 grains/cm^3 (ranging between 1300 and 25,000 grains/cm^3); the highest values are in intervals "a-b" (1,025 to 910 cm) and "d-e" (575 to 485 cm), as for dinocysts, and above 250 cm (removed from the discussion).

Pinus concentrations follow the same trend as total pollen concentrations that are mainly driven by trees (especially *Quercus*). Strong pollen production, enhanced river transport, and finer grain-sized sediments, are crucial factors contributing to increase pollen-grain concentrations. However, the strong link between pollen (terrestrial compartment) and dinocyst (marine realm)

concentrations point to a common mechanism of organic matter export to the AM and sedimentation processes.

- *Pollen and Non-Pollen Palynomorph (NPP) assemblages and pollen zones*

The zones defined on the basis of dinocyst assemblages have also been used for pollen assemblages to facilitate land-sea comparison (Figure 5b). Zone MD04-1 is characterized by the dominance of herbaceous pollen taxa, mainly Cichorioideae and Poaceae. Zone MD04-2 is marked by the strong increase in the altitudinal taxa *Cedrus* (reaching maximum percentages above 40% at 1001 and 961 cm), associated with semi-desert, steppic pollen taxa (i.e. *Ephedra* and *Artemisia*) and coastal-steppic taxa (i.e. Amaranthaceae). Zone MD04-3 is characterized by the progressive increase in arboreal taxa (especially *Quercus ilex*), associated with strong occurrences of herbaceous taxa (Cichorioideae and Poaceae) until 740 cm (limit "c"). In zone MD04-3, limit "c" corresponds to the onset of the strongest forest representation, largely represented by *Quercus*, associated with Cupressaceae, as well as Mediterranean forest (*Olea, Pistacia*) and open vegetation (i.e. Cichorioideae and Poaceae) taxa. Interestingly, from limit "c", freshwater algae occurrences also increase. Zone MD04-3 is also marked by increasing abundance of *Glomus* spores and Ascospores. Zone MD04-4 shows a strong representation of arboreal taxa (up to 40%) associated with a slight decrease in open-vegetation taxa (Cichorioideae, Poaceae). Coastal-steppic taxa (Amaranthaceae), with slight increases in *Ephedra* and *Artemisia*, also correspond to decreasing occurrences of *Glomus* spores. Finally, zone MD04-5 is characterized by the progressive decrease in arboreal taxa (especially *Quercus*) favoring the synchronous increase in open-vegetation taxa (Cichorioideae, Asteroideae, Poaceae). Additionally, percentages of semi-desert taxa (*Ephedra* and *Artemisia*) somewhat increase with those of *Olea*, and *Glomus* spore occurrences progressively increase. Modern climate-landscape relationships in Eurasia and northern Africa (Woodwards, 1987; Peyron et al., 1998) will be considered for pollen interpretation. A full description of main pollen results is available in Data in Brief.

4.4. Palynological quantification

For dinocyst-inferred sea-surface reconstructions, the maximum number of selected analogues is five (Figure 4) Also, a threshold of 1.35 is adopted by the MAT (Modern Analogue Technique) to exclude too dissimilar assemblages. In this study, Dmin varies around an average value of 0.87: no analogue was selected for six levels (440, 664, 800, 948, 992, 1000 cm), only one analogue for four levels (60, 746, 860, 932 cm), two analogues for one level (976 cm), three

analogues for three levels (976 cm), four analogues for nine levels (340, 532, 696, 760, 872, 880, 920, 1026, 1040 cm) and five analogues for the 63 other levels, testifying for statistical robustness of the reconstruction for about three quarters of the analysed samples.

For pollen-inferred climate reconstructions, the number of selected analogues is always four. Appropriate analogues are selected through cross-validation based on the leave-one-out approach. Stable Dmin values are about 0.39 from 1,040 cm to limit "e" and about 0.47 from limit "e" to the top of the sequence, testifying to the robustness of reconstructed climatic parameters.

Considering hydrological (cf. dinocyst-based quantifications) and climate (cf. pollen-based quantifications) parameters, SST and SSS are discussed in parallel with annual precipitation and temperature seasonality. The exhaustive dataset of reconstructed environmental parameters is available in Data in Brief.

4.5. Molecular biomarkers

Concentrations of C_{37} alkenones, plotted as the sum of $C_{37:2} + C_{37:3}$, range from 18 to 328.5 $ng.g^{-1}$, with a mean value of about 75.6 $ng.g^{-1}$ (Figure 4a). The $\sum C_{37}$ follows the same trend as that of palynomorph (dinocyst and pollen) concentrations along the sequence, with higher values in the oldest interval "a-b" (1,025 to 910 cm), highlighting the common pattern in organic matter export and preservation through both biomarker and palynological approaches.

Concentrations of TERR-alkanes range between 354 and 1,071 $ng.g^{-1}$, with a mean value of 643 $ng.g^{-1}$(Figure 4b). Up to limit "b" (910 cm), they decrease to the lowest values of the record (379 $ng.g^{-1}$). From limits "b" to "d", TERR-alkane concentrations are generally higher and highly variable with above average values. They broadly decrease during intervals "d" to "f" and increase again until 370 cm before decreasing up to the top of the studied core.

Finally, the ACL (Average Chain Length; Figure 4b) calculated from the n-alkane distribution shows increasing values from interval "a" to "d", suggesting a gradual dryness (expressed by high ACL values), followed by stable values up to limit "f", followed by decreasing values close to the mean of the dataset (30,1) up to the top of the studied sequence. Mean values of the ACL are generally consistent with our palynological data underlying a strong representation of open vegetation along the sequence.

5. Discussion

5.1. Palynomorph preservation and the signature of *Brigantedinium* spp.

Fine-grained (silto-clayey) sediments and high sedimentation rates (ca. 50 cm/kyr) recorded with core MD04-2801 may have favored conditions for the preservation of fossilized palynomorphs (dinocysts and pollen grains). A recent study of the modern distribution of pollen grains in the WMB suggested that modern pollen assemblages in our study area are representative of the adjacent vegetation (e.g. *Quercus ilex*, Amaranthaceae and Cichorioideae; Coussin et al., 2022). However, previous studies have investigated taxa sensibilities to oxidation effects (e.g. Havinga, 1967, 1971; Lebreton, 2009). It has for exemple been shown that *Quercus* and Cichorioideae pollen grains are not very sensitive to degradation and could be overrepresented in pollen assemblages at the expense of other taxa. The intact aspect of all pollen grains throughout the sequence leads us to hypothesize that pollen are mainly from the coastal Algerian catchments and that over-representation of the main taxa is unlikely. Regarding dinocyst taxa, *Brigantedinium* spp. are dominant and show large fluctuations (ca. 10 to 80 %; Figure 4a, 6j) throughout core MD04-2801. *Brigantedinium* spp. are often interpreted as witnessing upwelling regimes (e.g. Marret, 1994; Zonneveld et al., 1997, 2001; Bouimetarhan et al., 2009; Penaud et al., 2016; Coussin et al., 2022). Moreover, modern occurrences of *Brigantedinium* spp. in surface sediments of the western Mediterranean Basin (around 20%; Coussin et al., 2022) in association with *T. applanatum*, *Lejeunecysta* spp., *Echinidinium* spp., *S. nephroides* and grouped *Selenopemphix quanta* and *Protoperidinium nudum*, also allowed to assign these taxa to productive surface waters and were used to highlight the major haline-upwelling front associated with the AC, itself depending on the vigour of the Alboran gyres (Coussin et al., 2022). *Brigantedinium* spp. peaking values of ca. 80% over the Holocene (Figure 6i) were never reached in western Mediterranean modern surface sediments, even along the AC (Coussin et al., 2022). Since *Brigantedinium* spp., as well as *Echinidinium* spp., are well-known for their strongest sensitivity to oxic conditions (e.g. Zonneveld et al., 1997; Kodrans-Nsiah et al., 2008; Bogus et al., 2014), their percentages must be interpreted carefully as direct tracers of primary productivity. Indeed, it has been shown that their occurrences in sediments decrease logarithmically with increasing bottom water oxygen content (Zonneveld et al., 2001, 2007, 2008). Our reconstructions therefore raise questions about potential taphonomic biases that may have affected dinocyst assemblages.

The MD04-2801 core retrieved at a water depth of 2,063 m is located in the water depth range of the Western Mediterranean Deep Waters (WMDW). The WMDW, as well as Ligurian

Intermediate Waters (LIW), contribute to the Mediterranean Outflow Water (MOW) export at the Gibraltar Strait (Stommel et al., 1973; Lionello et al., 2006) which varied through time (e.g. Voelker et al., 2006; Toucanne et al., 2007; Peliz et al., 2009; Rogerson et al., 2010; Bahr et al., 2014, 2015; Voelker and Aflidason, 2015; Hernández-Molina et al., 2014). Stronger LIW during cold climate events (Toucanne et al., 2012) such as the Younger Dryas (YD), implying a stronger WMB ventilation, is also supported by Alboran Sea records (Mc Culloc'h et al., 2010). In contrast, warmer Holocene conditions, and especially the Sapropel 1 event (10.8 ± 0.4 to 6.1 ± 0.5 ka BP) in the Eastern Mediterranean Basin (e.g. Kallel et al., 1997; Bar-Matthews et al., 2000, 2003; Mercone et al., 2000; Rohling et al., 2002; Tachikawa et al., 2015), are characterized by a weakened/cessation of the LIW formation (e.g. Toucanne et al., 2012). This shift from well-ventilated bottom waters during the YD to less-ventilated ones during the Holocene optimum (ca. 9.5-6.5 ka BP) may respectively correspond to low (around 20% such as today) or high (> 40%) percentages of *Brigantedinium* spp. (Figure 6i). There is therefore a risk that *Brigantedinium* spp. relative abundances may be modulated by oxygenation conditions despite the high sedimentation rates recorded at our studied site. In this context, Zonneveld et al. (2007) suggested to use absolute concentrations of phototrophic rather than heterotrophic taxa (or total dinocyst) ones, combined with dinocyst diversity (or species richness), to better assess productivity conditions. In the following discussion, these recommendations are considered to limit potential biases due to diagenesis or ventilation when discussion dinocyst assemblage reconstructions.

5.2. From the Bölling-Alleröd to the Younger Dryas

5.2.1. Hydrological conditions

Alkenone SSTs show a strong cooling from the Bölling-Alleröd (B/A: zone MD04-1) to the Younger Dryas (YD: zone MD04-2 or "a-b"; Figure 6) featuring the lowest SST values (i.e. 15.5°C; 4.1°C below modern annual SSTs), consistent with the heaviest planktonic $\delta^{18}O$ values greater than 2‰ (Figure 6a,b). These low temperatures corresponds to the lowest reconstructed seasonality values (Figure 7h). This cold SST trend is synchronously observed in both the WMB sequences (Figure 8d,h,k,n,q). During the YD, cool-water dinocyst taxa (*N. labyrinthus*, *B. tepikiense* and *S. lazus* ; Figure 6c) dominating today polar to subpolar environments (Rochon et al., 1999; Van Nieuwenhove et al., 2020) show maximum percentages, while dinocyst-derived SSTs are not able to provide modern analogues representative of the environmental conditions of this cold climate event (Figure 6b). Indeed, all selected analogues

had statistical distances higher than the accepted threshold (cf. Data in Brief). SSTs lower by 3.5 and 8.5°C with respect to present-day winter conditions were reconstructed using foraminifera and dinocysts in SW Portugal and Cadiz-NW Morocco, respectively (Penaud et al., 2011). At these northeastern Atlantic subtropical sites, the same YD assemblages (*N. labyrinthus*, *B. tepikiense* and *S. lazus*) were observed with slight differences in percentages: *B. tepikiense* hardly occurred in the Gulf of Cadiz and further south, while *S. lazus* was not found off Portugal (Penaud et al., 2011). These observations support the mixed northern and subtropical North Atlantic influences in the AM. Also, as observed in the Alboran Sea (Turon and Londeix, 1988), *N. labyrinthus*, a stratigraphical marker of the YD, testifies of the southward shift of the bioclimatic belts during this cold event of the last deglaciation. In the AM, percentages around or slightly higher than 30% are closer to those reconstructed off the Iberian margin (slightly higher than 20%) than in NW Morocco (about 5%), and point to an enhanced advection of cold Atlantic waters in the WMB. In addition, *O. centrocarpum* (i.e. North Atlantic taxon) shows four-time stronger representation than *L. machaerophorum* estuarine taxon, suggesting the prevailing oceanic influence in the AM and associated low fluvial input (Figure 5a). This is supported by the higher values of Ocen/Lmac dinocyst ratio for all the compared WMB sites (Fig. 8)

Heavy planktonic $\delta^{13}C$ values (Figure 6g) and higher concentrations of alkenones (Figure 4a) and phototrophic dinocyst concentrations (Figure 6f) as well as a strong dinocyst diversity (Figure 4a) suggest enhanced primary productivity, despite lower percentages of *Brigantedinium* spp. (Figure 6i) that may result from a lower preservation of heterotrophic cysts under stronger bottom-water ventilation (cf. section 5.1). More productive conditions may be attributed to a stronger vigour of the AC resulting from the strengthening of the Alboran gyres during the YD (Combourieu-Nebout et al., 1999; Barcena et al., 2001; Penaud et al., 2011; Rouis-Zargouni et al., 2012; Ausín et al., 2015). This finding can also be explained by enhanced vertical mixing triggered by stronger winds replenishing surface waters with deep water nutrients.

5.2.2. Climate and continental context

Enhanced YD productivity could result from fertilization of the photic zone by Saharan dust deposition (Moreno et al., 2002; Bout-Roumazeilles et al., 2007; Jimenez-Espejo et al., 2008; Rodrigo-Gamiz et al., 2011; Bout-Roumazeilles et al., 2013). Unfortunately, the clayey fraction of core MD04-2801 only represents ca. 20% of the sediment lithology. The high sedimentation rates (ca. 50 cm/kyr), mainly characterized by silts, do not allow characterizing aeolian-

743 transported clayey minerals such as the typical palygorskite signature which is drowned in other
744 clayey minerals amount signals.
745 During the YD, the strong representation of semi-arid (*Artemisia, Ephedra*) and steppic-coastal
746 (Amaranthaceae) taxa, and the weak representation of Mediterranean forest taxa indicate
747 extremely dry conditions characterized by an open and steppic landscape (Figure 7g). This open
748 landscape is expressed by the lowest forest taxa representation in the WMB sequences (Figure
749 8g,j,m,p). Previous studies in the Western Mediterranean Sea already showed this cold-dry
750 event as characterized by a first dry phase followed by a more humid period (e.g. Combourieu
751 Nebout et al., 1998, 2002; Turon et al., 2003; Naughton et al., 2007; Kotthoff et al., 2008;
752 Fletcher and Sanchez-Goñi, 2008; Dormoy et al., 2009; Combourieu-Nebout et al., 2009;
753 Desprat et al., 2013). This bipartite structure is not obvious at the resolution of our study, except
754 for a slight decreasing trend of *Artemisia* from the start to the end of the YD (Figure 5b).
755 Additionally, increasing ACL values from 29.8 to 30.2 (Figure 4b) are consistent with a higher
756 plant adaptation to water stress.
757 The YD sedimentary facies of core MD04-2801 highlights coarse carbonate sediments with
758 minor advection of small-sized silico-clastic and ferro-magnetic sediments (Figure 3d).
759 Consequently, arid conditions during the YD, as revealed by pollen grains, may have favored
760 erosion of sedimentary formations onland and aeolian transport of carbonate particles amplified
761 by strengthened atmospheric circulation. Indeed, low Kaolinite values (cf. Data in Brief)
762 suggest reduced chemical alteration, while low concentrations of *Glomus* spores evidence weak
763 runoff due to low precipitations (Figure 7c). Sporadic but intense erosive runoff events may be
764 linked to peaks of reworked cysts originating from the alteration of Tertiary carbonate
765 formations (Figure 5a). Indeed, Algerian oued discharge intensifies during intense rainfalls
766 events responsible for flash floods with strong erosive effects. However, the scarce occurrences
767 of continental NPPs and generally low concentrations of reworked dinocysts rather attest low
768 alteration and low fluvial delivery to the AM.
769 Finally, unusual occurrences of *Cedrus* (about 20 %, peaking at 40 % ; Figure 7j) are recorded.
770 Considering the modern distribution of *Cedrus atlantica* in Northern Africa (Bell et al., 2019),
771 in the highest altitudinal vegetation belts (Ben Tiba and Reille, 1982; Stambouli-Essassi et al.,
772 2007), and the modern distribution of *Cedrus* percentages (around 0.5%) in KMDJ-23 core
773 (Coussin et al., 2022), we suggest that a wider altitudinal *Cedrus-Pinus* forest developed in the
774 high reliefs of the Tell Atlas. Even if stronger aeolian transport of coniferous pollen grains
775 better dispersed by winds than other pollen grains is possible under stronger atmospheric
776 circulation, synchronous peaks of *Cedrus* and reworked cyst concentrations (Figure 4), rather

suggest remaining mild conditions in altitudinal zones enhancing fluvial transport (i.e. strong seasonal erosive runoff) of *Cedrus,* even under the prevailing arid conditions of the YD.

5.3. The Early Holocene (11.7–8.2 ka BP)

5.3.1. Delayed Mediterranean forest expansion

The Early Holocene is characterized by a strong decrease of the semi-arid and coastal-steppic vegetation (Figure 7g), replaced by typical mattorals (xerophytous open vegetation) mainly represented by Cichorioideae (Figure 5b). At the same time, the altitudinal forest represented by *Cedrus* is no longer recorded along the Holocene with high percentages (i.e. values close to modern ones; Figure 7j), due to reduced extent of these altitudinal vegetation belts in the Atlas Mountains in a context of increasing temperatures allowing other taxa to colonise altitudinal belts. Previous studies also discussed the limited altitudinal area where *Cedrus* retracted at the YD-Holocene transition, while warmer Holocene conditions favors the evergreen *Quercus* forest expansion (Marret and Turon, 1994; Cheddadi et al., 1998, 2009; Zielhofer et al., 2017). Until 8 ka BP, the progressive increase of Mediterranean forest taxa, combined with the persistent signature of the open vegetation (e.g. Cichorioideae, Poaceae; Figure 7 f,g), suggest a progressive increase of moisture, which is a critical limiting factor for the forest expansion in the southern Mediterranean area (Quezel, 1999). Increasing moisture is also supported by sedimentological, bioindicator, and biochemical runoff tracers (i.e. higher magnetic susceptibility (Figure 7e) and Ti/Ca-XRF values (Figure 6h), higher concentrations of *Glomus* spores (Figure 7c) and of pre-quaternary cysts (Figure 4a), higher TERR-alkane fluxes (Figure 7d)). In the AM, *Quercus* maximal values thus appear delayed, while Mediterranean mattorals (mainly represented by Cichorioideae, Poaceae and Asteraceae) associated with typical sclerophytous trees (*Olea* and *Pistacia*), are still observed.

The delayed expansion of forest appears consistent with current Mediterranean observations suggesting that, following moisture deficiency, three millennia are necessary for a full Mediterranen forest recovery (e.g. Combourieu-Nebout et al., 1998, 2002; Allen et al., 2002;; Turon et al., 2003; Naughton et al., 2006; Fletcher and Sanchez-Goñi, 2008; Jalut et al., 2009; Tzedakis, 2007; Fletcher et al., 2010; Zielhofer et al., 2017). The Early Holocene corresponds to the highest values of boreal summer insolation (Berger and Loutre, 1991; Figure 8b), responsible for high summer temperatures that may have enhanced summer Mediterranean droughts, therefore slowing down the development of trees, especially evident in the more sensitive eastern part of the basin (Figure 8m,p). Previous studies conducted in northwestern

Africa also discussed the maximal forest development at around 8.5 ka BP (Ballouche, 1986; Brun 1989; Lamb et al., 1989), consistently with the maximal values reached at the end of the Early Holocene in our study core (ca. 8 ka BP). Climate quantifications also suggest relatively low precipitation before 8.5 ka BP while the temperature seasonality indicates a strong thermal amplitude explained by high summer temperatures (Figure 7h). The Alboran Sea and by extension the AM are extremely sensitive to the Atlantic moisture through the influence of westerlies (i.e. for Mediterranean cyclogenesis). From 11.7 to 10 ka BP, the extended dry period post-YD has also been reported across the SW and NE Mediterranean basin (Dormoy et al., 2009) and is probably linked to a still weak influence of westerly cyclones (Kotthoff et al., 2008). Indeed, the North Atlantic storm tracks may have been maintained in a southern position under the influence of the Fennoscandian Ice Sheet still persistent until 9 ka BP (Magny et al., 2003). There, the forest expansion is directly in phase with the climate change of northern Atlantic latitudes (cf. NGRIP oxygen isotopes *versus* Alboran Sea forest signal in Figure 8a,g,j), in agreement with numeric simulations (Carlson et al., 2008). The Atlantic influence, and associated moisture transport, follows a decreasing gradient from west to east (Figure 8h,j,m,p) between the Alboran Sea to Algeria, whatever the climate interval considered over the last 14 kyrs.

5.3.2. Warmer oligotrophic conditions

In parallel with the Mediterranean forest expansion (Combourieu-Nebout et al., 1998, 1999, 2002, 2009), alkenone, dinocyst and planktonic $\delta^{18}O$ data (Figure 6a,b,c) point to a strong increase of SSTs at the start of the Holocene, with a 4.5°C increase of alkenone-based annual SST (i.e. from 16°C during the YD to ca. 20.5°C during the Holocene). It is worth noting that alkenone-based SSTs exhibit mean annual values consistent with the dinocyst-based SST seasonal variability range (Figure 6b). Furthermore, both alkenone- and dinocyst-derived SST, as well as percentages of cold water dinocyst taxa, point to slightly cooler SST conditions during the Early Holocene regarding the following conditions of the Middle Holocene. The warmest conditions are therefore not reached yet during the Early Holocene, and the prevalence of runoff signatures (significant peaks of *Glomus* and pre-Quaternary cysts; Figure 4a, 7a) may result from increasing moisture combined with a still high erodability of soils in a continental context of persistent opened landscape.

The Holocene transition is also characterized by a pronounced drop of dinocyst and alkenone C_{37} concentrations (Figure 4a), as well as lighter planktonic $\delta^{13}C$ values (Figure 7f), likely

accounting for less productive conditions. Interestingly, heterotrophic cyst percentages (Figure 7j) increase with a plateau of high values (about 50 %) persistent until 6.5 ka BP. However, the Early Holocene also corresponds to the maximum of the boreal summer insolation and the related northward migration of the intertropical convergence zone. This configuration drives the formation of Sapropel S1 (cf. Figure 6; Rohling, 1994; Rohling et al., 2004, 2015) added to the enhanced river discharge in the Eastern Mediterranean Basin, as observed eastward in the Siculo-Tunisian strait between ca. 9.5–6 ka BP (Bout-Roumazeille et al., 2013). We suggest that enhanced African monsoons (e.g. Emeis et al., 2000 ; Kallel et al., 1997 ; De Menocal et al., 2000 ; Tachikawa et al., 2015 ; Siani et al., 2013), associated with the cessation of deep and intermediate water formation (Frigola et al., 2007; Toucanne et al., 2012), may have favored organic matter and therefore heterotrophic cyst preservation, and especially that of the most sensitive taxa *Brigantedinium* spp., under anoxic bottom waters in the Mediterranean Sea. Low productive conditions in the AM, as also confirmed by significant co-occurrences of *I. aculeatum* and *S. mirabilis* (Coussin et al., 2022), resonate with the oligotrophic conditions recorded in the Gulf of Cadiz (Penaud et al., 2016) that may have propagated in the WMB through advection of nutrient-poor subtropical North Atlantic Central Waters.

5.4. Middle Holocene (8.2–4.2 ka BP)

After an increasing trend across the Early Holocene, the Mediterranean forest reaches maximal values higher than 20% during the Mid-Holocene, while the Eurosiberian taxa do not show a significant increase (Figure 7f). These latter arboreal taxa require high moisture conditions and a reduced seasonality in the precipitation regime, therefore suggesting still moderate precipitation in the southern Mediterranean Basin as also confirmed by sclerophylous and mattorral observations (Figure 7g). The best coincidence interval for high-forest percentages in the three western Mediterranean sequences is recorded between 10 and 5.5 ka BP (green colored band in Figure 8). More specifically, the Mid-Holocene can be subdivided into three main phases.

5.4.1. The “8.2 ka BP” event

The first event, centered around 8.2 ka BP, lasting for about 100 to 200 years, is characterized by a significant drop in forest distribution (Figure 7f). This is reminiscent of the so-called “8.2 ka event” (Alley et al., 1997) that led to cold climate and hydrological conditions in the Northern Hemisphere and also affected the WMB (Combourieu Nebout et al., 1998, 2002; Magny et al., 2003; Zanchetta et al., 2007; Fletcher and Sanchez-Goñi, 2008; Pross et al., 2009;

Depreux et al., 2021) by limiting the precipitation pattern (Berger and Guilaine, 2009; Morrill et al., 2013). During this arid event, anomalously low fluvial discharge may be responsible for lower concentrations of pre-Quaternary cysts, *Glomus* spores, and freshwater microalgae in the AM (Figure 5a, 7b,c). This drought interval is also obvious with low values of the ratios Ti/Ca-XRF ratio (Figure 6h) and Kaolinite/Illite (Figure 7a) thus respectively suggesting both lower river runoff and chemical alteration. The 8.2 ka BP event is also known as a cold event with lowered SSTs, as recorded by alkenone SST (Figure 6b).

5.4.2. The African Humid Period

Between 8 and 6 ka BP, evergreen oaks largely dominated the Mediterranean forest (Figure 5b, 7f), with the maxima recorded at that time, associated with the highest representation of *Pistacia* and *Olea*, and the lowest representation of coastal-steppic and semi-arid taxa (Figure 7g), suggesting decreasing summer aridity and mild winters. From 8 to 6 ka BP, this important increase in moisture is consistent with previous studies conducted in the southwestern Mediterranean lowland areas (Fletcher et al., 2013; Jaouadi et al., 2016).

In addition, high river discharges are highlighted by increasing pre-Quaternary cyst and *Glomus* spore concentrations, as well as by the first significant increases in freshwater microalgae concentrations (Figure 7b) and significant low excursions of dinocyst-based SSS estimates (salinity drops of around 1.5 psu; Figure 6d). Simultaneously, higher Kaolinite (Figure 7a) and Ti/Ca-XRF (Figure 6h) values attest to increasing chemical alteration and river runoff, in a context of warmer SSTs suggested by dinocyst-derived and alkenone reconstructions (1.5°C higher than present; Figure 6b,c). This interval of increased precipitation in the Algerian highlands is synchronously recorded by several studies in the Maghreb region (Jaouadi et al., 2016; Lebreton et al., 2019; Depreux et al., 2021) and by Mediterranean simulations (Brayshaw et al., 2011; Peyron et al., 2017). At this time, rains grew stronger and spread northward into the Sahara with enhanced summer rainfall in Africa and other parts of the tropics (e.g. de Menocal et al., 2000; McGee et al., 2013). No monsoon precipitations are recorded in the studied Western Mediterranean area (Tzedakis, 2007; Brayshaw et al., 2011), but increasing moisture attests to the strongest phase of summer rainfall (average annual precipitation of 650 mm; 270 mm higher than the present) in a context of enhanced temperature seasonality (Figure 7h).

After the oligotrophic cooler conditions of the Early Holocene, higher nutrient-enriched fluvial discharge may explain a slight increase in productivity, as suggested by increasingly heavy values of planktonic $\delta^{13}C$ and a slight increase in phototrophic cyst concentrations (Figure 6f,g).

However, the Middle Holocene also records the strongest representation of the subtropical taxon *I. aculeatum*, concomitantly with Alboran Sea and Gulf of Cadiz sequences (Penaud et al., 2011, 2016; Rouis-Zargouni et al., 2012), this taxon signing for warmer-oligotrophic sea surface conditions. We therefore suggest that the high mid-Holocene SSTs may have prolonged the seasonal length of water column stratification and thus the deepening of the thermocline. We hypothesize that the subsequent deepening of the nutricline mitigated the productive conditions, explaining the low contrast between early and Middle Holocene productivity regimes.

At ca 8 ka BP, the shift between the Early and Middle-Holocene is marked by the onset of the Western Alboran Gyre circulation (Rohling et al., 1995; Pérez-Folgado et al., 2003; Ausín et al., 2015), promoting enhanced Atlantic water inflow into the Mediterranean Basin and the onset of the AC flow through the east, consistently with the increased Ocen/Lmac ratio from Cadiz to Algeria (Figure 8f,i,l,o). Interestingly, from 8 ka BP, the easternmost Ocen/Lmac signature shows an inverse trend to that of all western Mediterranean sequences, suggesting a strong depletion of the Atlantic influence from the Middle-Holocene at the Siculo-Tunisian strait, while increasing Ocen/Lmac ratios were synchronously recorded for the cold YD from west to east in the five sediment cores (Figure 8f,i,l,o,r).

5.4.3. Mediterranean forest retreat onset

From 6 ka BP, the progressive decline in forest taxa and the increase in coastal-steppic taxa percentages, associated with decreasing fluxes of TERR-alkanes as well as decreasing concentrations of pollen, *Glomus* spores, freshwater microalgea and pre-Quaternary cysts (Figure 7b,c,d,f,g) suggest decreasing precipitation rates and runoff in the AM. Summer precipitation therefore gradually declined (Figure 7i), due to the decrease in summer solar radiation in the tropics (Berger and Loutre, 1991), and climate conditions became too dry for plants. The sharp drops in Ti/Ca-XRF (Figure 6h) and Kaolinite values (Figure 7a) also suggest dusty-desert conditions, in agreement with previous western Mediterranean aridification signals (e.g. Fletcher and Zielhofer, 2013; Depreux et al., 2021), therefore characterizing the end of the AHP (Shanahan et al., 2015). The aridity trend, that started after 6 ka BP, ranged from about 5.5 to 3 ka BP (yellow band identified between limits “d” and “e” in Figures 6 and 7), consistently with an extremely dry interval described in western Mediterranean studies at the end of the African Humid Period (Cacho et al., 2001; Combourieu-Nebout et al., 2009), and also corresponding to increasing flash floods in Tunisia and Morocco due to erodible soils in

open landscape (Zielhofer and Faust, 2008; Depreux et al., 2021). During this interval, phototrophic productivity and higher dinocyst diversity (Figure 4a) coincide with ever-increasing heavy values of planktonic $\delta^{13}C$ (Figure 6g). Productive conditions are related to decreasing percentages of *I. aculeatum* (i.e. SST cooling) and increasing percentages of *S. mirabilis* (i.e. Atlantic water influence), suggesting, as for the YD (section 5.2.a.), a stronger vigour of the AC resulting from the strengthening of the Alboran gyres. Lower *Brigantedinium* spp. values may result from a lower preservation under stronger ventilation of Mediterranean bottom waters at that time.

5.5. Late Holocene (4.2 ka BP to present)

5.5.1. The "4.2 ka BP" event

Peak values of coastal-steppic and semi-arid taxa percentages culminated between 4.3 and 3.9 ka BP, coupled with the lowest *Glomus* spore concentrations recorded in the sequence, and may correspond to a phase of megadrought in Algeria (MDA in Figure 7) that lasted for about 400 years (Figure 7g), consistent with a regional speleothem study from Ruan et al. (2016). The highest summer droughts recorded in the study area therefore appear synchronous with the well-known 4.2 ka BP event (e.g. Jalali et al., 2016; Bini et al., 2019, Kaniewski et al., 2019; Di Rita and Magri, 2019), within the 5.5–3 ka BP interval. This also coincides with the development of the plateau of the heaviest planktonic $\delta^{13}C$ values (i.e. strongest productivity from 4.2 ka BP onward) in a context where the lowest percentages of *Brigantedinium* spp. were recorded, likely due to a strengthening of deep-water circulation at 4.2 ka BP (Figure 6g,i).

5.5.2. Settling of Modern conditions

The Late Holocene is characterized by the end of the 5.5–3 ka BP most arid Holocene interval followed by the last 3 kyrs BP occurring in a context of orbitally-driven climate aridity. From the Middle to Late Holocene, Mediterranean landscapes are strongly influenced by human impacts and fire activity (Pausas and Vallejo 1999, Vannière et al., 2008; Mercuri et al., 2019). Over the last 3 kyrs BP, two phases are identifiable in this study. First, from 3 to 1.5 ka BP, strong river discharge to the AM and associated runoff are recognized through increasing Ti/Ca-XRF (Figure 6h) and Kaolinite/Illite (Figure 7a) values. Pre-Quaternary cyst (Figure 5a), *Glomus* spore and freshwater microalgae (Figure 7b,c) concentrations, even reached their highest values over this period. Stronger signals of alteration-erosion and river runoff to the

AM directly follow the 5.5–3 ka BP interval, as observed during the Early Holocene right after the YD. Only the freshwater algae remain stable with low values during the Early Holocene compared with the 3–1.5 ka BP interval. The 3 to 1.5 ka BP interval also corresponds to increasing advection of Anthropogenic Pollen Indicators (*Rumex*, *Cerealia*-type and *Plantago lanceolata*) as well as Amaranthaceae and *Artemisia* (Figure 5b), likely resulting from pastures, as previously suggested in arid climates (Jaouadi et al., 2010; Florenzano *et al*., 2012; Florenzano *et al*., 2015). Two factors may have amplified the signature of river erosion-runoff: i) the arid conditions prevailing that favored strong erodability of soils, and ii) the superimposed growing anthropic impacts opening the landscapes in adjacent watersheds (e.g. Pastoralism, culture parcels and land clearing).

The second phase, from 1.5 ka BP to the top of the sequence, presents a sharp drop in Mediterranean forest taxa percentages in parallel with the highest Kaolinite/Illite (strongest chemical alteration ; Figure 7a) and Ti/Ca-XRF values (strongest erosional-runoff processes; Figure 6h). The antagonist pattern between "*Glomus* spore - freshwater microalgae" concentrations and Kaolinite/Illite values (i.e. opposite their general covariation during the whole sequence) lead to interpret this interval as driven by anthropogenic forcing.

Regarding surface waters, the plateau of heavy planktonic $\delta^{13}C$ values, starting at 3 ka BP coincides with decreasing *Impagidinium* spp. percentages and concentrations. At this period, *Brigantedinium* spp. percentages and concentrations maintain their highest values, with concentrations of heterotrophic cysts (Figure 6f) even significantly exceeding those of autotrophic cysts for the first time of the whole study sequence. From 3 ka BP, the upwelling taxon *T. applanatum* reaches its highest percentages and concentrations (Figure 5a). We therefore argue for the development of the current hydrographic conditions (cf. Figure 1a), where productivity is sustained by both vertical mixing due to the AC in the AM (wind-driven eddies) and nutrient-enriched fluvial discharge intensified by anthropic-driven land-use. Interestingly, the threshold previously highlighted at 1.5 ka BP (limit "f" in Figure 6) corresponds to a marked drop in alkenone and dinocyst-derived SST estimates, that also corresponds to reduced dinocyst-derived SSS estimates. From 1.5 ka BP to present, this SST and SSS decrease would confirm that strong advection of continental waters, accelerated by anthropic-driven erosional processes, can be superimposed on the post-3 ka BP setup of modern sea surface conditions, participating in the present-day primary productivity in the AM.

5.6. West to East Mediterranean Basin transect

5.6.1. Regional disparities in hydrological-climatic trends along the Holocene

Pollen records from north-eastern Algeria, and more specifically marine records from the Siculo-Tunisian Strait, show a progressive Late Holocene evolution characterized by higher precipitation rates (Figure 8g, j, m, p). This may be due to the Mediterranean storm track carrying increased moisture from the Atlantic through the Gulf of Lion to the north-eastern Algeria, northern Tunisian and Sicilian areas (Desprat et al., 2013; Lionello et al., 2016). During the Late Holocene, the northward storm track, affecting less frequently the westernmost Mediterranean regions (i.e. Alboran Sea for instance characterized by increasing aridity despite lower summer temperatures), would be responsible for stronger Mediterranean storms from the Gulf of Lion to the Central Mediterranean Sea as presently observed (Lionello et al., 2006).

This dichotomy between climate trends recorded in the Alboran Sea and AM is furthermore reflected by highest alkenone SST reached between 10–8 ka BP westward (and decreasing afterwards following NGRIP temperatures; cf. ODP 976 data in Figure 8a, h). These temperature ranges are reached from 8 ka BP eastward (particularly obvious with core MD04-2801 data in Figure 8n). The increasing SST gradient from west to east is also evident whatever the interval considered over the last 14 kyrs.

5.6.2. Rapid Holocene climate changes

Rapid decline of forest at the infra-millennial timescale suggests events of enhanced continental aridity, synchronously with alkenone SST coolings at 9, 8.2, 7.3 and 6.5 ka BP (horizontal dotted lines in Figure 8). These cold, arid events have already been described in marine and continental studies from SW Iberia to the WMB (Cacho et al., 2001; Frigola et al., 2007; Jalut et al., 2000, 2009; Fletcher and Sanchez-Goñi, 2008; Combourieu-Nebout et al., 2009; Chabaud et al., 2014; Jalali et al., 2016; Azuara et al., 2020) and are associated with the North Atlantic Bond events (Bond et al., 2001; Figure 8e). Several studies suggest that changes in North Atlantic thermohaline circulation could have triggered the multi-centennial scale climate variability of the WMB (Bianchi and McCave, 1999; Bond et al., 2001; Oppo et al., 2006; Fletcher and Sanchez-Goñi, 2008; Combourieu-Nebout et al., 2009, Chabaud et al., 2014).

From the Early Holocene, the AM forest decline events are generally synchronous with lower alkenone SST and higher *O. centrocarpum* occurrences figured out by positive values of the Ocen/Lmac ratio (Figure 8n,o). This suggests enhanced inflow of Atlantic waters in the WMB and stronger moisture transport by the westerlies track directed northward and affecting to a lesser extent the westernmost part of the Mediterranean Sea. By analogy, this would correspond to recurrent positive modes of the North Atlantic Oscillation (NAO). Interestingly, these

positive “NAO-like” events are expressed in contrast in the Siculo-Tunisian strait with lower *O. centrocarpum* and higher values of *L. machaerophorum* occurrences, suggesting stronger river discharge eastward. This pattern could illustrate the west-east modeled dipole response to NAO-like changes in the SW Mediterranean Basin according to Bini et al. (2019) and Perşoiu et al. (2019).

Dryer conditions, under enhanced wind strength in northern Atlantic latitudes (i.e. Bond event under recurrent phases of positive “NAO-like” conditions), may therefore explain lower tree percentages (Fletcher et al., 2010, 2013), and reversely higher tree percentages during recurrent phases of negative “NAO-like” conditions (Figure 8). Our study reveals the rapid response of Mediterranean vegetation and hydrological dynamics and the strong influence of the North Atlantic climate through atmosphere-ocean interactions and ocean circulation at a multi-centennial time scale.

6. Conclusion

Multiproxy investigation of dinoflagellate cysts, pollen, non-pollen palynomorphs, stable isotopes, clay mineral assemblages, grain-size analyses, marine and continental biomarkers, and climate and hydrological quantitative reconstructions were conducted on the marine core MD04-2801 on the Algerian Margin (AM). This study reveals the strong influence of orbital, multi-centennial and centennial forcing on hydrological conditions and vegetation dynamics over the last 14 kyrs BP. We show that dry and cold conditions prevailed during the Younger Dryas as well as strong marine productivity. Warmer conditions of the Early to Middle Holocene allowed for Mediterranean forest expansion, while the AM became oligotrophic until 6 ka BP. At an orbital timescale, the end of the African Humid Period led to aridification of the western Mediterranean at the Middle to Late Holocene transition, with a dramatic forest retreat, particularly pronounced between 4.3 and 3.9 ka BP. This event is referred to here as the Algerian Mega Drought event, that appeared synchronously with the « 4.2 ka BP » event. Sensitivity of the western Mediterranean to Northern Atlantic climate is also evidenced at an infra-orbital timescale through several cold-dry events around 9, 8.1, 7.3 and 6.5 ka BP. The forest decline from the Alboran Sea to the AM may result from the coupling of the North Atlantic Bond events with prevailing positive modes of the North Atlantic Oscillation (NAO) with a marked west to east dipole highlighted between the northern African coast up to Algeria and Tunisia. Finally, over the last 3 kyrs BP, we have underlined the development of modern productive conditions on the AM due to both vertical mixing (haline front and wind-driven eddies of the Algerian Current) and nutrient-enriched fluvial discharge intensified by anthropic-driven land-use.

7. Acknowledgements

This work was part of a PhD thesis (V.C.) financed by the *Région Bretagne* and UBO (Univ Brest). The work was supported by the French national programme (CNRS) LEFE-EC2CO (“DATAPOL”) and by the ISblue project, Interdisciplinary graduate school for the blue planet (ANR-17-EURE-0015), co-funded by a grant from the French government under the program "Investissements d'Avenir". The work was also supported by the INSU-Mistrals Progam - PaleoMex part. We thank Yannick Miras for his help in Non Pollen Palynomorph determination and discussions on their ecological signature. Thanks also to ISEM for their contribution.

8. Data availability

MD04-2801 data discussed in the manuscript are available in the SEANOE repository: https://doi.org/10.17882/89514

9. Table captions

Table 1: MD04-2801 AMS-^{14}C dates. Grey cells represent levels averaged for the final age model. Dates in italic (with the annotation « * ») were rejected for the final age model (Figure 2).

Table 2: This table presents MD04-2801 palynological data discussed in this study and describes each pollen zone for dinocyst and pollen grains assemblages.

10. Figure captions

Figure 1: a) Map presenting studied part of the Western Mediterranean Basin (WMB) on the globe (red square on global scale map) , sea-surface temperature, as well as major sea-surface and atmospheric currents (a simplified vegetation model according to Tassin (2012). b) Map presenting the local scale map (red square on regional scale map) figure topography and hydrographic network, high-resolution bathymetric data from the Algerian Margin (Babonneau et al., 2012), morphological entities of the Kramis deep-sea fan and location of the study core and selected corresponding modern sediments (Coussin et al., in prep.).

Figure 2: Age model for core MD04-280 based on the combination of age model a (lower section (1031 to 431 cm)) and age model b (upper section (431 to 0 cm)) from rbacon package calculation (Blaauw and Christen, 2011) performed under the R interface (version 4.1.0; R Development Core Team, 2021; http://www.r-project.org/) and rejected dates. Stratigraphic data includes the corresponding section number and photography, lithology, sediments density (g/cm^3), sedimentation rates (cm/kyrs) and Vp (m/s) values. Core disturbance by potential piston effect is represented as a red square on the age model.

Figure 3: Sedimentological data of core MD04-2801 in function of depth, core section and lithology. a) XRF Ca/Al ratio, b) XRF Ti/Al ratio, c) Magnetic susceptibility (SI). d) Low

resolution total sediment D50 (µm) in blue reported in faded blue on high-resolution total grain-size (d) and $CaCO_3$-free D50 in red. e) Planktonic (*G. bulloides*; in green) and endobenthic (*G. affinis*; in yellow) δ13C (‰ VPDB), higher planktonic signal suggests stronger primary productivity while lower endobenthic signal suggests stronger organic matter remineralisation. f) Planktonic (*G. bulloides*; in red) and endobenthic (*G. affinis*; in violet) δ18O (‰). g) Clay mineral fractions of Interstratified Illite-Smectite (In), Chlorite (Ch), Kaolinite (Kao) and Illite (Il).

Figure 4: MD04-2801 a) marine and b) continental palynological, biomarkers and MAT reconstruction data against depth (cm). a) Dinocyst diversity indexes are shown in red and blue, in parallel with percentages of the major species *Brigantedinium* spp. (red dotted line). Concentration of the total sum of dinocysts is shown in black, total sum of dinocysts without *Brigantedinium* spp. is represented in blue and *Brigantedinium* spp. concentration is represented in red. Concentration of C_{37} alkenones is represented in light blue (sum of C_{37}, ng/g). Total dinocyst (blue) and pollen with *Pinus* (orange) concentrations are represented in the logarithmic scale. b) Pollen diversity indexes are in green, in parallel with percentages of total trees (green) and total trees with *Pinus* (orange). Concentration of the total sum of pollen is shown in orange, total sum of dinocysts without *Pinus* in green. Concentration of TERR-alkanes in brown (sum of TERR-alkanes, ng/g) and Average Chain Length (ACL) in yellow with average sequence value as a dotted line.

Figure 5: a) Dinocyst diagram (percentages of selected taxa exceeding at least once 1% in all studied samples) of the MD04-2801 core, with related ecological groups (cf. Coussin et al., 2022). Dinocyst zones are based on a CONISS statistical analysis on the Tilia program. b) Pollen diagram (percentages of selected taxa when exceeding at least once 1% in all studied samples, *Pinus* excluded from the main pollen sum) for the MD04-2801 core, with related ecological groups. For both a) and b), continental non-pollen palynomorphs (NPPs) and pre-quaternary cysts are highlighted in concentrations (number of palynomorphs per cm^3 of sediment). (For interpretation of the references to color in this figure legend, the reader is referred to the web version of this article.)

Figure 6: Oceanic proxies from the MD04-2801 core plotted in age (Cal years BP) with related pollen zones, sedimentological, stratigraphical limits and remarquable periods (S1 = Sapropel 1). Modern values from KMDJ-23 core are plotted as colored stars in the left band of the figure

(1 - 0 ka). a) Planktonic δ18O (‰), b) Alkenone derived annual Sea Surface Temperatures (SST, shaded from low temperatures in blue to high temperatures in red, °C), c) Cold water dinocyst taxa percentages (*N. labyrinthus, B. tepikiense* and *S. lazus*, cf. Figure 5) in reversed logarithmic scale, d) Dinocysts-derived Winter (blue) and Summer (red) SST (°C) with shaded reconstructed minima and maxima and alkenone annual SST as a dotted blue line. e) Dinocyst-derived Winter (blue) and Summer (red) Sea Surface Salinity (SSS, psu) with shaded reconstructed minima and maxima, f) Heterotrophic (orange) and Phototrophic (green) dinocyst concentration in logarithmic scale, g) Planktonic (*G. bulloides*; in green) and endobenthic (*G. affinis*; in orange) δ13C (‰ VPDB), h) XRF Ti/Ca ratio, i) *Brigantedinium* spp. percentages (%), j) *Brigantedinium* spp. concentration (red line), k) *Impagidinium* spp. percentages (%), l) *Impagidinium* spp. concentration (brown).

Figure 7: Continental proxies from the MD04-2801 core plotted in age (Cal years BP) with related pollen zones, sedimentological, stratigraphical limits and exceptional periods (S1 = Sapropel 1, Megadrought Algeria = MDA). Modern values from KMDJ-23 core are plotted as colored stars in the left band of the figure (1 - 0 ka). a) Kaolinite/Illite percentages of the clayey phase ratio with higher Illite values in green and higher values in Kaolinite in red, b) freshwater algae concentration (green) , c) Glomus (HDV-207) concentration (grey), d) superior plant leaf wax produced TERR-alkane (shaded green silhouette) and major represented n-C29 + n-C-31 (green dotted line) fluxes ($ng.g^{-1}.yrs^{-1}$), e) Siliciclastic coarse grain inputs schematized by magnetic susceptibility (SI), f) Mediterranean and Eurosiberian forest (cf. Figure 5) percentages, g) Coastal-steppic and Semi-arid vegetation (cf. Figure 5) percentages, h) Temperature seasonality index calculated with pollen-derived Mean Temperature of the Warmest Month (MTWA) and Mean Temperature of the Coldest Month (MTCO) as (MTWA-MTCO). i) Pollen-derived annual precipitation reconstructions (mm, blue line), j) Altitudinal forest (cf. Figure 5), k) Human impact taxa (cf. Figure 5) percentages.

Figure 8: West to east transect of sequences from the Gulf of Cadiz (MD99-2339), Alboran sea (ODP site 976 and MD95-2043), Algerian Margin (MD04-2801, this study) and Sicilian strait (MD04-2797) with paleoenvironmental data plotted in age (Cal years BP) both on their published chronology and their geographical situation on the map versus Orbital parameters (a) NGRIP δ18O (‰, Vinther et al., 2006) in black, b) 65°N insolation in yellow (W/m^2) from Berger and Loutre (1991), c) Precession in blue and e) Hematite-stained quartz % in red (Bond

et al., 2001). For both represented cores, (d,h,k,n,q) Alkenone SST are represented (black line, °C), (f,I,l,o,r) OCEN/LMAC log ratio representing oceanic dinocyst taxa *O. centrocarpum* versus estuarine dinocyst taxa *L. machaerophorum* log ratio (blue shaded silhouette, higher ratios represent lower river discharge conditions), (g,j,m,p) Summed Mediterranean and Eurosiberian forest (%) with total sum as a green silhouette and eurosiberian proportion as a brown dotted line. Spotted forest retreat events are shown as dotted horizontal lines with corresponding ages. The regional map figures all cited sequences, geographical coordinates and zonal correlations with negative NAO conditions (modified after Perşoiu et al. (2019) in Bini et al. (2019). Green zones show positive correlations with NAO- conditions indicating stronger precipitations than average during NAO- and orange zones figure negative correlations with NAO- conditions indicating lower precipitations than average during NAO-.

11. References

Allen, J.R.M., Watts, W.A., McGee, E., Huntley, B., 2002. Holocene environmental variability—the record from Lago Grande di Monticchio, Italy. Quaternary International 88, 69–80.

Alley, R.B., Mayewski, P.A., Sowers, T., Stuiver, M., Taylor, K.C., Clark, P.U., 1997. Holocene climatic instability: A prominent, widespread event 8200 yr ago. Geology 25, 483–486.

Arnone, R.A., La Violette, P.E., 1986. Satellite definition of the bio-optical and thermal variation of coastal eddies associated with the African Current. Journal of Geophysical Research: Oceans 91, 2351–2364.

Arnone, R.A., Wiesenburg, D.A., Saunders, K.D., 1990. The origin and characteristics of the Algerian Current. Journal of Geophysical Research: Oceans 95, 1587–1598.

Ausín, B., Flores, J.A., Sierro, F.J., Cacho, I., Hernández-Almeida, I., Martrat, B., Grimalt, J.O., 2015. Atmospheric patterns driving Holocene productivity in the Alboran Sea (Western Mediterranean): a multiproxy approach. The Holocene 25, 583–595.

Azuara, J., Sabatier, P., Lebreton, V., Jalali, B., Sicre, M.-A., Dezileau, L., Bassetti, M.-A., Frigola, J., Combourieu-Nebout, N., 2020. Mid- to Late-Holocene Mediterranean climate variability: Contribution of multi-proxy and multi-sequence comparison using wavelet spectral analysis in the northwestern Mediterranean basin. Earth-Science Reviews 208, 103232.

Babonneau, N., Cattaneo, A., Savoye, B., Barjavel, G., Déverchère, J., Yelles, K., 2012. The Kramis fan offshore western Algeria: the role of sediment waves in turbiditic levee growth. SEPM Special Publication 99, 293–308.

Bahr, A., Jiménez- Espejo, F.J., Kolasinac, N., Grunert, P., Hernández- Molina, F.J., Röhl, U.,

Voelker, A.H., Escutia, C., Stow, D.A., Hodell, D., 2014. Deciphering bottom current velocity and paleoclimate signals from contourite deposits in the G ulf of C ádiz during the last 140 kyr: An inorganic geochemical approach. Geochemistry, Geophysics, Geosystems 15, 3145–3160.

Bahr, A., Kaboth, S., Jiménez-Espejo, F.J., Sierro, F.J., Voelker, A.H., Lourens, L., Röhl, U., Reichart, G.-J., Escutia, C., Hernandez-Molina, F.J., 2015. Persistent monsoonal forcing of Mediterranean Outflow Water dynamics during the late Pleistocene. Geology 43, 951–954.

Bakun, A., Agostini, V.N., 2001. Seasonal patterns of wind-induced upwelling/downwelling in the Mediterranean Sea. scimar 65, 243–257.

Barbéro, M., Quézel, P., Rivas-Martínez, S., 1981. Contribution à l'étude des groupements forestiers et préforestiers du Maroc. Phytocoenologia 311–412.

Bárcena, M.A., Cacho, I., Abrantes, F., Sierro, F.J., Grimalt, J.O., Flores, J.A., 2001. Paleoproductivity variations related to climatic conditions in the Alboran Sea (western Mediterranean) during the last glacial–interglacial transition: the diatom record. Palaeogeography, Palaeoclimatology, Palaeoecology 167, 337–357.

Bar-Matthews, M., Ayalon, A., Gilmour, M., Matthews, A., Hawkesworth, C.J., 2003. Sea–land oxygen isotopic relationships from planktonic foraminifera and speleothems in the Eastern Mediterranean region and their implication for paleorainfall during interglacial intervals. Geochimica et Cosmochimica Acta 67, 3181–3199.

Bar-Matthews, M., Ayalon, A., Kaufman, A., 2000. Timing and hydrological conditions of Sapropel events in the Eastern Mediterranean, as evident from speleothems, Soreq cave, Israel. Chemical Geology 169, 145–156.

Beaudouin, C., Suc, J.-P., Escarguel, G., Arnaud, M., Charmasson, S., 2007. The significance of pollen signal in present-day marine terrigenous sediments: The example of the Gulf of Lions (western Mediterranean Sea). Geobios 40, 159–172.

Belkebir, L., Labdi, A., Mansour, B., Bessedik, M., Saint-Martin, J.-P., 2008. Biostratigraphie et lithologie des séries serravallo-tortoniennes du massif du Dahra et du bassin du Chélif (Algérie). Implications sur la position de la limite serravallo-tortonienne. Geodiversitas 30, 9–19.

Ben Tiba, B., Reille, M., 1982. Recherches pollenanalytiques dans les montagnes de Kroumirie (Tunisie septentrionale): premiers résultats. Ecologia mediterranea 8, 75–86.

Berger, A., Loutre, M.-F., 1991. Insolation values for the climate of the last 10 million years. Quaternary Science Reviews 10, 297–317.

Berger, J.-F., Guilaine, J., 2009. The 8200 cal BP abrupt environmental change and the Neolithic transition: A Mediterranean perspective. Quaternary international 200, 31–49.

Béthoux, J.P., 1984. Paléo-hydrologie de la Méditerranée au cours des derniers 20 000 ans. Oceanologica acta 7, 43–48.

Bethoux, J.P., 1979. Budgets of the Mediterranean Sea-Their dependance on the local climate and on the characteristics of the Atlantic waters. Oceanologica acta 2, 157–163.

Bethoux, J.P., Gentili, B., 1994. The Mediterranean Sea, a Test Area for Marine and Climatic Interactions, in: Malanotte-Rizzoli, P., Robinson, A.R. (Eds.), Ocean Processes in Climate Dynamics: Global and Mediterranean Examples, NATO ASI Series. Springer Netherlands, Dordrecht, pp. 239–254.

Bianchi, G.G., McCave, I.N., 1999. Holocene periodicity in North Atlantic climate and deep-ocean flow south of Iceland. Nature 397, 515–517.

Biebow, N., 1996. Dinoflagellatenzysten als Indikatoren der spät-und postglazialen Entwicklung des Auftriebsgeschehens vor Peru (PhD Thesis). GEOMAR Forschungszentrum für marine Geowissenschaften der Christian ….

Bini, M., Zanchetta, G., Perşoiu, A., Cartier, R., Català, A., Cacho, I., Dean, J.R., Di Rita, F., Drysdale, R.N., Finnè, M., 2019. The 4.2 ka BP Event in the Mediterranean region: an overview. Climate of the Past 15, 555–577.

Blaauw, M., Christen, J.A., 2011. Flexible paleoclimate age-depth models using an autoregressive gamma process. Bayesian analysis 6, 457–474.

Bliedtner, M., Schäfer, I.K., Zech, R., von Suchodoletz, H., 2018. Leaf wax n-alkanes in modern plants and topsoils from eastern Georgia (Caucasus)–implications for reconstructing regional paleovegetation. Biogeosciences 15, 3927–3936.

Bogus, K., Mertens, K.N., Lauwaert, J., Harding, I.C., Vrielinck, H., Zonneveld, K.A.F., Versteegh, G.J.M., 2014. Differences in the chemical composition of organic-walled dinoflagellate resting cysts from phototrophic and heterotrophic dinoflagellates. Journal of Phycology 50, 254–266.

Bond, G., Kromer, B., Beer, J., Muscheler, R., Evans, M.N., Showers, W., Hoffmann, S., Lotti-Bond, R., Hajdas, I., Bonani, G., 2001. Persistent solar influence on North Atlantic climate during the Holocene. science 294, 2130–2136.

Bond, G., Showers, W., Cheseby, M., Lotti, R., Almasi, P., deMenocal, P., Priore, P., Cullen, H., Hajdas, I., Bonani, G., 1997. A Pervasive Millennial-Scale Cycle in North Atlantic Holocene and Glacial Climates. Science 278, 1257–1266.

Bordon, A., Peyron, O., Lézine, A.-M., Brewer, S., Fouache, E., 2009. Pollen-inferred late-glacial and Holocene climate in southern Balkans (Lake Maliq). Quaternary International 200, 19–30.

Bouimetarhan, I., Marret, F., Dupont, L., Zonneveld, K., 2009. Dinoflagellate cyst distribution in marine surface sediments off West Africa (17–6 N) in relation to sea-surface conditions, freshwater input and seasonal coastal upwelling. Marine Micropaleontology 71, 113–130.

Bout-Roumazeilles, V., Combourieu Nebout, N., Peyron, O., Cortijo, E., Landais, A., Masson-

Delmotte, V., 2007. Connection between South Mediterranean climate and North African atmospheric circulation during the last 50,000yrBP North Atlantic cold events. Quaternary Science Reviews 26, 3197–3215.

Bout-Roumazeilles, V., Combourieu-Nebout, N., Desprat, S., Siani, G., Turon, J.-L., Essallami, L., 2013. Tracking atmospheric and riverine terrigenous supplies variability during the last glacial and the Holocene in central Mediterranean. Climate of the Past 9, 1065–1087.

Bout-Roumazeilles, V., Cortijo, E., Labeyrie, L., Debrabant, P., 1999. Clay mineral evidence of nepheloid layer contributions to the Heinrich layers in the northwest Atlantic. Palaeogeography, Palaeoclimatology, Palaeoecology 146, 211–228.

Brayshaw, D.J., Hoskins, B., Black, E., 2010. Some physical drivers of changes in the winter storm tracks over the North Atlantic and Mediterranean during the Holocene. Philosophical Transactions of the Royal Society A: Mathematical, Physical and Engineering Sciences 368, 5185–5223.

Brayshaw, D.J., Rambeau, C.M., Smith, S.J., 2011. Changes in Mediterranean climate during the Holocene: Insights from global and regional climate modelling. The Holocene 21, 15–31.

Brun, A., 1989. Microflores et paléovégétations en Afrique du Nord depuis 30 000 ans. Bulletin de la Société géologique de France 25–33.

Bryden, H.L., Kinder, T.H., 1991. Steady two-layer exchange through the Strait of Gibraltar. Deep Sea Research Part A. Oceanographic Research Papers 38, S445–S463.

Cacho, I., Grimalt, J.O., Canals, M., Sbaffi, L., Shackleton, N.J., Schönfeld, J., Zahn, R., 2001. Variability of the western Mediterranean Sea surface temperature during the last 25,000 years and its connection with the Northern Hemisphere climatic changes. Paleoceanography 16, 40–52.

Cacho, I., Grimalt, J.O., Pelejero, C., Canals, M., Sierro, F.J., Flores, J.A., Shackleton, N., 1999. Dansgaard- Oeschger and Heinrich event imprints in Alboran Sea paleotemperatures. Paleoceanography 14, 698–705.

Castañeda, I.S., Werne, J.P., Johnson, T.C., Filley, T.R., 2009. Late Quaternary vegetation history of southeast Africa: the molecular isotopic record from Lake Malawi. Palaeogeography, Palaeoclimatology, Palaeoecology 275, 100–112.

Chabaud, L., Sánchez Goñi, M.F., Desprat, S., Rossignol, L., 2014. Land–sea climatic variability in the eastern North Atlantic subtropical region over the last 14,200 years: atmospheric and oceanic processes at different timescales. The Holocene 24, 787–797.

Cheddadi, R., Fady, B., François, L., Hajar, L., Suc, J.-P., Huang, K., Demarteau, M., Vendramin, G.G., Ortu, E., 2009. Putative glacial refugia of Cedrus atlantica deduced from Quaternary pollen records and modern genetic diversity. Journal of Biogeography 36, 1361–1371.

Cheddadi, R., Lamb, H.F., Guiot, J., van der Kaars, S., 1998. Holocene climatic change in Morocco: a quantitative reconstruction from pollen data. Climate dynamics 14, 883–890.

Combourieu Nebout, N.C., Londeix, L., Baudin, F., Turon, J.-L., von Grafenstein, R., Zahn, R., 1999. Quaternary marine and continental paleoenvironmentsin the Western Mediterranean (Site 976, Alboran Sea): palynological evidence.

Combourieu Nebout, N.C., Peyron, O., Dormoy, I., Desprat, S., Beaudouin, C., Kotthoff, U., Marret, F., 2009. Rapid climatic variability in the west Mediterranean during the last 25 000 years from high resolution pollen data. Clim. Past 19.

Combourieu Nebout, N.C., Turon, J.L., Zahn, R., Capotondi, L., Londeix, L., Pahnke, K., 2002. Enhanced aridity and atmospheric high-pressure stability over the western Mediterranean during the North Atlantic cold events of the past 50 ky. Geology 30, 863–866.

Combourieu-Nebout, N., Paterne, M., Turon, J.-L., Siani, G., 1998. A high-resolution record of the last deglaciation in the central Mediterranean Sea: Palaeovegetation and palaeohydrological evolution. Quaternary Science Reviews 17, 303–317.

Coussin V., Penaud A., Combourieu-Nebout N., Peyron O., Schmidt S., Zaragosi S., De Vernal A., Babonneau N., 2022. Distribution of modern dinocyst and pollen grains in the Western Mediterranean Sea (Algerian margin and Gulf of Lion). Marine Micropaleontology 175, 102157.

Cugny, C., Mazier, F., Galop, D., 2010. Modern and fossil non-pollen palynomorphs from the Basque mountains (western Pyrenees, France): the use of coprophilous fungi to reconstruct pastoral activity. Veget Hist Archaeobot 19, 391–408.

Damsté, J.S.S., Verschuren, D., Ossebaar, J., Blokker, J., van Houten, R., van der Meer, M.T., Plessen, B., Schouten, S., 2011. A 25,000-year record of climate-induced changes in lowland vegetation of eastern equatorial Africa revealed by the stable carbon-isotopic composition of fossil plant leaf waxes. Earth and Planetary Science Letters 302, 236–246.

De Menocal, P.B., Ortiz, J., Guilderson, T., Adkins, J., Sarnthein, M., Baker, L., Yarusinsky, M., 2000. Abrupt onset and termination of the African Humid Period:: rapid climate responses to gradual insolation forcing. Quaternary science reviews 19, 347–361.

De Vernal, A., Eynaud, F., Henry, M., Hillaire-Marcel, C., Londeix, L., Mangin, S., Matthießen, J., Marret, F., Radi, T., Rochon, A., 2005. Reconstruction of sea-surface conditions at middle to high latitudes of the Northern Hemisphere during the Last Glacial Maximum (LGM) based on dinoflagellate cyst assemblages. Quaternary Science Reviews 24, 897–924.

De Vernal, A., Henry, M., Bilodeau, G., 1999. Techniques de préparation et d'analyse en micropaléontologie. Les cahiers du GEOTOP 3, 41.

De Vernal, A., Radi, T., Zaragosi, S., Van Nieuwenhove, N., Rochon, A., Allan, E., De

Schepper, S., Eynaud, F., Head, M.J., Limoges, A., Londeix, L., Marret, F., Matthiessen, J., Penaud, A., Pospelova, V., Price, A., Richerol, T., 2020. Distribution of common modern dinoflagellate cyst taxa in surface sediments of the Northern Hemisphere in relation to environmental parameters: The new n=1968 database. Marine Micropaleontology, Taxonomy and distribution of modern organic-walled dinoflagellate cysts in surface sediments from the Northern Hemisphere: an update of Rochon et al., 1999 159, 101796.

Depreux, B., Lefèvre, D., Berger, J.-F., Segaoui, F., Boudad, L., El Harradji, A., Degeai, J.-P., Limondin-Lozouet, N., 2021. Alluvial records of the African Humid Period from the NW African highlands (Moulouya basin, NE Morocco). Quaternary Science Reviews 255, 106807.

Desprat, S., Combourieu-Nebout, N., Essallami, L., Sicre, M.-A., Dormoy, I., Peyron, O., Siani, G., Bout Roumazeilles, V., Turon, J.-L., 2013. Deglacial and Holocene vegetation and climatic changes in the southern Central Mediterranean from a direct land–sea correlation. Climate of the Past 9, 767–787.

Di Rita, F., Lirer, F., Bonomo, S., Cascella, A., Ferraro, L., Florindo, F., Insinga, D.D., Lurcock, P.C., Margaritelli, G., Petrosino, P., 2018. Late Holocene forest dynamics in the Gulf of Gaeta (central Mediterranean) in relation to NAO variability and human impact. Quaternary Science Reviews 179, 137–152.

Di Rita, F., Magri, D., 2019. The 4.2 ka event in the vegetation record of the central Mediterranean. Climate of the Past 15, 237–251.

Dormoy, I., Peyron, O., Combourieu Nebout, N., Goring, S., Kotthoff, U., Magny, M., Pross, J., 2009. Terrestrial climate variability and seasonality changes in the Mediterranean region between 15 000 and 4000 years BP deduced from marine pollen records. Climate of the Past 5, 615–632.

Dugerdil, L., Joannin, S., Peyron, O., Jouffroy-Bapicot, I., Vannière, B., Boldgiv, B., Unkelbach, J., Behling, H., Ménot, G., 2021. Climate reconstructions based on GDGT and pollen surface datasets from Mongolia and Baikal area: calibrations and applicability to extremely cold–dry environments over the Late Holocene. Climate of the Past 17, 1199–1226.

Emeis, K.-C., Struck, U., Schulz, H.-M., Rosenberg, R., Bernasconi, S., Erlenkeuser, H., Sakamoto, T., Martinez-Ruiz, F., 2000. Temperature and salinity variations of Mediterranean Sea surface waters over the last 16,000 years from records of planktonic stable oxygen isotopes and alkenone unsaturation ratios. Palaeogeography, Palaeoclimatology, Palaeoecology 158, 259–280.

Fatela, F., Taborda, R., 2002. Confidence limits of species proportions in microfossil assemblages. Marine Micropaleontology 45, 169–174.

Fensome, R.A., 1993. A classification of living and fossil dinoflagellates. Micropaleontology, special publication 7, 1–351.

Fink, H.G., Wienberg, C., De Pol-Holz, R., Hebbeln, D., 2015. Spatio-temporal distribution

patterns of Mediterranean cold-water corals (Lophelia pertusa and Madrepora oculata) during the past 14,000 years. Deep Sea Research Part I: Oceanographic Research Papers 103, 37–48.

Fletcher, W.J., Debret, M., Goñi, M.F.S., 2013. Mid-Holocene emergence of a low-frequency millennial oscillation in western Mediterranean climate: Implications for past dynamics of the North Atlantic atmospheric westerlies. The Holocene 23, 153–166.

Fletcher, W.J., Sanchez Goñi, M., 2008. Orbital-and sub-orbital-scale climate impacts on vegetation of the western Mediterranean basin over the last 48,000 yr. Quaternary Research 70, 451–464.

Fletcher, W.J., Sanchez Goñi, M.F., Peyron, O., Dormoy, I., 2010. Abrupt climate changes of the last deglaciation detected in a Western Mediterranean forest record. Climate of the Past 6, 245–264.

Florenzano, A., Marignani, M., Rosati, L., Fascetti, S., Mercuri, A.M., 2015. Are Cichorieae an indicator of open habitats and pastoralism in current and past vegetation studies? Plant Biosystems - An International Journal Dealing with all Aspects of Plant Biology 149, 154–165.

Florenzano, A., Torri, P., Rattighieri, E., N'Siala, I.M., Mercuri, A.M., 2012. Cichorioideae-Cichorieae as pastureland indicator in pollen spectra from southern Italy 12.

Frigola, J., Moreno, A., Cacho, I., Canals, M., Sierro, F.J., Flores, J.A., Grimalt, J.O., Hodell, D.A., Curtis, J.H., 2007. Holocene climate variability in the western Mediterranean region from a deepwater sediment record. Paleoceanography 22.

Gautier, F., LUBES-NIEL, H., Sabatier, R., Masson, J.M., Paturel, J.-E., Servat, E., 1998. Variabilité du régime pluviométrique de l'Afrique de l'Ouest non sahélienne entre 1950 et 1989. Hydrological sciences journal 43, 921–935.

Gilman, C., Garrett, C., 1994. Heat flux parameterizations for the Mediterranean Sea: The role of atmospheric aerosols and constraints from the water budget. Journal of Geophysical Research: Oceans 99, 5119–5134.

Grimm, E., 1987. CONISS: a FORTRAN 77 program for stratigraphically constrained cluster analysis by the method of incremental sum of squares. Computers & Geosciences 13, 13–35.

Grimm, E.C., 1990. TILIA 2.0, Software. Illinois State Museum, Springfield.

Guiot, J., 1990. Methodology of the last climatic cycle reconstruction in France from pollen data. Palaeogeography, Palaeoclimatology, Palaeoecology 80, 49–69.

Guiot, J., de Vernal, A., 2007. Chapter thirteen transfer functions: Methods for quantitative paleoceanography based on microfossils. Developments in marine geology 1, 523–563.

Guizien, K., Charles, F., Lantoine, F., Naudin, J.-J., 2007. Nearshore dynamics of nutrients and chlorophyll during Mediterranean-type flash-floods. Aquat. Living Resour. 20, 3–14.

Hammer, O., Harper, D., Ryan, P., 2001. PAST: Paleontological Statistics Software Package for Education and Data Analysis. Palaeontologia Electronica, Palaeontologia Electronica 4, 1–9.

Harnickell, E., Mueller-Dombois, D., 1975. Climate-diagram maps of the individual continents and the ecological climatic regions of the earth. Springer-Verlag.

Havinga, A.J., 1971. An experimental investigation into the decay of pollen and spores in various soil types, in: Sporopollenin. Elsevier, pp. 446–479.

Havinga, A.J., 1967. Palynology and pollen preservation. Review of Palaeobotany and Palynology 2, 81–98.

Hernández-Molina, F.J., Stow, D.A., Alvarez-Zarikian, C.A., Acton, G., Bahr, A., Balestra, B., Ducassou, E., Flood, R., Flores, J.-A., Furota, S., 2014. Onset of Mediterranean outflow into the North Atlantic. Science 344, 1244–1250.

Heusser, L.E., Balsam, W.L., 1985. Pollen sedimentation in the Northwest Atlantic: Effects of the Western Boundary Undercurrent. Marine Geology 69, 149–153.

Howell, M.W., Thunell, R.C., 1992. Organic carbon accumulation in Bannock Basin: evaluating the role of productivity in the formation of eastern Mediterranean sapropels. Marine Geology 103, 461–471.

Jalali, B., Sicre, M.-A., Bassetti, M.-A., Kallel, N., 2016. Holocene climate variability in the North-Western Mediterranean Sea (Gulf of Lions). Clim. Past 12, 91–101.

Jalali, B., Sicre, M.-A., Kallel, N., Azuara, J., Combourieu-Nebout, N., Bassetti, M.-A., Klein, V., 2017. High-resolution Holocene climate and hydrological variability from two major Mediterranean deltas (Nile and Rhone). The holocene 27, 1158–1168.

Jalut, G., Dedoubat, J.J., Fontugne, M., Otto, T., 2009. Holocene circum-Mediterranean vegetation changes: climate forcing and human impact. Quaternary international 200, 4–18.

Jaouadi, S., Lebreton, V., Bout-Roumazeilles, V., Siani, G., Lakhdar, R., Boussoffara, R., Dezileau, L., Kallel, N., Mannai-Tayech, B., Combourieu-Nebout, N., 2016. Environmental changes, climate and anthropogenic impact in south-east Tunisia during the last 8 kyr. Climate of the Past 12, 1339–1359.

Jaouadi, S., Lebreton, V., Mulazzani, S., Boussofara, R., Mannai-Tayech, B., 2010. Analyses polliniques en contexte anthropisé: le cas du site holocène SHM-1 (Hergla, Tunisie centrale). Sezione di Museologia Scientifica e Naturalistica 6, 25–32.

Jimenez- Espejo, F.J., Martinez- Ruiz, F., Rogerson, M., González- Donoso, J.M., Romero, O.E., Linares, D., Sakamoto, T., Gallego- Torres, D., Rueda Ruiz, J.L., Ortega- Huertas, M., 2008. Detrital input, productivity fluctuations, and water mass circulation in the westernmost Mediterranean Sea since the Last Glacial Maximum. Geochemistry, Geophysics, Geosystems 9.

Kallel, N., Paterne, M., Duplessy, J.C., Vergnaudgrazzini, C., Pujol, C., Labeyrie, L., Arnold, M., Fontugne, M., Pierre, C., 1997. Enhanced rainfall in the Mediterranean region during the last sapropel event. Oceanolica Acta 20, 697–712.

Kaniewski, D., Marriner, N., Bretschneider, J., Jans, G., Morhange, C., Cheddadi, R., Otto, T., Luce, F., Van Campo, E., 2019. 300-year drought frames Late Bronze Age to Early Iron Age transition in the Near East: new palaeoecological data from Cyprus and Syria. Regional Environmental Change 19, 2287–2297.

Kodrans-Nsiah, M., de Lange, G.J., Zonneveld, K.A., 2008. A natural exposure experiment on short-term species-selective aerobic degradation of dinoflagellate cysts. Review of Palaeobotany and Palynology 152, 32–39.

Kotthoff, U., Müller, U.C., Pross, J., Schmiedl, G., Lawson, I.T., van de Schootbrugge, B., Schulz, H., 2008a. Lateglacial and Holocene vegetation dynamics in the Aegean region: an integrated view based on pollen data from marine and terrestrial archives. The Holocene 18, 1019–1032.

Kotthoff, U., Pross, J., Müller, U.C., Peyron, O., Schmiedl, G., Schulz, H., Bordon, A., 2008b. Climate dynamics in the borderlands of the Aegean Sea during formation of sapropel S1 deduced from a marine pollen record. Quaternary Science Reviews 27, 832–845.

Lamb, H.F., Eicher, U., Switsur, V.R., 1989. An 18,000-year record of vegetation, lake-level and climatic change from Tigalmamine, Middle Atlas, Morocco. Journal of biogeography 65–74.

Lebreton, V., Jaouadi, S., Bruneau, M., Karbouch, M., Boujelben, A., Montaldi, M., Berger, J.-F., 2019. History of semi-arid and arid environments in the Eastern Maghreb during the Middle Holocene: first results of the pollen analysis from Sebkha Kelbia (Central Tunisia), in: The Mediterranean Palynological Societies Symposium 2019. Abstract Book. Université de Bordeaux, p. 98.

Lebreton, V., Messager, E., Marquer, L., Renault-Miskovsky, J., 2010. A neotaphonomic experiment in pollen oxidation and its implications for archaeopalynology. Review of Palaeobotany and Palynology 162, 29–38.

Lewis, J., Dodge, J., Powell, A., 1990. Quaternary dinoflagellate cysts from the upwelling system offshore Peru, Hole 686b, odp leg 1121, in: Proceedings of the Ocean Drilling Program, Scientific Results. pp. 323–328.

Lionello, P., Malanotte-Rizzoli, P., Boscolo, R., Alpert, P., Artale, V., Li, L., Luterbacher, J., May, W., Trigo, R., Tsimplis, M., 2006. The Mediterranean climate: an overview of the main characteristics and issues. Elsevier.

Lionello, P., Trigo, I.F., Gil, V., Liberato, M.L.R., Nissen, K.M., Pinto, J.G., Raible, C.C., Reale, M., Tanzarella, A., Trigo, R.M., Ulbrich, S., Ulbrich, U., 2016. Objective climatology of cyclones in the Mediterranean region: a consensus view among methods with different system identification and tracking criteria. Tellus A: Dynamic Meteorology and Oceanography 68, 29391. https://doi.org/10.3402/tellusa.v68.29391

Lohrenz, S.E., Wiesenburg, D.A., DePalma, I.P., Johnson, K.S., Gustafson, D.E., 1988. Interrelationships among primary production, chlorophyll, and environmental conditions in frontal regions of the western Mediterranean Sea. Deep Sea Research Part A. Oceanographic Research Papers 35, 793–810.

Magny, M., Bégeot, C., Guiot, J., Peyron, O., 2003. Contrasting patterns of hydrological changes in Europe in response to Holocene climate cooling phases. quaternary science reviews 22, 1589–1596.

Marret, F., 1994. Distribution of dinoflagellate cysts in recent marine sediments from the east Equatorial Atlantic (Gulf of Guinea). Review of Palaeobotany and Palynology 84, 1–22.

Marret, F., Turon, J.-L., 1994. Paleohydrology and paleoclimatology off Northwest Africa during the last glacial-interglacial transition and the Holocene: Palynological evidences. Marine Geology 118, 107–117.

Mayewski, P.A., Rohling, E.E., Stager, J.C., Karlén, W., Maasch, K.A., Meeker, L.D., Meyerson, E.A., Gasse, F., Kreveld, S. van, Holmgren, K., Lee-Thorp, J., Rosqvist, G., Rack, F., Staubwasser, M., Schneider, R.R., Steig, E.J., 2004. Holocene climate variability. Quaternary Research 62, 243–255. https://doi.org/10.1016/j.yqres.2004.07.001

McCulloch, M., Taviani, M., Montagna, P., Correa, M.L., Remia, A., Mortimer, G., 2010. Proliferation and demise of deep-sea corals in the Mediterranean during the Younger Dryas. Earth and Planetary Science Letters 298, 143–152.

McGee, D., deMenocal, P.B., Winckler, G., Stuut, J.-B.W., Bradtmiller, L.I., 2013. The magnitude, timing and abruptness of changes in North African dust deposition over the last 20,000 yr. Earth and Planetary Science Letters 371, 163–176.

Meghraoui, M., Morel, J.-L., Andrieux, J., Dahmani, M., 1996. Tectonique plio-quaternaire de la chaine tello-rifaine et de la mer d'Alboran; une zone complexe de convergence continent-continent. Bulletin de la Société géologique de France 167, 141–157.

Mercone, D., Thomson, J., Croudace, I.W., Siani, G., Paterne, M., Troelstra, S., 2000. Duration of S1, the most recent sapropel in the eastern Mediterranean Sea, as indicated by accelerator mass spectrometry radiocarbon and geochemical evidence. Paleoceanography 15, 336–347.

Mercuri, A.M., Florenzano, A., Burjachs, F., Giardini, M., Kouli, K., Masi, A., Picornell-Gelabert, L., Revelles, J., Sadori, L., Servera-Vives, G., 2019. From influence to impact: The multifunctional land use in Mediterranean prehistory emerging from palynology of archaeological sites (8.0-2.8 ka BP). The Holocene 29, 830–846.

Mertens, K.N., Verhoeven, K., Verleye, T., Louwye, S., Amorim, A., Ribeiro, S., Deaf, A.S., Harding, I.C., De Schepper, S., González, C., 2009. Determining the absolute abundance of dinoflagellate cysts in recent marine sediments: the Lycopodium marker-grain method put to the test. Review of Palaeobotany and Palynology 157, 238–252.

Millot, C., 1999. Circulation in the Western Mediterranean Sea. Journal of Marine Systems 20, 423–442.

Millot, C., 1987. The circulation of the Levantine Intermediate Water in the Algerian Basin. Journal of Geophysical Research: Oceans 92, 8265–8276.

Millot, C., 1985. Some features of the Algerian Current. Journal of Geophysical Research: Oceans 90, 7169–7176.

Millot, C., Taupier-Letage, I., 2005. Circulation in the Mediterranean Sea, in: Saliot, A. (Ed.), The Mediterranean Sea, Handbook of Environmental Chemistry. Springer, Berlin, Heidelberg, pp. 29–66.

Miola, A., 2012. Tools for Non-Pollen Palynomorphs (NPPs) analysis: A list of Quaternary NPP types and reference literature in English language (1972–2011). Review of Palaeobotany and Palynology 186, 142–161.

Moreno, A., Cacho, I., Canals, M., Prins, M.A., Sánchez-Goñi, M.-F., Grimalt, J.O., Weltje, G.J., 2002. Saharan dust transport and high-latitude glacial climatic variability: the Alboran Sea record. Quaternary Research 58, 318–328.

Morrill, C., LeGrande, A.N., Renssen, H., Bakker, P., Otto-Bliesner, B.L., 2013. Model sensitivity to North Atlantic freshwater forcing at 8.2 ka. Climate of the Past 9, 955–968.

Naughton, F., Sánchez Goñi, M.F., Drago, T., Conceição Freitas, M., Oliveira, A., 2007. Holocene changes in the Douro estuary (Northwestern Iberia). Journal of Coastal Research 23, 711–720.

Oppo, D.W., McManus, J.F., Cullen, J.L., 2006. Evolution and demise of the Last Interglacial warmth in the subpolar North Atlantic. Quaternary Science Reviews 25, 3268–3277.

Osman, M.K., Bessedik, M., Belkebir, L., Mansouri, M.E.H., Atik, A., Belkhir, A., Rubino, J.-L., Satour, L., Belhadji, A., 2021. Messinian to Piacenzian deposits, erosion, and subsequent marine bioevents in the Dahra Massif (Lower Chelif Basin, Algeria). Arabian Journal of Geosciences 14, 1–36.

Ozenda, P., 1975. Sur les étages de la végétation dans les montagnes du bassin méditerranéen., Documentation de cartographie écologique 16, 1–32.

Pausas, J.G., Vallejo, V.R., 1999. The role of fire in European Mediterranean ecosystems, in: Remote Sensing of Large Wildfires. Springer, pp. 3–16.

Peliz, A., Marchesiello, P., Santos, A.M.P., Dubert, J., Teles- Machado, A., Marta- Almeida, M., Le Cann, B., 2009. Surface circulation in the Gulf of Cadiz: 2. Inflow- outflow coupling and the Gulf of Cadiz slope current. Journal of Geophysical Research: Oceans 114.

Peñalba, M.C., Arnold, M., Guiot, J., Duplessy, J.-C., de Beaulieu, J.-L., 1997. Termination of

the last glaciation in the Iberian Peninsula inferred from the pollen sequence of Quintanar de la Sierra. Quaternary Research 48, 205–214.

Penaud, A., Eynaud, F., Sánchez-Goñi, M., Malaizé, B., Turon, J.-L., Rossignol, L., 2011. Contrasting sea-surface responses between the western Mediterranean Sea and eastern subtropical latitudes of the North Atlantic during abrupt climatic events of MIS 3. Marine Micropaleontology 80, 1–17.

Penaud, A., Eynaud, F., Voelker, A.H.L., Turon, J.-L., 2016. Palaeohydrological changes over the last 50 ky in the central Gulf of Cadiz: complex forcing mechanisms mixing multi-scale processes. Biogeosciences 13, 5357–5377.

Pérez-Folgado, M., Sierro, F.J., Flores, J.A., Cacho, I., Grimalt, J.O., Zahn, R., Shackleton, N., 2003. Western Mediterranean planktonic foraminifera events and millennial climatic variability during the last 70 kyr. Marine Micropaleontology 48, 49–70.

Perkins, H., Pistek, P., 1990. Circulation in the Algerian Basin during June 1986. Journal of Geophysical Research: Oceans 95, 1577–1585.

~~Perrodon, A., 1957. Etude géologique des bassins néogènes sublittoraux de l'Algérie occidentale.~~

Perşoiu, A., Ionita, M., Weiss, H., 2019. Atmospheric blocking induced by the strengthened Siberian High led to drying in west Asia during the 4.2 ka BP event–a hypothesis. Climate of the Past 15, 781–793.

Polunin, O., Walters, M., 1985. Guide to the vegetation of Britain and Europe. Oxford University Press.

Pons, A., Reille, M., 1988. The Holocene-and Upper Pleistocene pollen record from Padul (Granada, Spain): a new study. Palaeogeography, Palaeoclimatology, Palaeoecology 66, 243–263.

Pross, J., Kotthoff, U., Müller, U.C., Peyron, O., Dormoy, I., Schmiedl, G., Kalaitzidis, S., Smith, A.M., 2009. Massive perturbation in terrestrial ecosystems of the Eastern Mediterranean region associated with the 8.2 kyr BP climatic event. Geology 37, 887–890.

Raimbault, P., Coste, B., Boulhadid, M., Boudjellal, B., 1993. Origin of high phytoplankton concentration in deep chlorophyll maximum (DCM) in a frontal region of the Southwestern Mediterranean Sea (Algerian Current). Deep Sea Research Part I: Oceanographic Research Papers 40, 791–804.

Reille, M., 1992. Pollen et spores d'Europe et d'Afrique du Nord. Laboratoire de Botanique historique et Palynologie.

Reimer, P.J., Austin, W.E., Bard, E., Bayliss, A., Blackwell, P.G., Ramsey, C.B., Butzin, M., Cheng, H., Edwards, R.L., Friedrich, M., 2020. The IntCal20 Northern Hemisphere radiocarbon age calibration curve (0–55 cal kBP). Radiocarbon 62, 725–757.

1777 Richter, T.O., Van der Gaast, S., Koster, B., Vaars, A., Gieles, R., de Stigter, H.C., De Haas,
1778 H., van Weering, T.C., 2006. The Avaatech XRF Core Scanner: technical description
1779 and applications to NE Atlantic sediments. Geological Society, London, Special
1780 Publications 267, 39–50.
1781
1782 Rochon, A., De Vernal, A., Turon, J.-L., Matthießen, J., Head, M.J., 1999. Distribution of recent
1783 dinoflagellate cysts in surface sediments from the North Atlantic Ocean and adjacent
1784 seas in relation to sea-surface parameters. American Association of Stratigraphic
1785 Palynologists Contribution Series 35, 1–146.
1786
1787 Rodrigo-Gámiz, M., Martínez-Ruiz, F., Jiménez-Espejo, F.J., Gallego-Torres, D., Nieto-
1788 Moreno, V., Romero, O., Ariztegui, D., 2011. Impact of climate variability in the
1789 western Mediterranean during the last 20,000 years: oceanic and atmospheric responses.
1790 Quaternary Science Reviews 30, 2018–2034.
1791
1792 Rogerson, M., Colmenero- Hidalgo, E., Levine, R.C., Rohling, E.J., Voelker, A.H.L., Bigg,
1793 G.R., Schönfeld, J., Cacho, I., Sierro, F.J., Löwemark, L., 2010. Enhanced
1794 Mediterranean- Atlantic exchange during Atlantic freshening phases. Geochemistry,
1795 Geophysics, Geosystems 11.
1796
1797 Rohling, E., 1994. Review and new aspects concerning the formation of eastern Mediterranean
1798 sapropels. Marine Geology 122, 1–28.
1799
1800 Rohling, E., Den Dulk, M., Pujol, C., Vergnaud-Grazzini, C., 1995. Abrupt hydrographic
1801 change in the Alboran Sea (western Mediterranean) around 8000 yrs BP. Deep Sea
1802 Research Part I: Oceanographic Research Papers 42, 1609–1619.
1803
1804 Rohling, E., Hayes, A., De Rijk, S., Kroon, D., Zachariasse, W.J., Eisma, D., 1998. Abrupt cold
1805 spells in the northwest Mediterranean. Paleoceanography 13, 316–322.
1806
1807 Rohling, E., Marino, G., Grant, K.M., 2015. Mediterranean climate and oceanography, and the
1808 periodic development of anoxic events (sapropels). Earth-Science Reviews 143, 62–97.
1809
1810 Rohling, E., Mayewski, P., Abu-Zied, R., Casford, J., Hayes, A., 2002. Holocene atmosphere-
1811 ocean interactions: records from Greenland and the Aegean Sea. Climate Dynamics 18,
1812 587–593.
1813
1814 Rohling, E., Sprovieri, M., Cane, T., Casford, J.S., Cooke, S., Bouloubassi, I., Emeis, K.C.,
1815 Schiebel, R., Rogerson, M., Hayes, A., 2004. Reconstructing past planktic foraminiferal
1816 habitats using stable isotope data: a case history for Mediterranean sapropel S5. Marine
1817 Micropaleontology 50, 89–123.
1818
1819 Rohling, E.J., Abu-Zied, R., Casford, J.S.L., Hayes, A., Hoogakker, B.A.A., 2009. The marine
1820 environment: present and past. The physical geography of the Mediterranean 33–67.
1821
1822 Rossignol-Strick, M., 1985. Mediterranean Quaternary sapropels, an immediate response of the
1823 African monsoon to variation of insolation. Palaeogeography, palaeoclimatology,
1824 palaeoecology 49, 237–263.
1825
1826 Rossignol-Strick, M., Nesteroff, W., Olive, P., Vergnaud-Grazzini, C., 1982. After the deluge:

Mediterranean stagnation and sapropel formation. Nature 295, 105–110.

Rouis-Zargouni, I., Turon, J.-L., Londeix, L., Essallami, L., Kallel, N., Sicre, M.-A., 2010. Environmental and climatic changes in the central Mediterranean Sea (Siculo–Tunisian Strait) during the last 30 ka based on dinoflagellate cyst and planktonic foraminifera assemblages. Palaeogeography, Palaeoclimatology, Palaeoecology 285, 17–29.

Rouis-Zargouni, I., Turon, J.-L., Londeix, L., Kallel, N., Essallami, L., 2012. The last glacial-interglacial transition and dinoflagellate cysts in the western Mediterranean Sea. Comptes Rendus Geoscience 344, 99–109.

Ruan, J., Kherbouche, F., Genty, D., Blamart, D., Cheng, H., Dewilde, F., Hachi, S., Edwards, R.L., Régnier, E., Michelot, J.-L., 2016. Evidence of a prolonged drought ca. 4200 yr BP correlated with prehistoric settlement abandonment from the Gueldaman GLD1 Cave, Northern Algeria. Climate of the Past 12, 1–14.

Sanchez Goñi, M.F., Cacho, I., Turon, J.-L., Guiot, J., Sierro, F.J., Peypouquet, J.P., Grimalt, J.O., Shackleton, N.J., 2002. Synchroneity between marine and terrestrial responses to millennial scale climatic variability during the last glacial period in the Mediterranean region. Climate dynamics 19, 95–105.

Schäfer, I.K., Lanny, V., Franke, J., Eglinton, T.I., Zech, M., Vysloužilová, B., Zech, R., 2016. Leaf waxes in litter and topsoils along a European transect. Soil 2, 551–564.

Siani, G., Magny, M., Paterne, M., Debret, M., Fontugne, M., 2013. Paleohydrology reconstruction and Holocene climate variability in the South Adriatic Sea. Clim. Past 9, 499–515.

Siani, G., Paterne, M., Arnold, M., Bard, E., Métivier, B., Tisnerat, N., Bassinot, F., 2000. Radiocarbon reservoir ages in the Mediterranean Sea and Black Sea. Radiocarbon 42, 271–280.

Sicre, M.-A., Ternois Y., Miquel J.-C., and Marty J-C, Alkenones in the Mediterranean Sea: interannual variability and vertical transfer. *Geophysical Research Letters* ***26***, 12, 1735-1738, 1999.

Sicre, M.-A., Jalali, B., Eiríksson, J., Knudsen, K.-L., Klein, V., Pellichero, V., 2021. Trends and centennial-scale variability of surface water temperatures in the North Atlantic during the Holocene. Quaternary Science Reviews 265, 107033.

Sicre, M.-A., Jalali, B., Martrat, B., Schmidt, S., Bassetti, M.-A., Kallel, N., 2016. Sea surface temperature variability in the North Western Mediterranean Sea (Gulf of Lion) during the Common Era. Earth and Planetary Science Letters 456, 124–133.

Stambouli-Essassi, S., Roche, E., Bouzid, S., 2007. Evolution de la végétation et du climat dans le Nord-ouest de la Tunisie au cours des 40 derniers millénaires. Geo-Eco-Trop 31, 171–214.

Stockmarr, J.A., 1971. Tabletes with spores used in absolute pollen analysis. Pollen spores 13, 615–621.

Stommel, H., Bryden, H., Mangelsdorf, P., 1973. Does some of the Mediterranean outflow

come from great depth? Pure and Applied Geophysics 105, 879–889.

Stuiver, M., Reimer, P.J., 1993. Extended 14C data base and revised CALIB 3.0 14C age calibration program. Radiocarbon 35, 215–230.

Tachikawa, K., Vidal, L., Cornuault, M., Garcia, M., Pothin, A., Sonzogni, C., Bard, E., Menot, G., Revel, M., 2015. Eastern Mediterranean Sea circulation inferred from the conditions of S1 sapropel deposition. Climate of the Past 11, 855–867.

Targarona, J., Warnaar, J., Boessenkool, K.P., Brinkhuis, H., Canals, M., 1999. Recent dinoflagellate cyst distribution in the North Canary Basin, NW Africa. Grana 38, 170–178.

Tassin, C., 2012. Paysages végétaux du domaine méditerranéen: Bassin méditerranéen, Californie, Chili central, Afrique du Sud, Australie méridionale. IRD éditions.

Tinner, W., van Leeuwen, J.F., Colombaroli, D., Vescovi, E., van der Knaap, W.O., Henne, P.D., Pasta, S., D'Angelo, S., La Mantia, T., 2009. Holocene environmental and climatic changes at Gorgo Basso, a coastal lake in southern Sicily, Italy. Quaternary Science Reviews 28, 1498–1510.

Tintore, J., Violette, P.E.L., Blade, I., Cruzado, A., 1988. A Study of an Intense Density Front in the Eastern Alboran Sea: The Almeria–Oran Front. Journal of Physical Oceanography 18, 1384–1397.

Toucanne, S., Jouet, G., Ducassou, E., Bassetti, M.-A., Dennielou, B., Minto'o, C.M.A., Lahmi, M., Touyet, N., Charlier, K., Lericolais, G., 2012. A 130,000-year record of Levantine Intermediate Water flow variability in the Corsica Trough, western Mediterranean Sea. Quaternary Science Reviews 33, 55–73.

Toucanne, S., Mulder, T., Schönfeld, J., Hanquiez, V., Gonthier, E., Duprat, J., Cremer, M., Zaragosi, S., 2007. Contourites of the Gulf of Cadiz: a high-resolution record of the paleocirculation of the Mediterranean outflow water during the last 50,000 years. Palaeogeography, Palaeoclimatology, Palaeoecology 246, 354–366.

Turon, J.-L., 1984. Direct land/sea correlations in the last interglacial complex. Nature 309, 673–676.

Turon, J.-L., Lézine, A.-M., Denèfle, M., 2003. Land–sea correlations for the last glaciation inferred from a pollen and dinocyst record from the Portuguese margin. Quaternary Research 59, 88–96.

Turon, J.-L., Londeix, L., 1988. Les assemblages de kystes de dinoflagellés en Méditerranée occidentale (Mer d'Alboran). Mise en évidence de l'évolution des paléoenvironnements depuis le dernier maximum glaciaire. Bulletin des Centres de recherches exploration-production Elf-Aquitaine 12, 313–344.

Tzedakis, P.C., 2007. Seven ambiguities in the Mediterranean palaeoenvironmental narrative. Quaternary Science Reviews 26, 2042–2066.

Tzoraki, O., Nikolaidis, N.P., 2007. A generalized framework for modeling the hydrologic and biogeochemical response of a Mediterranean temporary river basin. Journal of Hydrology 346, 112–121.

Van Geel, B., 1972. Palynology of a section from the raised peat bog 'Wietmarscher moor ', with special reference to fungal remains. Acta Botanica Neerlandica 21, 261–284.

Van Nieuwenhove, N., Pospelova, V., Anne, de V., Rochon, A., 2020. A historical perspective on the development of the Northern Hemisphere modern dinoflagellate cyst database. Marine Micropaleontology 159, 101824.

Vannière, B., Colombaroli, D., Chapron, E., Leroux, A., Tinner, W., Magny, M., 2008. Climate versus human-driven fire regimes in Mediterranean landscapes: the Holocene record of Lago dell'Accesa (Tuscany, Italy). Quaternary Science Reviews 27, 1181–1196.

Viúdez, Á., Tintoré, J., 1995. Time and space variability in the eastern Alboran Sea from March to May 1990. Journal of Geophysical Research: Oceans 100, 8571–8586.

Voelker, A.H., Aflidason, A., 2015. Refining the Icelandic tephrachronology of the last glacial period–the deep-sea core PS2644 record from the southern Greenland Sea. Global and Planetary Change 131, 35–62.

Voelker, A.H., Lebreiro, S.M., Schönfeld, J., Cacho, I., Erlenkeuser, H., Abrantes, F., 2006. Mediterranean outflow strengthening during northern hemisphere coolings: a salt source for the glacial Atlantic? Earth and Planetary Science Letters 245, 39–55.

Vogts, A., Moossen, H., Rommerskirchen, F., Rullkötter, J., 2009. Distribution patterns and stable carbon isotopic composition of alkanes and alkan-1-ols from plant waxes of African rain forest and savanna C3 species. Organic Geochemistry 40, 1037–1054.

Wall, D., Dale, B., Lohmann, G.P., Smith, W.K., 1977. The environmental and climatic distribution of dinoflagellate cysts in modern marine sediments from regions in the North and South Atlantic Oceans and adjacent seas. Marine micropaleontology 2, 121–200.

Watts, W.A., Allen, J.R.M., Huntley, B., Fritz, S.C., 1996. Vegetation history and climate of the last 15,000 years at Laghi di Monticchio, southern Italy. Quaternary Science Reviews 15, 113–132.

Zanchetta, G., Drysdale, R.N., Hellstrom, J.C., Fallick, A.E., Isola, I., Gagan, M.K., Pareschi, M.T., 2007. Enhanced rainfall in the Western Mediterranean during deposition of sapropel S1: stalagmite evidence from Corchia cave (Central Italy). Quaternary Science Reviews 26, 279–286.

Zielhofer, C., Faust, D., 2008. Mid-and Late Holocene fluvial chronology of Tunisia. Quaternary Science Reviews 27, 580–588.

Zielhofer, C., Fletcher, W.J., Mischke, S., De Batist, M., Campbell, J.F., Joannin, S., Tjallingii, R., El Hamouti, N., Junginger, A., Stele, A., 2017. Atlantic forcing of Western Mediterranean winter rain minima during the last 12,000 years. Quaternary Science

Reviews 157, 29–51.

Zonneveld, K.A.F., Bockelmann, F., Holzwarth, U., 2007. Selective preservation of organic-walled dinoflagellate cysts as a tool to quantify past net primary production and bottom water oxygen concentrations. Marine Geology 237, 109–126.

Zonneveld, K.A.F., Ganssen, G., Troelstra, S., Versteegh, G.J., Visscher, H., 1997. Mechanisms forcing abrupt fluctuations of the Indian Ocean summer monsoon during the last deglaciation. Quaternary Science Reviews 16, 187–201.

Zonneveld, K.A.F., Hoek, R.P., Brinkhuis, H., Willems, H., 2001. Geographical distributions of organic-walled dinoflagellate cysts in surficial sediments of the Benguela upwelling region and their relationship to upper ocean conditions. Progress in Oceanography 48, 25–72.

Zonneveld, K.A.F., Versteegh, G., Kodrans-Nsiah, M., 2008. Preservation and organic chemistry of Late Cenozoic organic-walled dinoflagellate cysts: A review. Marine Micropaleontology 68, 179–197.

Table

Table 1

Code	Spectrometer	Depth (cm)	Dated material	^{14}C age	Error	^{14}C age – reservoir age	IntCal20 Cal BP Min-Max	Error σ
SacA43123	ECHoMICADAS	3	*G. bulloides*	170	30	-230	**0** 0-0	1 σ
SacA55619*	ARTEMIS	31[a]	*G. bulloides*	820	30	420	**491,5** 472-511	1 σ
SacA55620	ARTEMIS	231	*G. bulloides*	1400	30	1000	**928,5** 900-957	2 σ
GifA20376	ECHoMICADAS	311	*G. bulloides*	1290	60	890	**817** 716-918	2 σ
SacA55621	ARTEMIS	431	*G. bulloides*	2165	30	1765	**1644,5** 1571-1718	2 σ
GifA21150	ECHoMICADAS	522	*G. bulloides*	3610	70	3210	**3424** 3357-3723	1 σ
GifA18283	ECHoMICADAS	531	*G. bulloides*	3870	80	3470	**3737,5** 3634-3841	1 σ
SacA54337	ARTEMIS	531	*G. bulloides*	3820	30	3420	**3647,5** 4229-4522	2 σ
GifA20378	ECHoMICADAS	550	*G. bulloides*	4330	60	3930	**4375,5** 4229-4522	2 σ
GifA21151	ECHoMICADAS	559	*G. bulloides*	4390	60	3990	**4432** 4245-4619	2 σ
GifA20380	ECHoMICADAS	579	*G. bulloides*	5000	60	4600	**5342,5** 5214-5471	2 σ
GifA21152	ECHoMICADAS	581	*G. bulloides*	5060	70	4660	**5392** 5315-5469	1 σ
SacA55622	ARTEMIS	631	*G. bulloides*	6200	30	5800	**6584** 6499-6669	2 σ
GifA18282	ECHoMICADAS	731	*G. bulloides*	8470	70	8070	**8917,5** 8696-9139	2 σ
SacA54338	ARTEMIS	731	*G. bulloides*	7990	35	7590	**8392** 8374-8410	1 σ
GifA18256*	ECHoMICADAS	931[b]	*G. bulloides*	11110	270	10710	**12488,5** 11808-13169	2 σ
SacA54339	ARTEMIS	931	*G. bulloides*	10600	40	10200	**11867,5** 11739-11996	2 σ
SacA54335	ARTEMIS	978	Gastéropode	11000	40	10600	**12653** 12616-12690	1 σ
SacA54336	ARTEMIS	978	Gastéropode	11015	40	10615	**12659** 12621-12697	1 σ
SacA55623	ARTEMIS	1031	*G. bulloides*	12445	40	12045	**13920,5** 13804-14037	2 σ

2023 Table 2

2024

Pollen zones	Limits	Interval (cm)	Age (cal BP)	Description of Dinocyst zones	Pollen zones	Inferred hydrological changes	Description of pollen zone	Vegetation changes	Inferred climatic changes	Non-pollen palynomorphs remarks
MD04-5	Top - f	0 - 370	0 - 1 400	High values of *Brigantedinium* spp. (60% mainly), *S. mirabilis* and *O. centrocarpum*. Increasing values of estuarine-stratified taxa and thermophilous full-oceanic taxa. Diverse coastal productivity and upwelling heterotrophic assemblage. Occurences of *Lejeunecysta* spp.	Highest heterotrophic taxa representations. Mixed upwelling and coastal productivity.	Upwelling driven productivity mixed with river discharge induced coastal productivity. Increasing oligotrophic conditions signal	Strongest representation of *Cichorioideae* (up to 35% mainly), *Asteroideae*. Stable percentages of *Poaceae*, *Quercus ilex*, deciduous *Quercus*, *Olea*, *Pistacia, Juniperus*, *Cupressus*, *Cedrus*. Increasing percentages of *Ephedra* and *Atremisia*. Increasing occurrences and representations of human impact taxa.	Open shrubs and steppe vegetation combined with open mediterranean forest forming mattorals and maquis. Potential human activity expansion.	Increasing aridity	Freshwater algae stable representation. Glomus high abundances, ascospores stable abundances. Occasional coprophilous abundances.
	f - e	370 - 485	1 400 - 2 700	High values of *Brigantedinium* spp. (60% mainly) followed by stable represented *S. mirabilis* and *O. centrocarpum*. Diverse coastal productivity and upwelling heterotrophic assemblage. High representation of *T. applanatuml.*	Highest heterotrophic taxa representations. High upwelling and coastal productivity.	Upwelling drived productivity under relatively stable Atlantic influence.	Strong increase of *Cichorioideae* (30% mainly), *Asteroideae*. Stable percentages of *Poaceae*, *Quercus ilex,* deciduous *Quercus*, *Olea*, *Pistacia*, *Juniperus*, *Cupressus*, *Cedrus*, *Ephedra* and *Artemisia*.	Open shrubs and steppe vegetation combined with open mediterranean forest forming mattorals and maquis.	Increasing aridity	Freshwater algae stable representation. Glomus high abundances, ascospores stable abundances.
MD04-4	e- d	485 - 575	2 700 - 5 120	High values of *S. mirabilis* (30% mainly) and *I. aculeatum*. High representations of *L. machaerophorum*. Increasing percentages of *S. bentorii*, *N. labyrinthus* and *T. applanatum*.	Highrepresentation of phototrophic taxa. Upwelling cortege strong representation.	Intense upwelling activity. Intense oceanic influence. Seasonal oligotrophic stratified warm surface waters persistent signal.	Increasing of *Chenopodiaceae*, *Cichorioideae*, *Artemisia* and *Ephedra*. Small decrease of *Quercus ilex* and decrease of *Pistacia, Quercus suber* and *Cedrus*.	Open mediterranean forest with extended underbrush and maquis of Cichorioideae, Asteraceae and Poaceae steppe	Decreasing rainfalls with centennial oscillations	Lower freshwater algae and Glomus abundances. Peak of ascospores around 540 cm.
MD04-3	d - c	575 - 740	5 120 - 8 600	High values of Brigantedinium spp. increasing percentages of I. aculeatum (15-20% mainly) and S. mirabilis. Rare occurrences of *Lejeunecysta* spp. And *T. applanatum.*	Stable strong heterotrophic representation. Highest percentages of the Thermophilous full-oceanic taxa majorly represented by Impagidinium aculeatum.	Strongest oligotrophic surface conditions, increasing stratification and sea surface temperature. Persitant upwelling productivity signal.	Highest trees percentages. Increasing percentages of *Cupressaceae*, *Pistacia* and *Olea*, *Quercus ilex* and *Poaceae*. Decrease of *Chenopodiaceae* and small decrease of *Cichorioideae* which peaks from 650 to 600 cm.	Open mediterranean oak forest combined with underbrush and maquis of Cichorioideae, Asteraceae and Poaceae	Increased humidity and temperature marked with centennial oscillations	Highest representations of freshwater algae. Stable high representation of Glomus and ascospores.

	c - b	740 - 910	8600 - 11 500	High percentages of *Brigantedinium* spp. (40 % mainly). Diverse coastal productivity and upwelling heterotrophic assemblage. Highest percentages of *O. centrocarpum* (10-20% mainly).	Increasing of the heterotrophic taxa representations. Increasing representation of thermophilous full-oceanic taxa.	Oligotrophic surface conditions, stratification and sea surface temperature. Persitant upwelling driven productivity.	Strong increase of *Quercus ilex*, deciduous *Quercus*, *Pistacia, Olea, Asteroideae*, *Cichorioideae* and *Poaceae*. Decrease of *Cedrus, Chenopodiaceae*, *Artemisia* and *Ephedra*. Increasing representation of monocotyledonae and pteridophyte spores.	Open mediterranean forest and underbush or maquis	Warmer conditions and gradual increased humidity	Stable high representation of Glomus and ascospores.
MD04-2	b - a	910 - 1 025	11 500 - 13 700	Increase of the *N. labyrinthus* percentages (30 - 35% mainly). Cold water taxa *S. lazus* and *B. tepikiense* are also represented in high values. *O. centrocarpum* shows stronger representations around 910-950 cm. Highest representation og the intern neritic taxa *S. ramosus*, *S. bentorii* and *S. membranaceus*.	Decrease of the heterotrophic taxa representation with the persistance of upwelling cortege taxa. Increasing percentages of cold water taxa and extern neritic photrophic taxa. Diversified assemblage.	Cold surface temperature. Strong oceanic influence. Highest productivity period in thesequence.	Highest representations of *Cedrus* (30% mainly) with two major peaks at 970 and 1000 cm (reaching more than 40%). Increase of *Chenopodiaceae*, *Artemisia* and *Ephedra* with a decrease ogf all *Quercus ilex*, *Quercus suber* and *Cupressaceae*.	Steppe with semi-desert plants. Sparse Pine and coniferous woodlands and Cedrus forests uplands.	Dry and cold conditions	Weak or lacking freshwater algae and fungal spores signal
MD04-1	a - Bottom	1 025 - 1 042	13 700 - 14 000	Dominance of *Brigantedinium* spp.	Dominanceof the heterotrophic taxon Birgantedinium spp.	Apparent productive conditions, active upwelling.	Dominance of *Chenopodiaceae*, *Cichorioideae* and *Poaceae* associated to *Artemisia* and *Ephedra*. Low representation of *Querus ilex* (less than 10 %) and *Cupressaceae*.	Dominating steppe with sparse mediterranean woodlands.	Dry conditions	Weak or lacking freshwater algae and fungal spores signal

Table 2

Figures

Figure 1

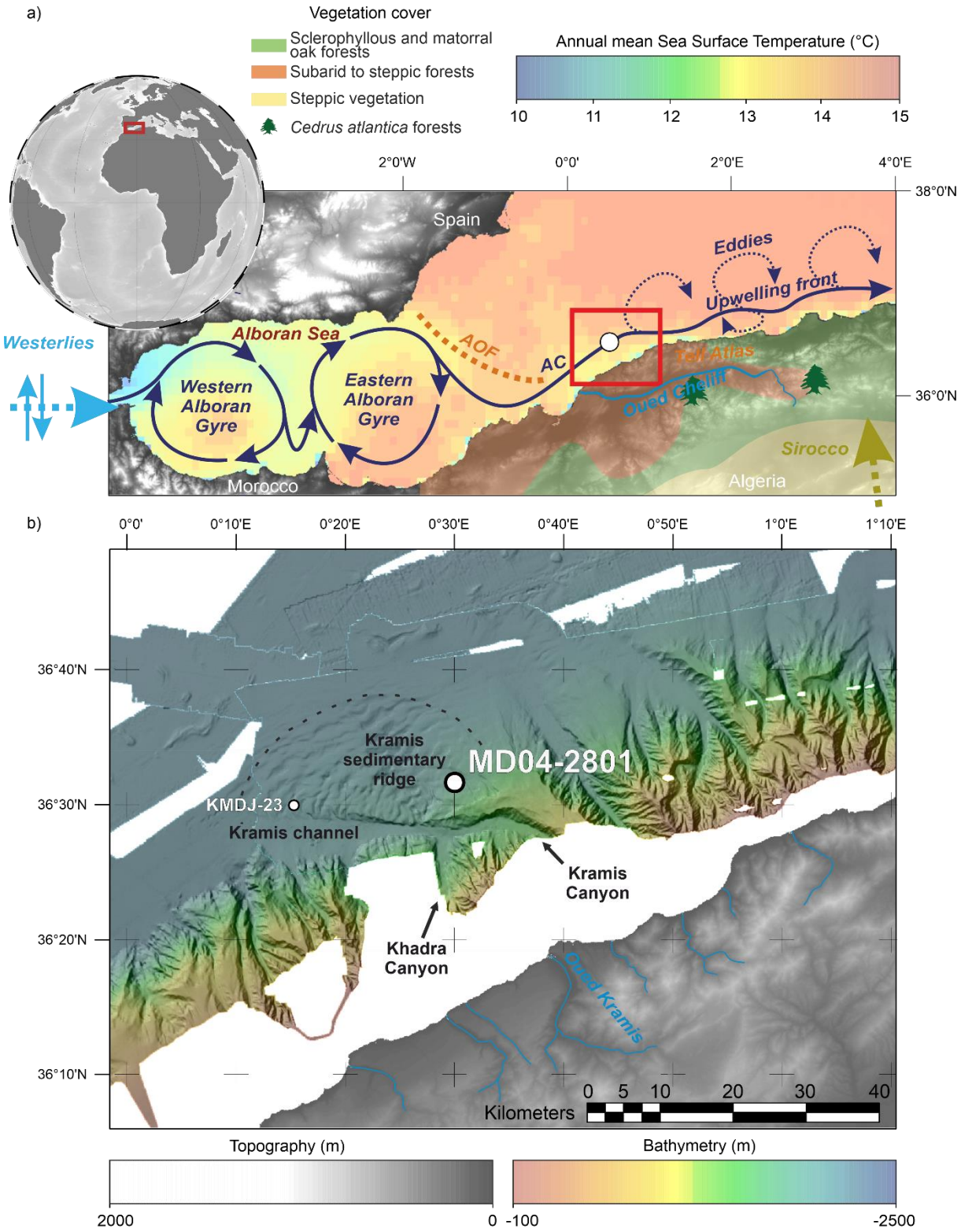

2034

2035 Figure 2

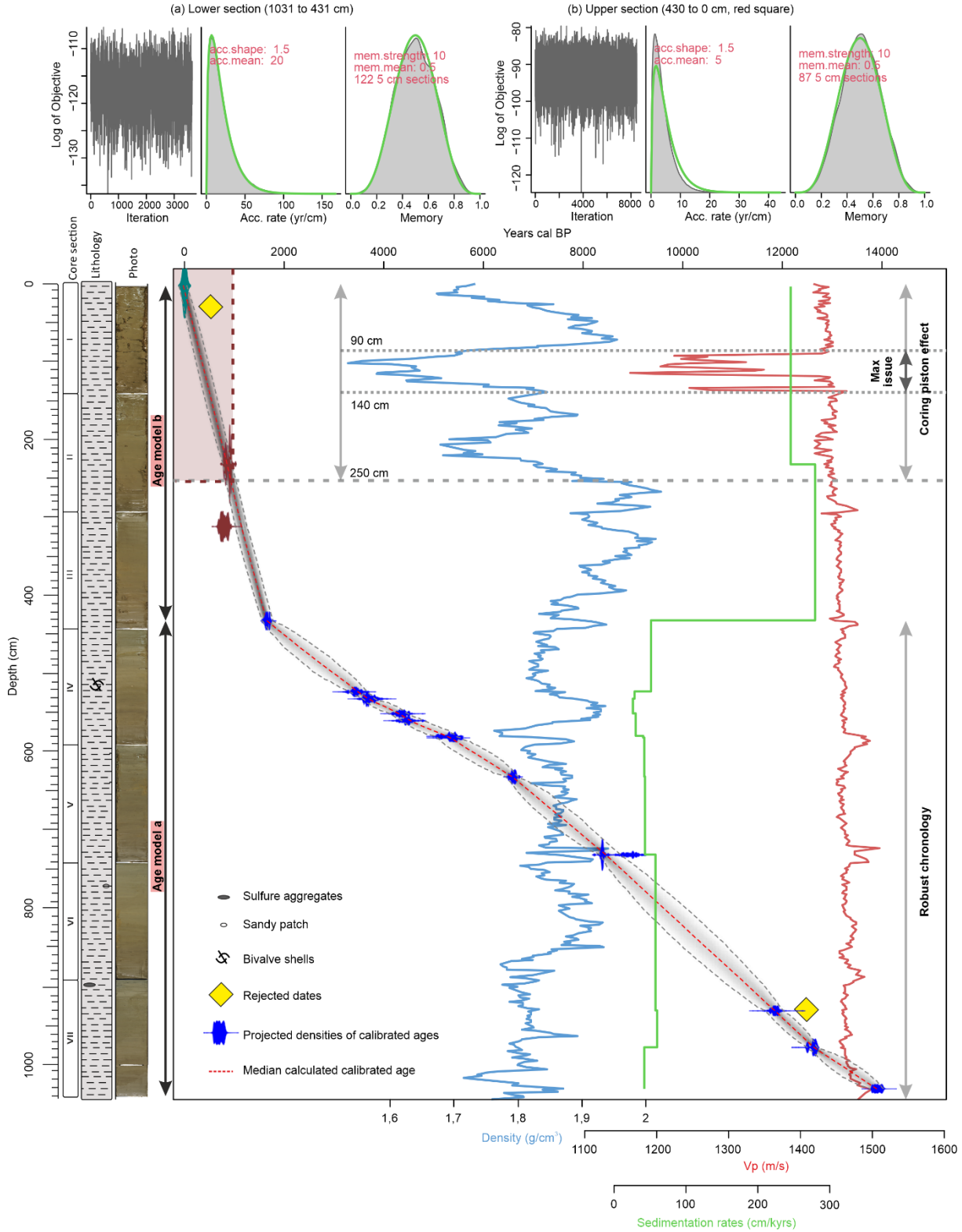

2036

2037

2038

2039

2040

2041 Figure 3

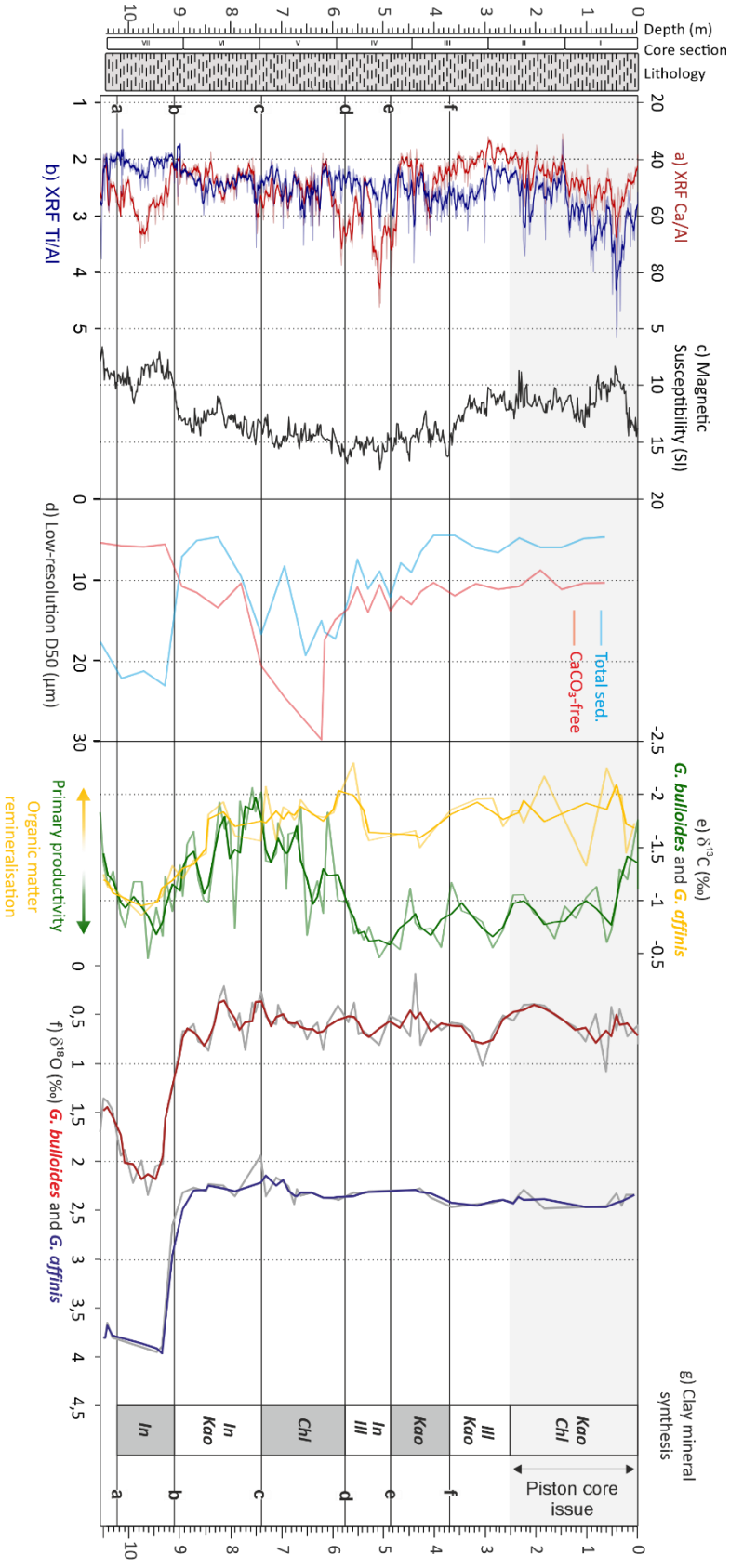

2042

2043

Figure 4

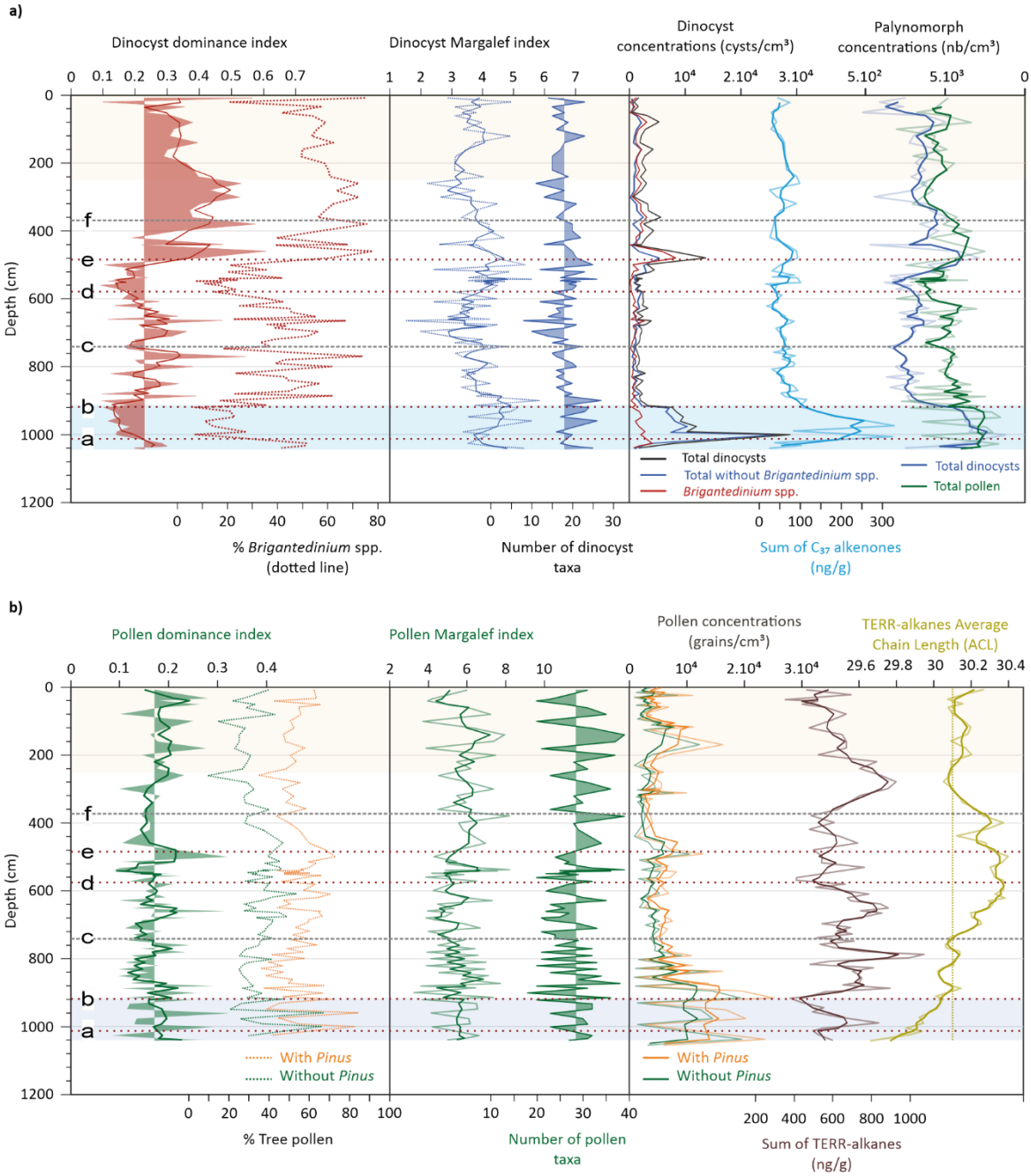
a)
Dinocyst dominance index
Dinocyst Margalef index
Dinocyst concentrations (cysts/cm³)
Palynomorph concentrations (nb/cm³)
Depth (cm)
Total dinocysts
Total without Brigantedinium spp.
Brigantedinium spp.
Total dinocysts
Total pollen
% Brigantedinium spp. (dotted line)
Number of dinocyst taxa
Sum of C37 alkenones (ng/g)
b)
Pollen dominance index
Pollen Margalef index
Pollen concentrations (grains/cm³)
TERR-alkanes Average Chain Length (ACL)
With Pinus
Without Pinus
With Pinus
Without Pinus
% Tree pollen
Number of pollen taxa
Sum of TERR-alkanes (ng/g)

2054 Figure 5

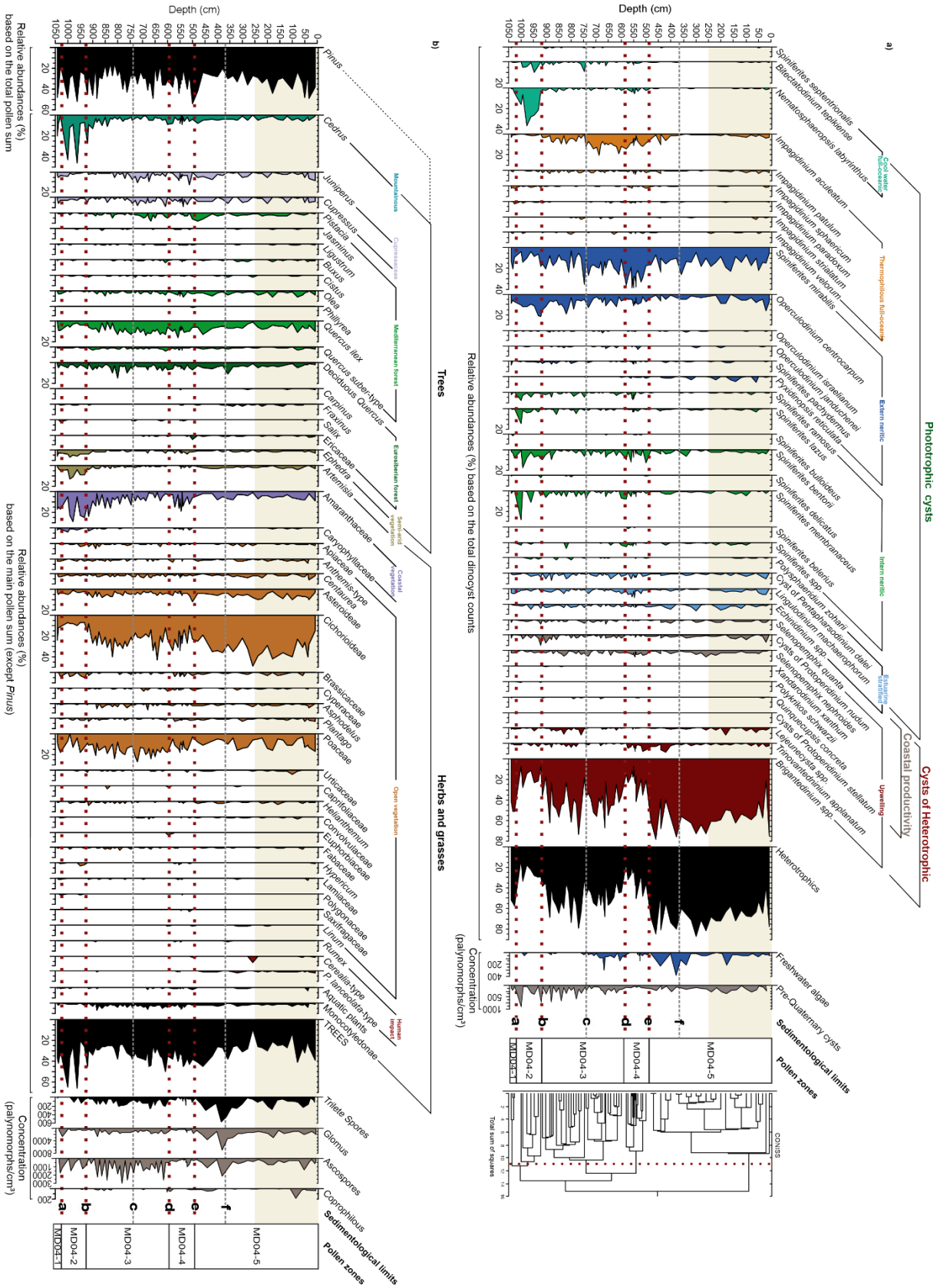

2055

2056

2057

Figure 6

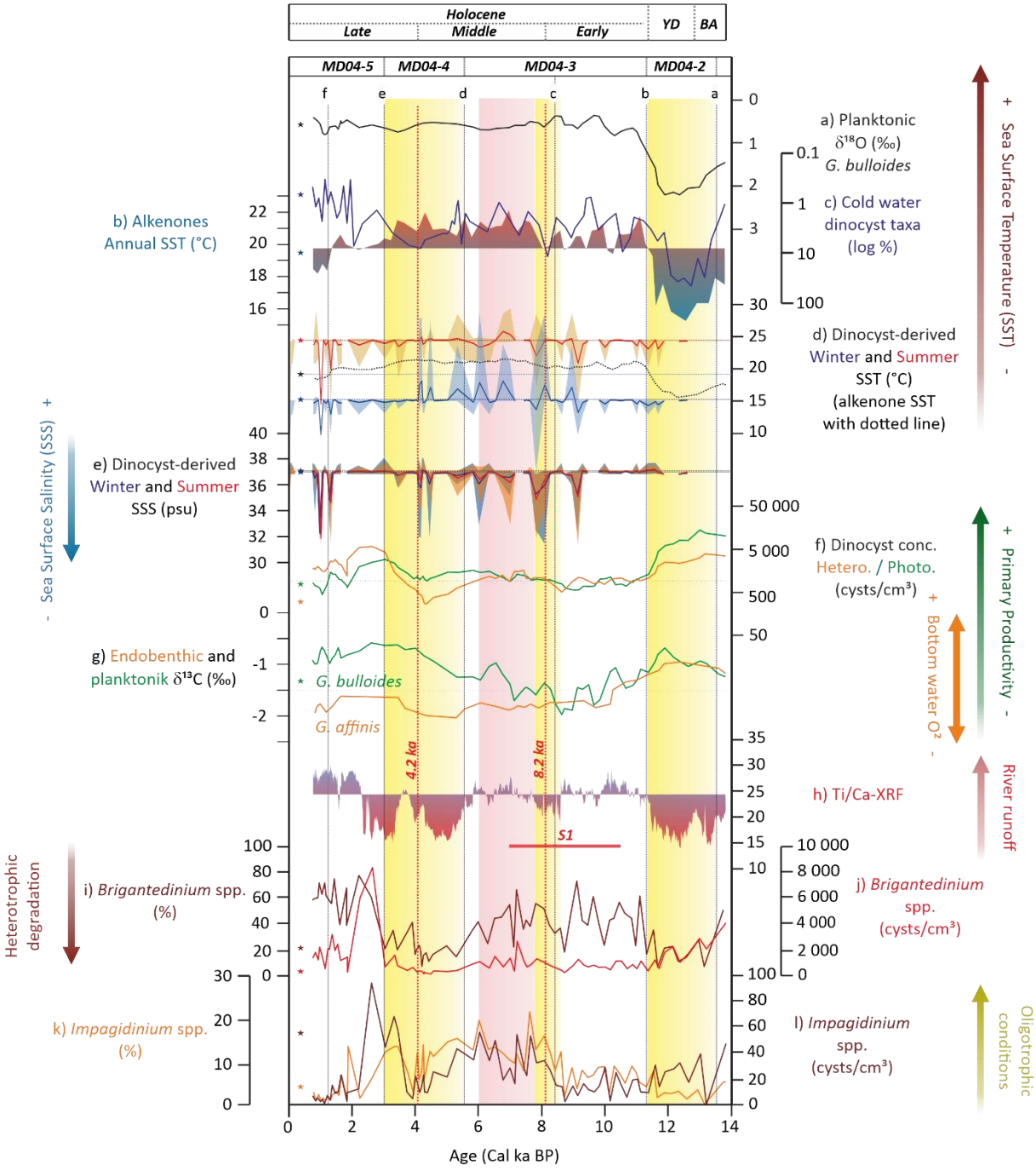
Holocene
Late
Middle
Early
YD
BA
MD04-5
MD04-4
MD04-3
MD04-2
f
e
d
c
b
a
a) Planktonic δ18O (‰) G. bulloides
b) Alkenones Annual SST (°C)
c) Cold water dinocyst taxa (log %)
d) Dinocyst-derived Winter and Summer SST (°C) (alkenone SST with dotted line)
+ Sea Surface Temperature (SST) -
- Sea Surface Salinity (SSS) +
e) Dinocyst-derived Winter and Summer SSS (psu)
f) Dinocyst conc. Hetero. / Photo. (cysts/cm³)
+ Primary Productivity -
+ Bottom water O2 -
g) Endobenthic and planktonik δ13C (‰)
G. bulloides
G. affinis
4.2 ka
8.2 ka
S1
h) Ti/Ca-XRF
River runoff
Heterotrophic degradation
i) Brigantedinium spp. (%)
j) Brigantedinium spp. (cysts/cm³)
k) Impagidinium spp. (%)
l) Impagidinium spp. (cysts/cm³)
Oligotrophic conditions
Age (Cal ka BP)

2068 Figure 7

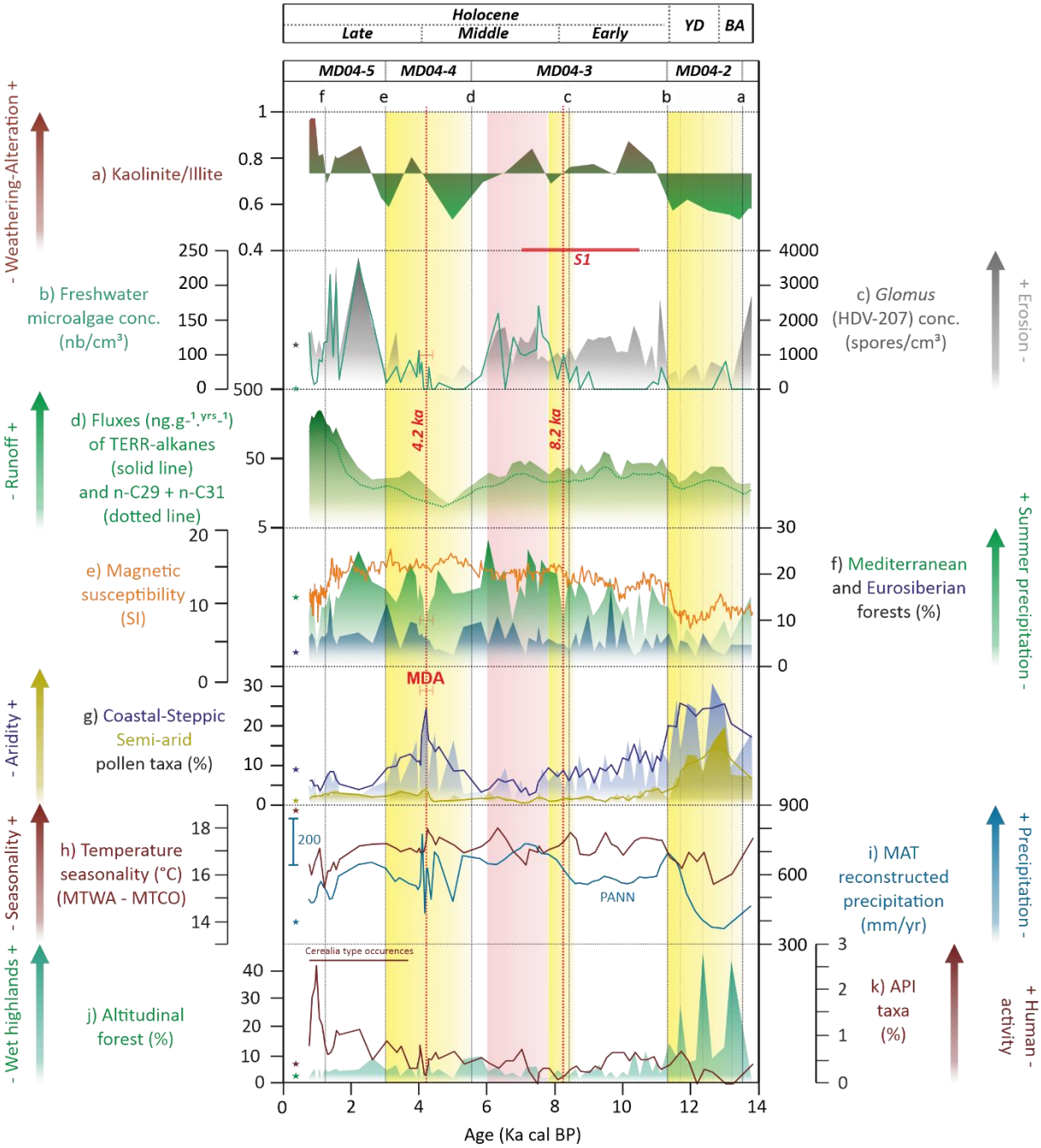

2069
2070
2071
2072
2073
2074
2075
2076
2077

2078 Figure 8

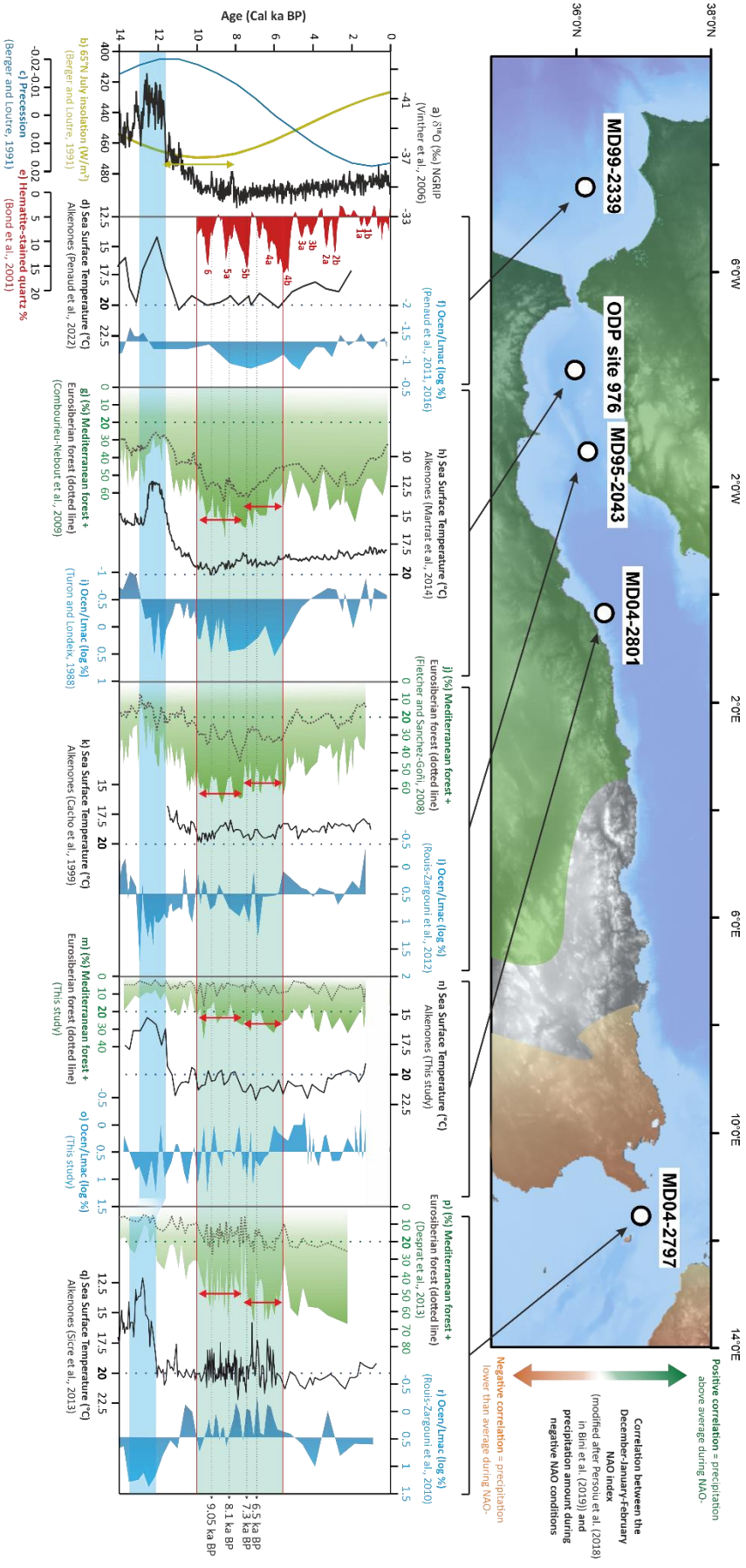

2079